

# Enantioselective Recognition of Ammonium Carbamates in a Chiral Metal–Organic Framework

Jeffrey D. Martell,<sup>†,‡</sup> Leo B. Porter-Zasada,<sup>†</sup> Alexander C. Forse,<sup>†,§,||</sup> Rebecca L. Siegelman,<sup>†</sup> Miguel I. Gonzalez,<sup>†</sup> Julia Oktawiec,<sup>†</sup> Tomče Runčevski,<sup>†,⊥</sup> Jiawei Xu,<sup>#</sup> Monika Srebro-Hooper,<sup>∇</sup> Phillip J. Milner,<sup>†</sup> Kristen A. Colwell,<sup>§</sup> Jochen Autschbach,<sup>°</sup> Jeffrey A. Reimer,<sup>§,⊥</sup> and Jeffrey R. Long<sup>\*,†,§,⊥</sup>

<sup>†</sup>Department of Chemistry, University of California, Berkeley, California 94720, United States

<sup>‡</sup>Miller Institute for Basic Research in Science, University of California, Berkeley, California 94720, United States

<sup>§</sup>Department of Chemical and Biomolecular Engineering, University of California, Berkeley, California 94720, United States

<sup>||</sup>Berkeley Energy and Climate Institute, University of California, Berkeley, California 94720, United States

<sup>⊥</sup>Materials Sciences Division, Lawrence Berkeley National Laboratory, Berkeley, California 94720, United States

<sup>#</sup>Jasco Corporation, 2967-5 Ishikawa-machi, Hachioji-shi, Tokyo 192-8537, Japan

<sup>∇</sup>Faculty of Chemistry, Jagiellonian University, 30-387 Krakow, Poland

<sup>°</sup>Department of Chemistry, University at Buffalo, State University of New York, Buffalo, New York 14260, United States

Table of Contents	Page
1. Characterization and CO <sub>2</sub> adsorption properties of dach–Mg <sub>2</sub> (dobpdc) variants .....	S2
2. Characterization of dach–Mg <sub>2</sub> (pc-dobpdc) variants .....	S15
3. Testing diamine mixtures in Mg <sub>2</sub> (dobpdc) .....	S20
4. Dach–Zn <sub>2</sub> (dobpdc) single-crystal structure and CO <sub>2</sub> adsorption properties .....	S22
5. Testing additives for chiral induction of Mg <sub>2</sub> (dobpdc) .....	S29
6. Characterization of <i>R</i> - and <i>S</i> -Mg <sub>2</sub> (dobpdc) .....	S38
7. Solid-state circular dichroism and calculated CD spectra .....	S48
8. Attempts to synthesize large enantiopure Zn <sub>2</sub> (dobpdc) single crystals .....	S54
9. Powder X-ray diffraction of dach-appended <i>R</i> - and <i>S</i> -Mg <sub>2</sub> (dobpdc) .....	S55
10. Density functional theory calculations .....	S65
11. Solid-state NMR spectroscopy .....	S71
12. Testing a different chiral diamine-appended Mg <sub>2</sub> (dobpdc) variant .....	S74
13. References .....	S76

# 1. Characterization and CO<sub>2</sub> adsorption properties of dach–Mg<sub>2</sub>(dobpdc) variants

## Determination of thermodynamic parameters for CO<sub>2</sub> adsorption in dach–Mg<sub>2</sub>(dobpdc) variants.

All CO<sub>2</sub> adsorption isobars presented in the main text were obtained with a temperature ramp rate of 2 °C/min in order to expedite data collection for numerous samples. To determine more precisely the CO<sub>2</sub> adsorption step positions, isobars were collected with a much slower temperature ramp rate of 0.1 °C/min (Figure S5). Very high step temperatures of 181 °C and 142 °C were observed for the two adsorption steps of (*R,R*)-dach-(±)-Mg<sub>2</sub>(dobpdc) (dach = *trans*-1,2-diaminocyclohexane). These temperatures were ~25 °C higher than those observed when a 2 °C/min cooling rate was used, reflecting slow CO<sub>2</sub> adsorption kinetics in this material relative to previously-published diamine-appended variants of Mg<sub>2</sub>(dobpdc), for which changing the temperature ramp rate does not have such a large impact on step temperature. In a CO<sub>2</sub> adsorption isobar using a slow 0.1 °C/min cooling rate, (±)-dach-(±)-Mg<sub>2</sub>(dobpdc) exhibited a step temperature of 162 °C, which was also substantially higher than the step temperature observed with a 2 °C/min cooling rate (Figure S6). Approximate values for  $\Delta h_{\text{ads}}$  and  $\Delta s_{\text{ads}}$  were estimated by comparing the TGA adsorption step positions to values previously determined for other diamine-appended variants of Mg<sub>2</sub>(dobpdc) (Table S1).<sup>1,2</sup> For these previously-published adsorbents, the isobaric CO<sub>2</sub> adsorption step temperatures had been determined, and gas sorption isotherms at a minimum of three different temperatures had been performed to calculate both  $\Delta h_{\text{ads}}$  and  $\Delta s_{\text{ads}}$ . Plotting  $\Delta h_{\text{ads}}$  versus the isobaric step temperature for all of diamine variants depicted in Table S1 revealed a linear correlation (Figure S7). A similar linear correlation was observed when  $\Delta s_{\text{ads}}$  was plotted versus TGA step temperature (Figure S8). Trend lines were generated using linear regressions, as depicted on the plots in Figure S7 and Figure S8. Approximate values for  $\Delta h_{\text{ads}}$  and  $\Delta s_{\text{ads}}$  were determined by inputting step temperature into the linear fitting functions (Figure S7 and Figure S8). For the high-temperature step of (*R,R*)-dach-(±)-Mg<sub>2</sub>(dobpdc),  $\Delta h_{\text{ads}} = 111 \pm 9$  kJ/mol and  $\Delta s_{\text{ads}} = 244 \pm 26$  J/mol·K. For the low-temperature step of (*R,R*)-dach-(±)-Mg<sub>2</sub>(dobpdc),  $\Delta h_{\text{ads}} = 91 \pm 7$  kJ/mol and  $\Delta s_{\text{ads}} = 211 \pm 20$  J/mol·K. For (±)-dach-(±)-Mg<sub>2</sub>(dobpdc),  $\Delta h_{\text{ads}} = 102 \pm 8$  kJ/mol and  $\Delta s_{\text{ads}} = 228 \pm 23$  J/mol·K.

We attempted to corroborate these thermodynamic parameters by collecting gas sorption isotherms for (*R,R*)-dach-(±)-Mg<sub>2</sub>(dobpdc) at 55, 65, 75, and 85 °C (data not shown). All of the isotherms exhibited two adsorption steps with equal heights, consistent with the two steps observed in TGA isobars. However, the step pressures were substantially higher than predicted on the basis of the pure CO<sub>2</sub> isobars, and  $\Delta h_{\text{ads}}$  determined for the low-pressure step (equivalent to the high-temperature step) using the Clausius–Clapeyron equation was lower than  $\Delta h_{\text{ads}}$  determined for the high-pressure step (data not shown). This lower adsorption enthalpy for a lower-pressure step was inconsistent with all prior studies on this class of materials, and it was likely a result of the measured step pressures to be too high due to the extremely slow adsorption kinetics in this material preventing equilibration from being reached.

We additionally attempted to validate the thermodynamic adsorption parameters using TGA adsorption isobars with various partial pressures of CO<sub>2</sub> (data not shown). (*R,R*)-dach-(±)-Mg<sub>2</sub>(dobpdc) was activated under flowing N<sub>2</sub> on the TGA, the gas stream was switched to CO<sub>2</sub> at a partial pressure of interest (mixed with N<sub>2</sub>), and the sample was slowly cooled to a temperature very close to the adsorption step for 3 h. A fast flow rate of 100 mL/min was used in an effort to enable equilibration within a shorter time frame. In spite of this very long equilibration time, the sample mass did not stabilize during the 3 h period, a consequence of the extremely slow adsorption kinetics of this material, especially at temperatures close to the step. While even longer equilibration times could be explored, diamine loss was a serious concern.

Holding the sample isothermally at temperatures above 160 °C for many hours with a flow rate of 100 mL/min caused diamine loss.

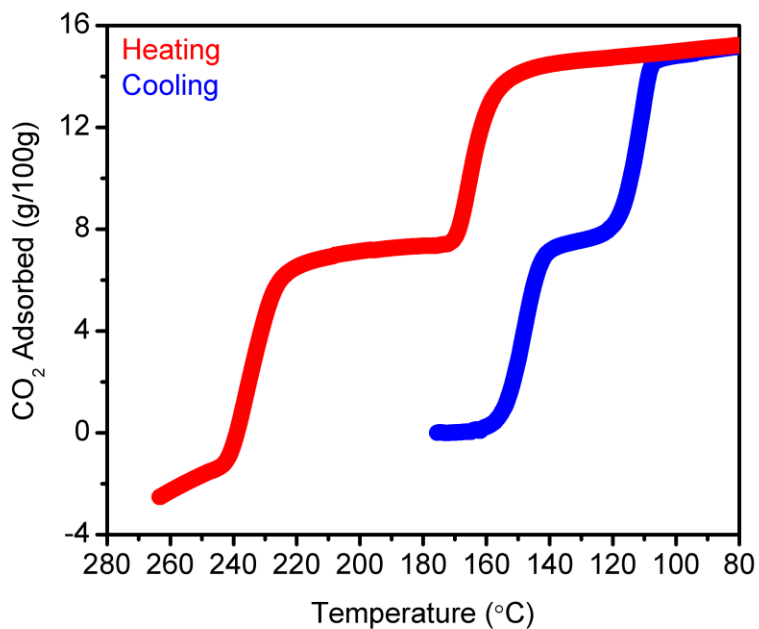


**Figure S1.** Thermogravimetric adsorption (blue, cooling) and desorption (red, heating) isobars collected for (*S,S*)-dach-(±)-Mg<sub>2</sub>(dobpdc) under pure CO<sub>2</sub> at a temperature ramp rate of 2 °C/min.

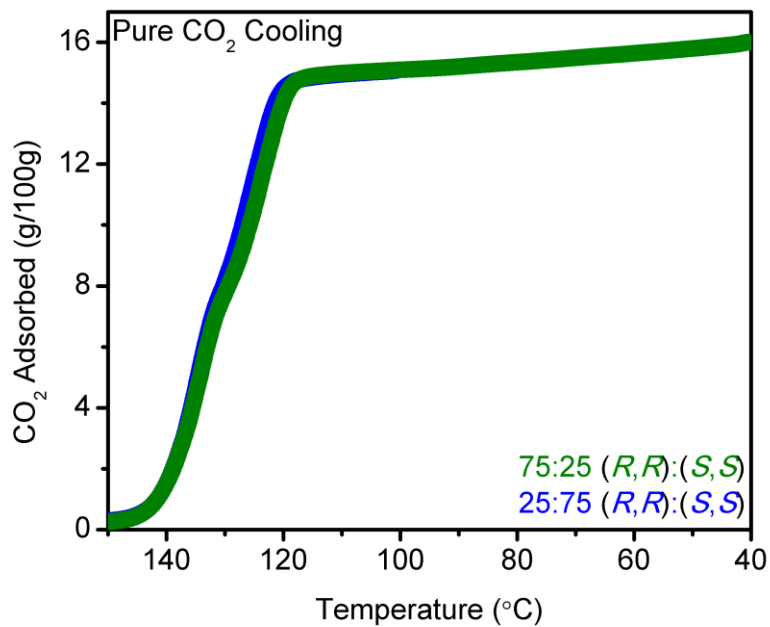


**Figure S2.** Thermogravimetric adsorption (cooling) isobars under pure CO<sub>2</sub> for (±)-Mg<sub>2</sub>(dobpdc) grafted with a solution of 75:25 (*R,R*)-dach:(*S,S*)-dach (green) or 25:75 (*R,R*)-dach:(*S,S*)-dach (blue). A temperature ramp rate of 2 °C/min was used.

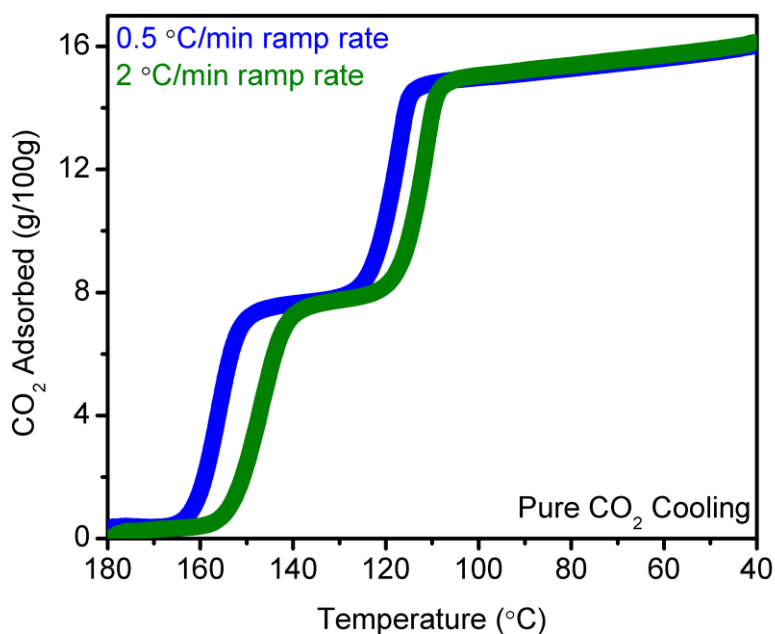


**Figure S3.** Thermogravimetric adsorption (cooling) isobars under pure CO<sub>2</sub> for (*R,R*)-dach-(±)-Mg<sub>2</sub>(dobpdc) with a temperature ramp rate of 2 °C/min (green) or 0.5 °C/min (blue).

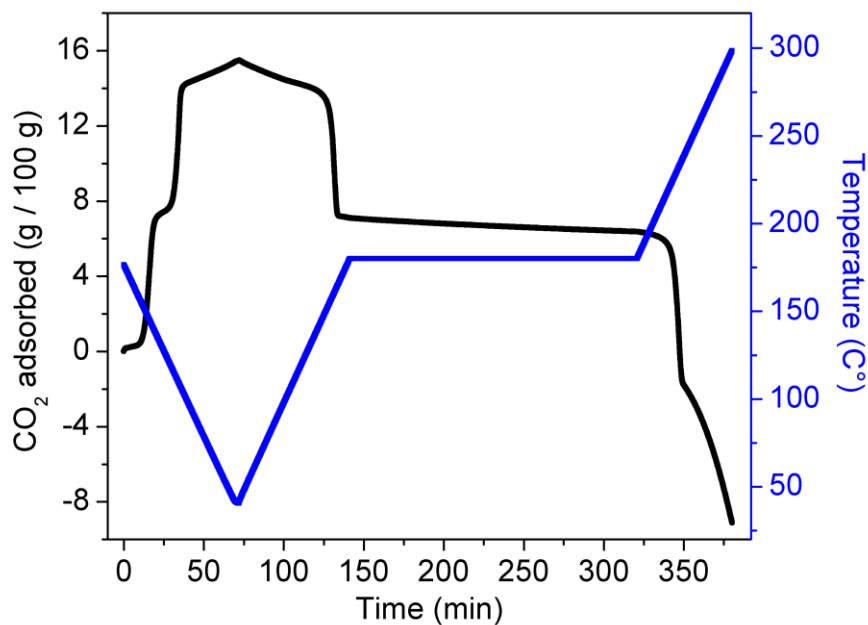


**Figure S4.** Thermogravimetric analysis of CO<sub>2</sub> adsorption and desorption (black) as a function of temperature (blue) for (*S,S*)-dach-(±)-Mg<sub>2</sub>(dobpdc). A temperature ramp rate of 2 °C/min was used, and during desorption the temperature was held isothermally at 180 °C for 3 h. Diamine loss due to volatilization is apparent during the heating from 180 °C to 300 °C. Diamine loading was 73% at the conclusion of this experiment based on <sup>1</sup>H NMR spectroscopy of a digested sample.

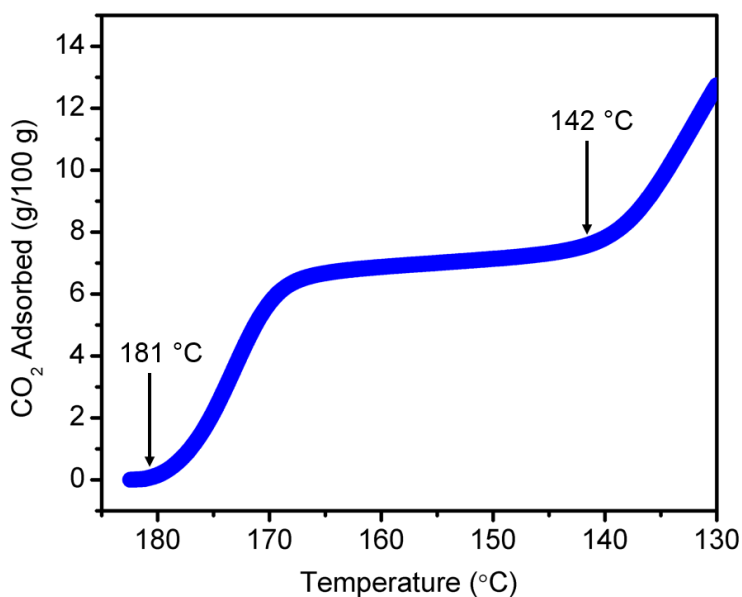


**Figure S5.** Thermogravimetric adsorption (cooling) isobar under pure CO<sub>2</sub> for (*R,R*)-dach-(±)-Mg<sub>2</sub>(dobpdc) with a temperature ramp rate of 0.1 °C/min and a flow rate of 100 mL/min, as opposed to the standard flow rate of 25 mL/min used for the other isobars in this manuscript. This faster flow rate was

used for calculation of thermodynamic parameters, to facilitate comparison with literature values for other diamine-appended variants. The points of onset for the two adsorption steps were 181 and 142 °C, respectively.

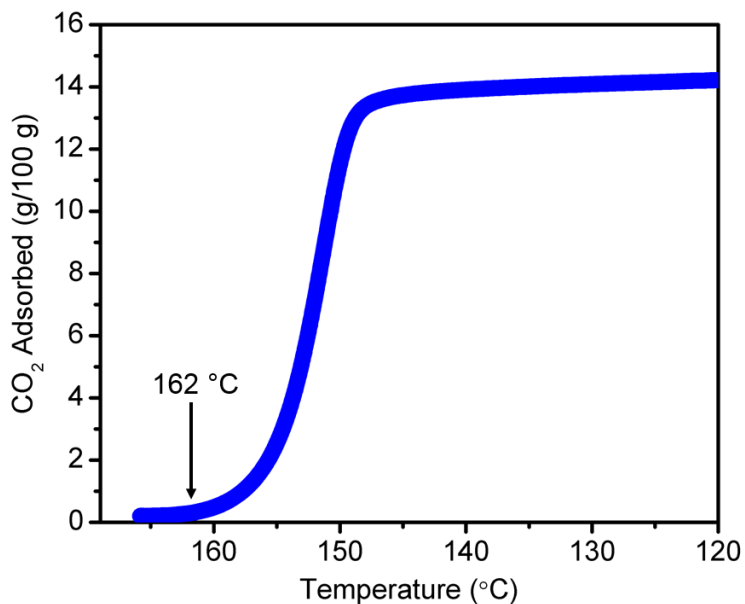


**Figure S6.** Thermogravimetric adsorption (cooling) isobar under pure CO<sub>2</sub> for (±)-dach-(±)-Mg<sub>2</sub>(dobpdc) with a temperature ramp rate of 0.1 °C/min and a flow rate of 100 mL/min, as opposed to the standard flow rate of 25 mL/min used for the other isobars in this manuscript. This faster flow rate was used for calculation of thermodynamic parameters, to facilitate comparison with literature values for other diamine-appended variants. The point of onset for the adsorption step was 162 °C.

**Table S1.** TGA isobar step temperatures and thermodynamic parameters for previously published diamine-appended variants of Mg<sub>2</sub>(dobpdc)

<b>Diamine</b>	<b>TGA isobar step temperature (°C)</b>	<b>−Δ<i>h</i><sub>ads</sub> (kJ/mol)</b>	<b>−Δ<i>s</i><sub>ads</sub> (J/mol·K)</b>
<i>N,N'</i> -diethylethylenediamine <sup>1</sup>	153	100 ± 4	228 ± 10
<i>N</i> -methylethylenediamine <sup>1</sup>	140	96 ± 3	227 ± 10
<i>N</i> -ethylethylenediamine <sup>1</sup>	125	84 ± 3	186 ± 14
<i>N</i> -isopropylethylenediamine <sup>1</sup>	115	82 ± 3	203 ± 8
<i>N,N'</i> -dimethylethylenediamine <sup>1</sup>	128	79 ± 1	187 ± 2
1,3-diaminopropane <sup>2</sup>	117	76 ± 2	186 ± 6
2-methyl-1,3-diaminopropane <sup>2</sup>	119	71 ± 4	167 ± 12
1,1-dimethyl-1,2-ethylenediamine <sup>2</sup>	85	63 ± 4	161 ± 13
<i>N,N</i> -dimethylethylenediamine <sup>1</sup>	59	52 ± 1	146 ± 2
<i>N,N</i> -diethylethylenediamine <sup>1</sup>	60	49 ± 4	141 ± 13

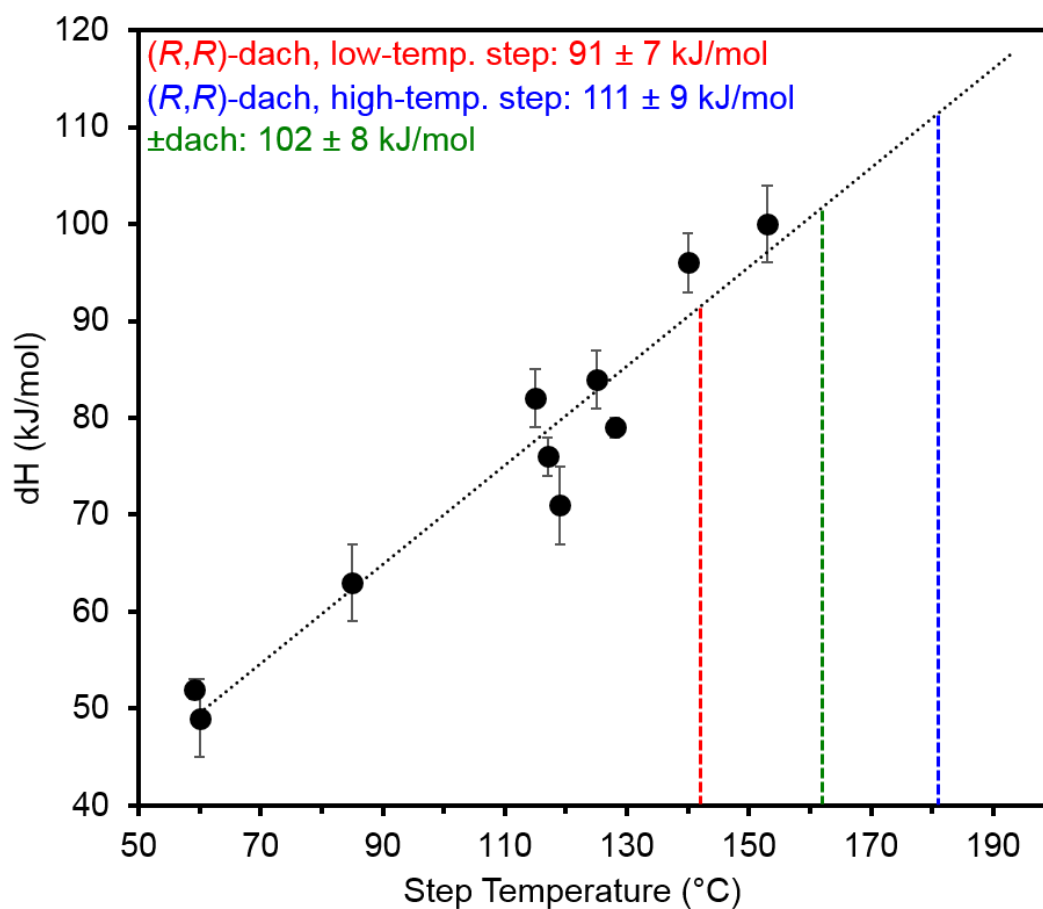


**Figure S7.** Estimation of CO<sub>2</sub> adsorption enthalpies for the high- and low-temperature steps of (*R,R*)-dach-(±)-Mg<sub>2</sub>(dobpdc), and for the single step exhibited by (±)-dach-(±)-Mg<sub>2</sub>(dobpdc). Each black dot on the plot represents a previously published diamine-appended variant of Mg<sub>2</sub>(dobpdc). The color-coded vertical lines represent the step temperatures observed in TGA adsorption isobars. From the points of intersection with the trend line, approximate adsorption enthalpies can be calculated. This method assumes that dach-(±)-Mg<sub>2</sub>(dobpdc) variants follow the trend exhibited by the other diamines.



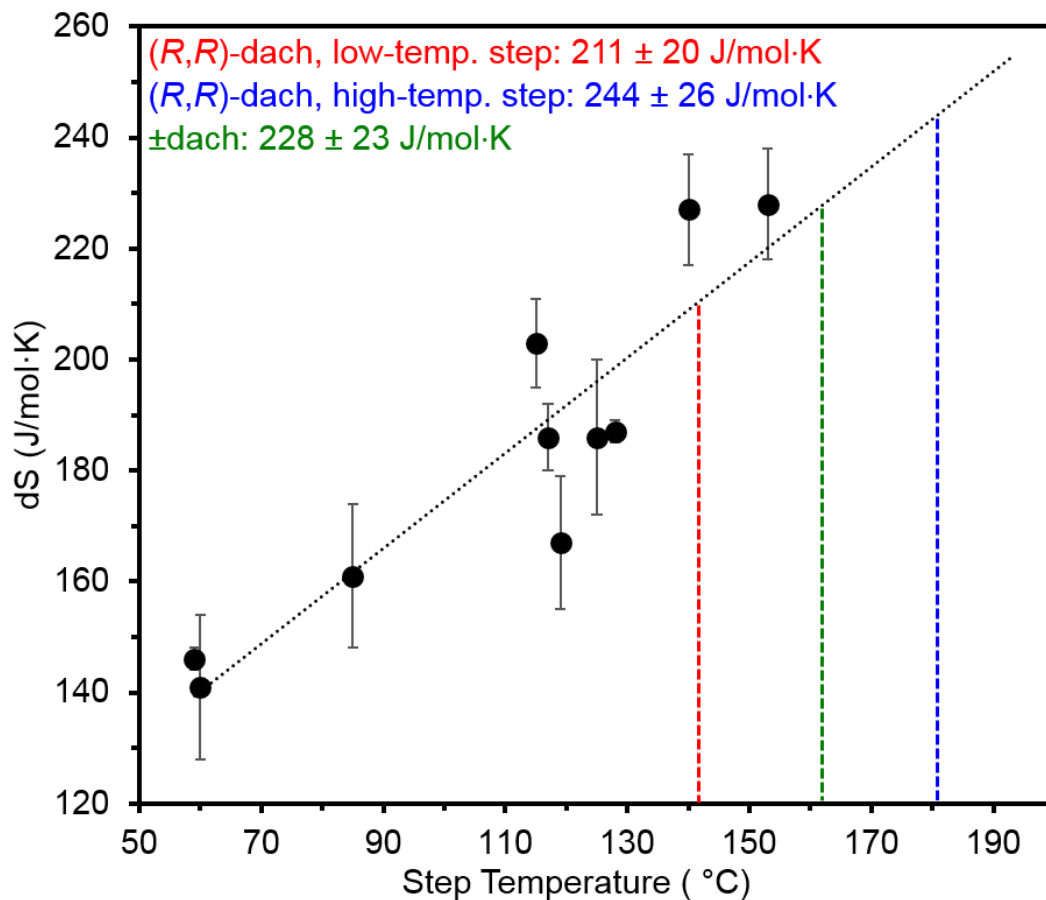


**Figure S8.** Estimation of CO<sub>2</sub> adsorption entropies for the high- and low-temperature steps of (*R,R*)-dach–(±)-Mg<sub>2</sub>(dobpdc), and for the single step exhibited by (±)-dach–(±)-Mg<sub>2</sub>(dobpdc). Each black dot on the plot represents a previously published diamine-appended variant of Mg<sub>2</sub>(dobpdc). The color-coded vertical lines represent the step temperatures observed in TGA adsorption isobars. From the points of intersection with the trend line, approximate CO<sub>2</sub> adsorption entropies can be calculated.

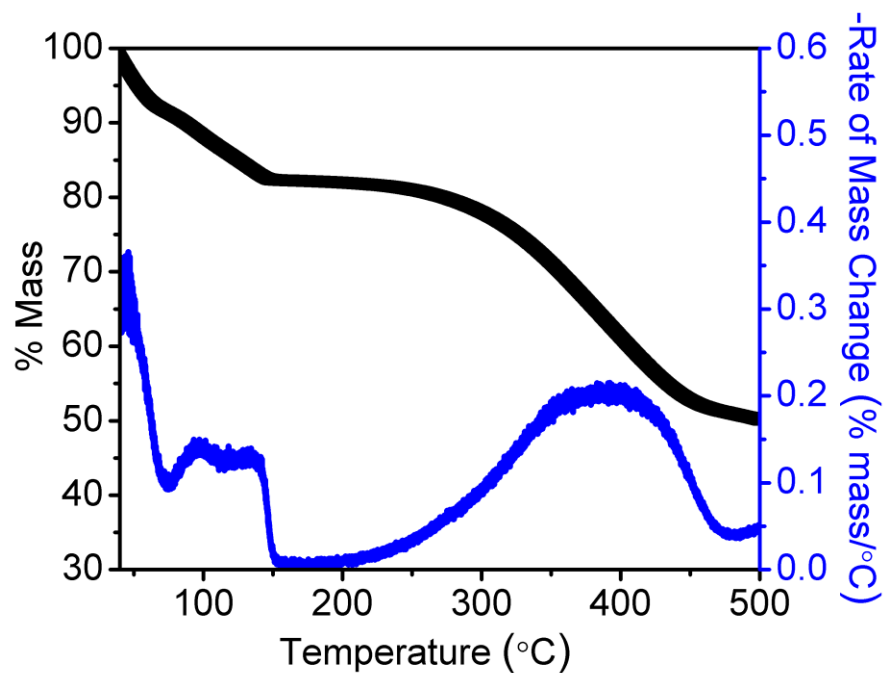


**Figure S9.** Thermogravimetric decomposition trace (black) and negative derivative decomposition trace (“-Rate of Mass Change”, blue) for (±)-dach-(±)-Mg<sub>2</sub>(dobpdc). A ramp rate of 3 °C/min was used. The initial transition below 70 °C can be attributed to loss of loosely bound toluene solvent molecules. The transition from ~80–130 °C can be attributed to loss of strongly bound solvent molecules, such as water or excess diamine, and CO<sub>2</sub> (this adsorbent can capture CO<sub>2</sub> from air). The transition occurring from ~200–450 °C can be attributed to diamine loss.

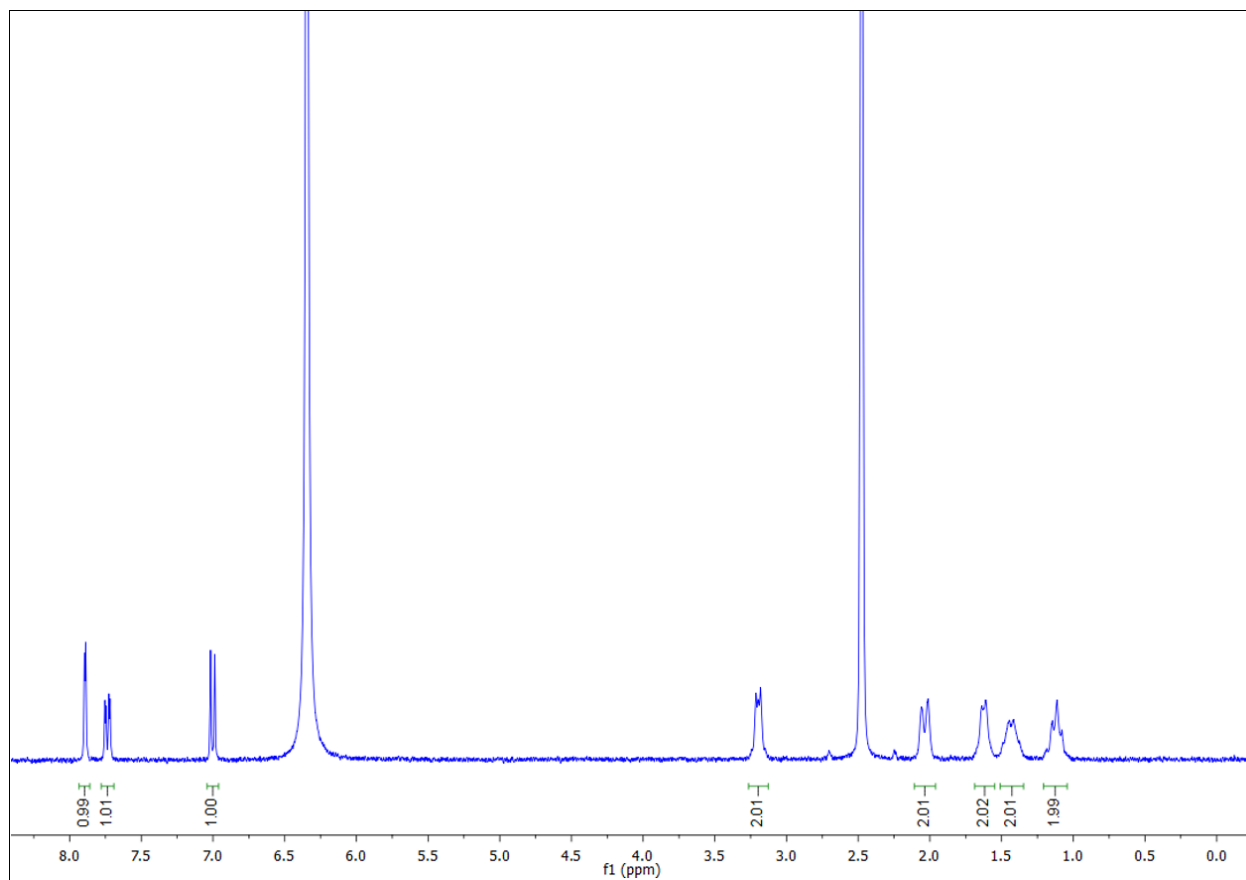


**Figure S10.**  $^1\text{H}$  NMR spectrum of acid-digested (*R,R*)-dach-( $\pm$ )- $\text{Mg}_2(\text{dobpdc})$  after collection thermogravimetric analysis  $\text{CO}_2$  adsorption isobars ( $\text{DMSO-}d_6$ ). The peaks between  $\sim 7.0$ – $8.0$  ppm correspond to  $\text{H}_4\text{dobpdc}$ . The peak at 2.5 ppm corresponds to DMSO, and the peak at 6.3 ppm corresponds to  $\text{H}_3\text{O}^+$ . The molar ratio of dach: $\text{H}_4\text{dobpdc}$  in this sample is 2:1, indicating a diamine loading of 1 per metal site in  $\text{Mg}_2(\text{dobpdc})$ , or 100%. This spectrum was obtained using a Bruker AV-300 MHz NMR instrument.

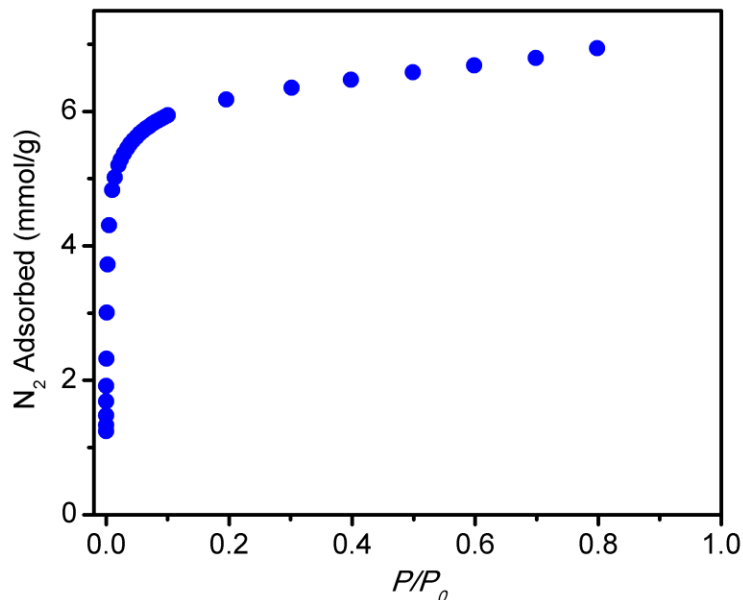


**Figure S11.** 77 K  $N_2$  adsorption isotherm of activated (*R,R*)-dach-( $\pm$ )- $Mg_2$ (dobpdc). Fitting these data yielded a Brunauer–Emmett–Teller surface area of  $528 \pm 2 \text{ m}^2/\text{g}$ .

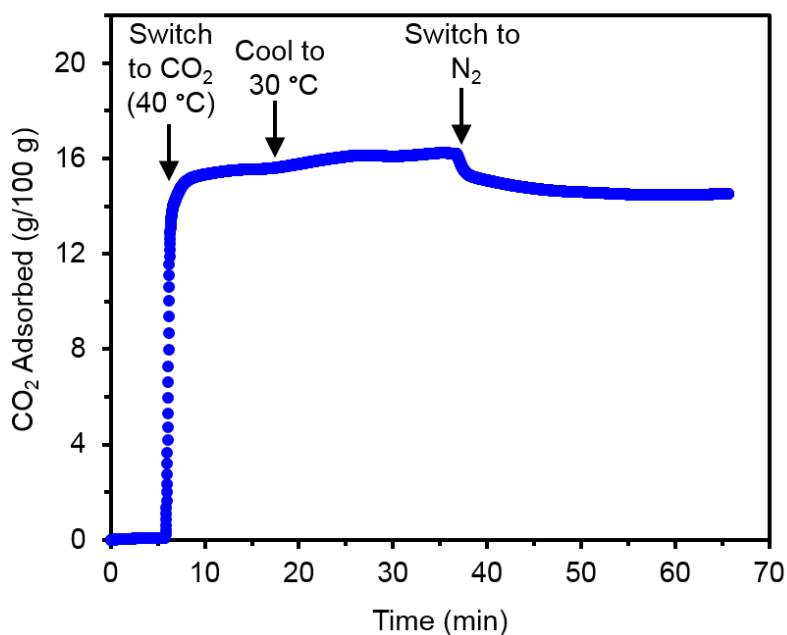


**Figure S12.** Thermogravimetric analysis of ( $\pm$ )-dach-( $\pm$ )- $Mg_2$ (dobpdc) demonstrating retention of adsorbed  $CO_2$  under flowing  $N_2$  at  $30 \text{ }^\circ\text{C}$ . The sample was activated at  $180 \text{ }^\circ\text{C}$  under flowing  $N_2$  for 20 min, then cooled to  $40 \text{ }^\circ\text{C}$  under  $N_2$ . At the time point indicated on the plot, the gas stream was switched to pure  $CO_2$ . After 10 min, the sample was cooled to  $30 \text{ }^\circ\text{C}$  and held isothermally. Finally, the gas stream was switched back to  $N_2$ , and the sample was held isothermally for 30 min. A small amount of  $CO_2$ , presumably bound to the framework through physisorption, desorbed from the sample, but the majority of the  $CO_2$  did not desorb.

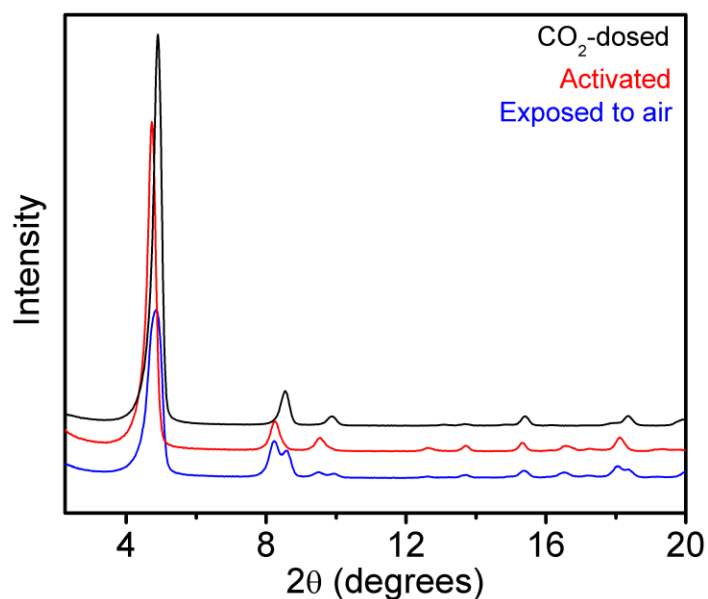


**Figure S13.** Powder X-ray diffraction patterns ( $\lambda = 1.5418 \text{ \AA}$ ) collected at 298 K for (*S,S*)-dach-( $\pm$ )-Mg<sub>2</sub>(dobpdc) with 13 days of exposure to air after synthesis (blue), after activation (red), and after dosing with CO<sub>2</sub> (black). The air-exposed sample contains two phases, indicating that half of the material has adsorbed CO<sub>2</sub> from air. Activation and CO<sub>2</sub> dosing were performed on a thermogravimetric analyzer, followed immediately by collection of the powder patterns. This adsorbent retains CO<sub>2</sub> upon exposure to N<sub>2</sub> or air at a temperature of 30 °C and at colder temperatures. The powder pattern of the activated sample was collected quickly enough that substantial CO<sub>2</sub> was not adsorbed from air prior to data acquisition.

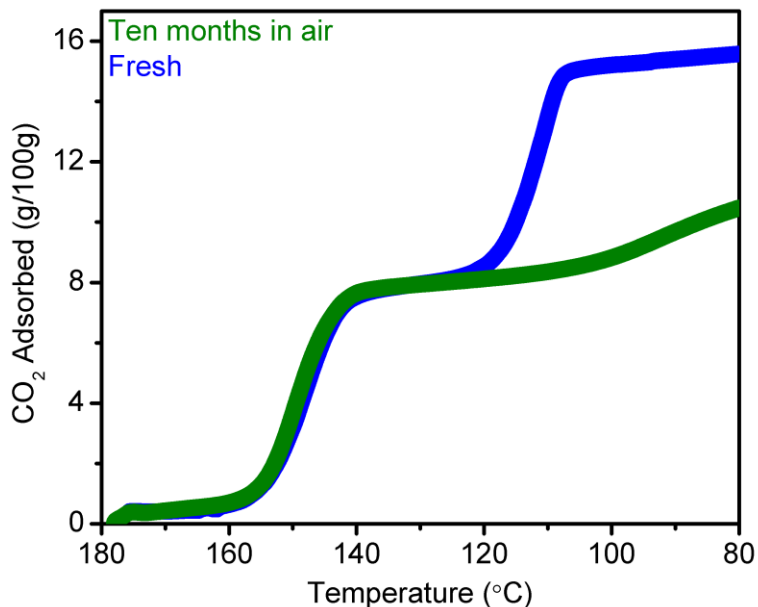


**Figure S14.** Assessment of diamine-appended adsorbent stability in air using thermogravimetric analysis. Thermogravimetric adsorption (cooling) isobars were collected under pure CO<sub>2</sub> for (*S,S*)-dach-(±)-Mg<sub>2</sub>(dobpdc) as-synthesized (blue, “fresh”) and after storage in a vial (sealed by a Teflon-lined screw-on cap to the 20 mL vial) under air for 10 months (green). A temperature ramp rate of 2 °C/min was used. The height and sharpness of the high-temperature adsorption step are unchanged after 10 months, while the low-temperature adsorption step is much broader and shorter, indicating selective diamine loss from one diastereomeric subdomain of the material. As demonstrated in the preceding figure, half of this adsorbent captures CO<sub>2</sub> from air, while the other one does not. We hypothesize that the diastereomeric subdomain of this material that captures CO<sub>2</sub> from air is resistant to diamine loss, owing to the highly stabilized ammonium carbamate chains, while the other subdomain of the material, which lacks adsorbed CO<sub>2</sub>, is more prone to diamine volatilization.

## 2. Characterization of dach–Mg<sub>2</sub>(pc-dobpdc) variants

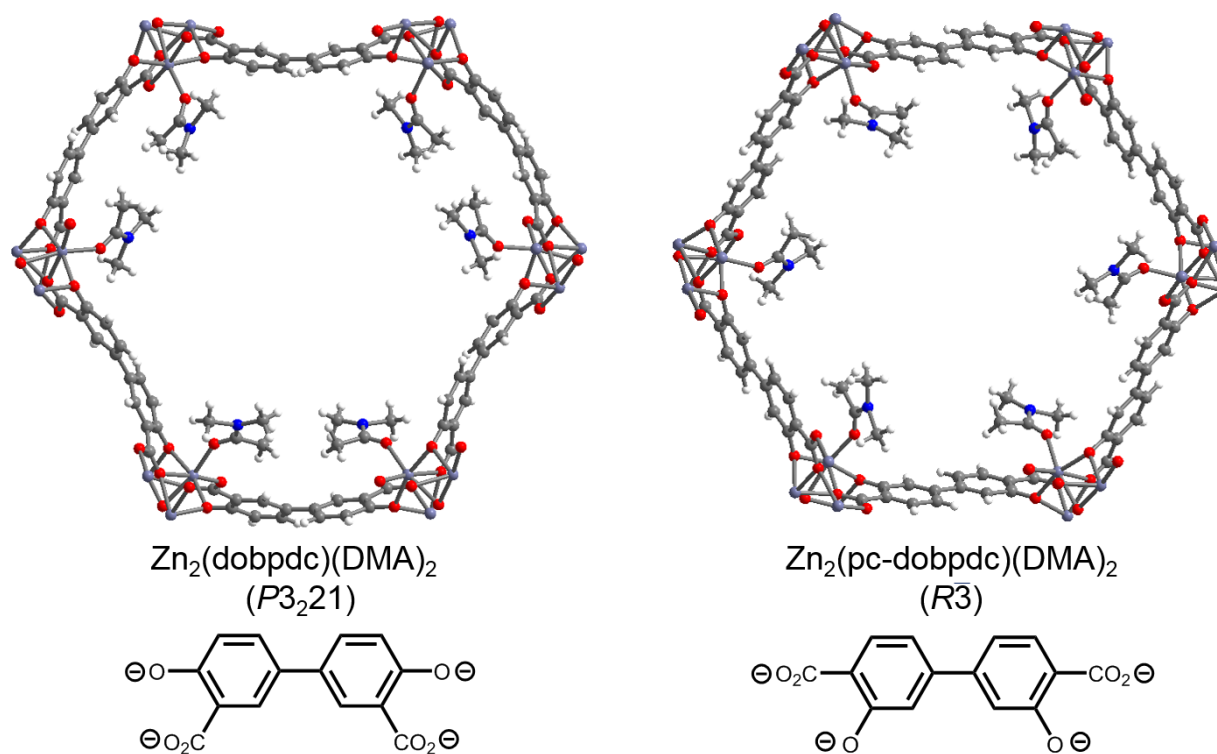


**Figure S15.** Pore views of the crystal structures of DMA-solvated  $\text{Zn}_2(\text{dobpdc})^1$  and  $\text{Zn}_2(\text{pc-dobpdc})^3$  at 100 K. We note that no single-crystal structure is available for  $\text{Mg}_2(\text{pc-dobpdc})$ , but it was reported<sup>4</sup> to exist in the same space group as  $\text{Zn}_2(\text{pc-dobpdc})$ , for which the crystal structure has been determined.<sup>3</sup> The structures of the organic linkers from which these frameworks are assembled,  $\text{dobpdc}^{4-}$  and  $\text{pc-dobpdc}^{4-}$ , respectively, are depicted at the bottom. While these frameworks have very similar pore diameters, they form in different space groups. The  $\text{Zn}_2(\text{dobpdc})$  framework is chiral, adopting either a left-handed ( $P3_221$  space group) or right-handed ( $P3_121$  space group) structure, whereas  $\text{Zn}_2(\text{pc-dobpdc})$  is achiral. Pale purple, red, blue, gray, and white spheres represent Zn, O, N, C, and H atoms, respectively.

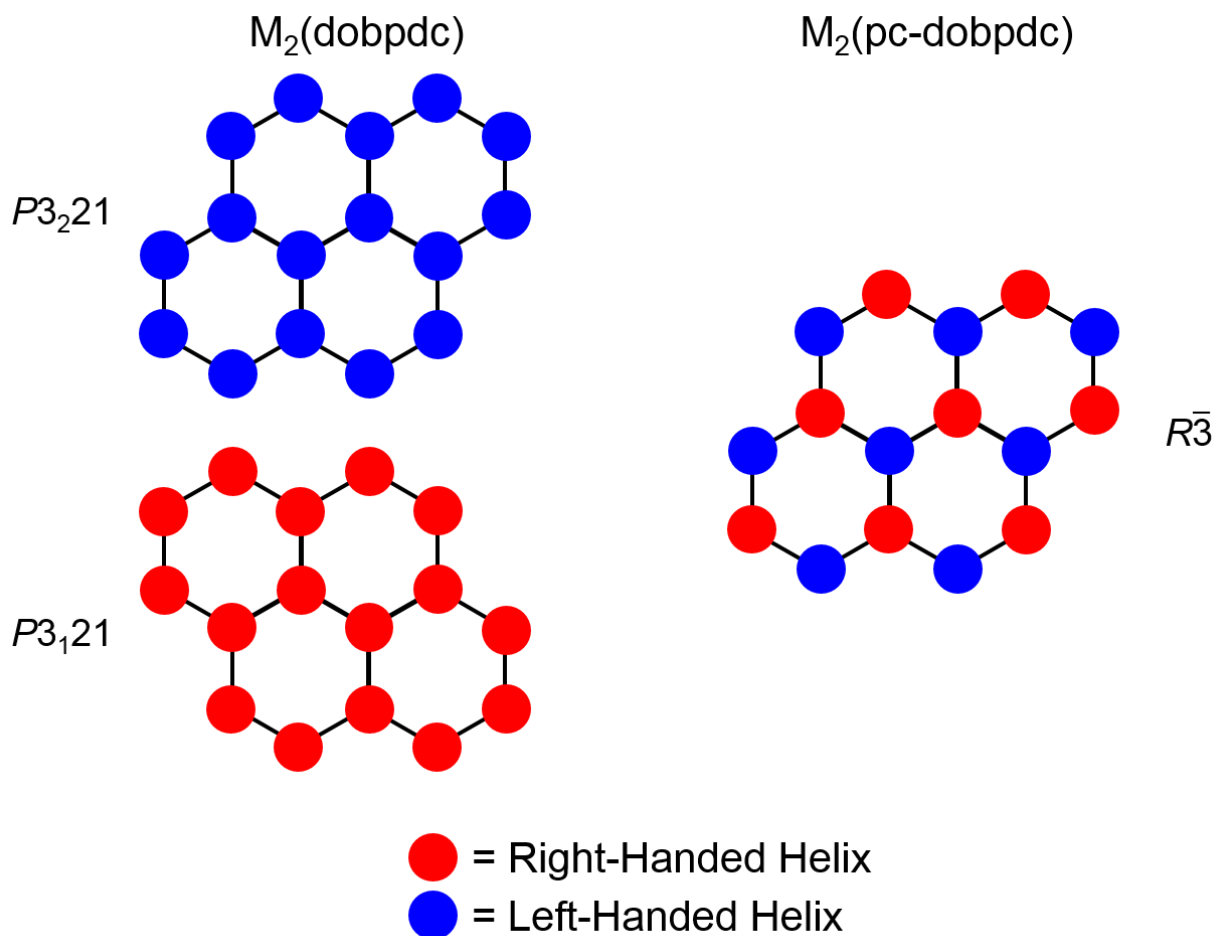


**Figure S16.** Schematic overview of the structures of  $M_2(\text{dobpdc})$  and  $M_2(\text{pc-dobpdc})$ . Both frameworks contain a 50:50 mixture of left- and right-handed helices, but they differ in the arrangement of these helices. The right- and left-handed helices of  $M_2(\text{dobpdc})$  are segregated into separate subdomains, giving rise to two types of enantiomeric pores in the material. In contrast, the helices of  $M_2(\text{pc-dobpdc})$  are arranged in an alternating pattern, leading to only one type of pore and an overall achiral structure.



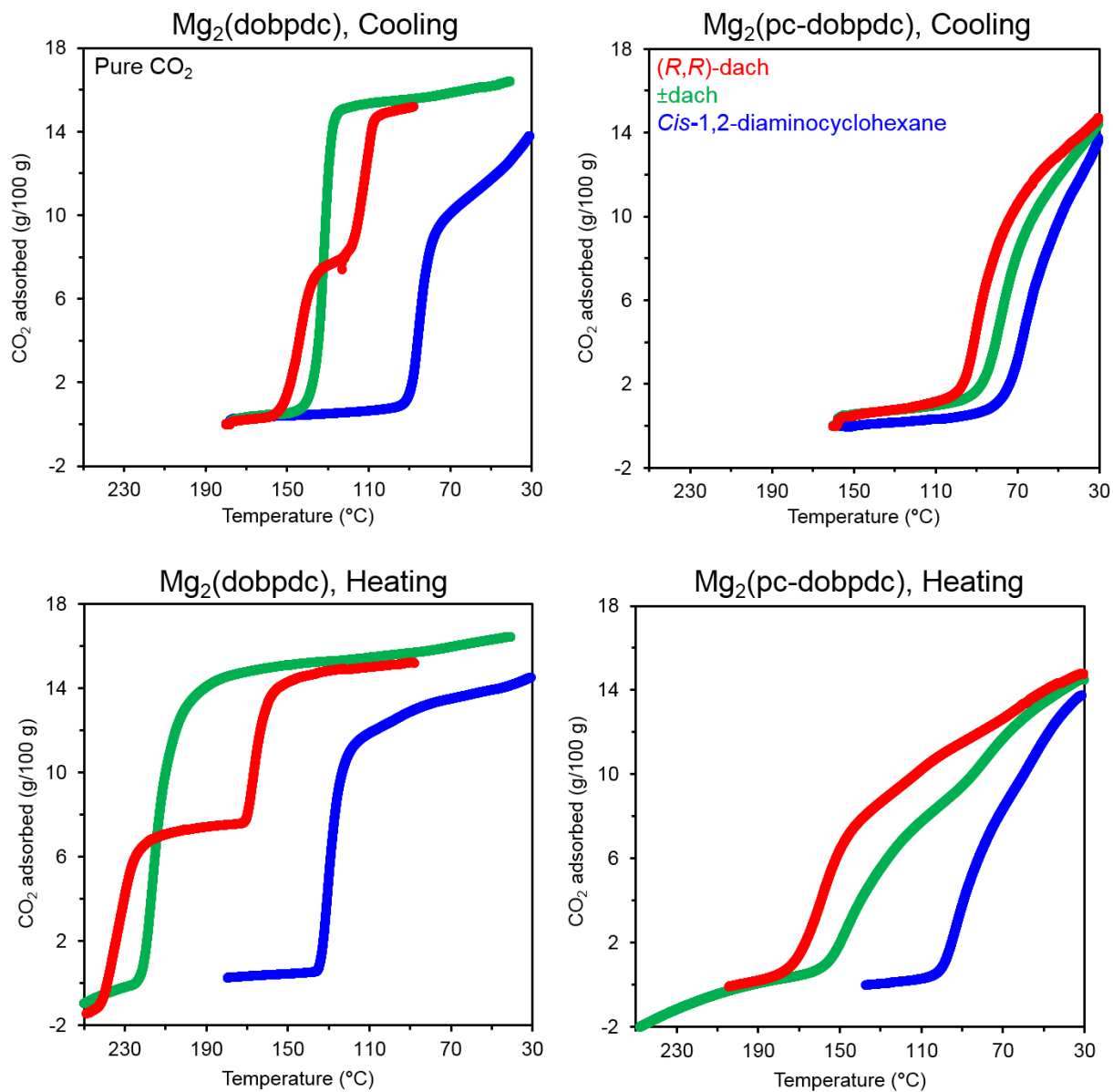


**Figure S17.** Thermogravimetric adsorption (cooling, top two plots) and desorption (heating, bottom two plots) isobars under pure CO<sub>2</sub> for diamine-appended variants of Mg<sub>2</sub>(dobpdc) (two plots at left) and Mg<sub>2</sub>(pc-dobpdc) (two plots at right). Temperature ramp rates of 2 °C/min were used. Each adsorbent was grafted to three 1°,1° diamine analogues of ethylenediamine: (*R,R*)-dach (red), (±)-dach (green), and *cis*-1,2-diaminocyclohexane (blue).

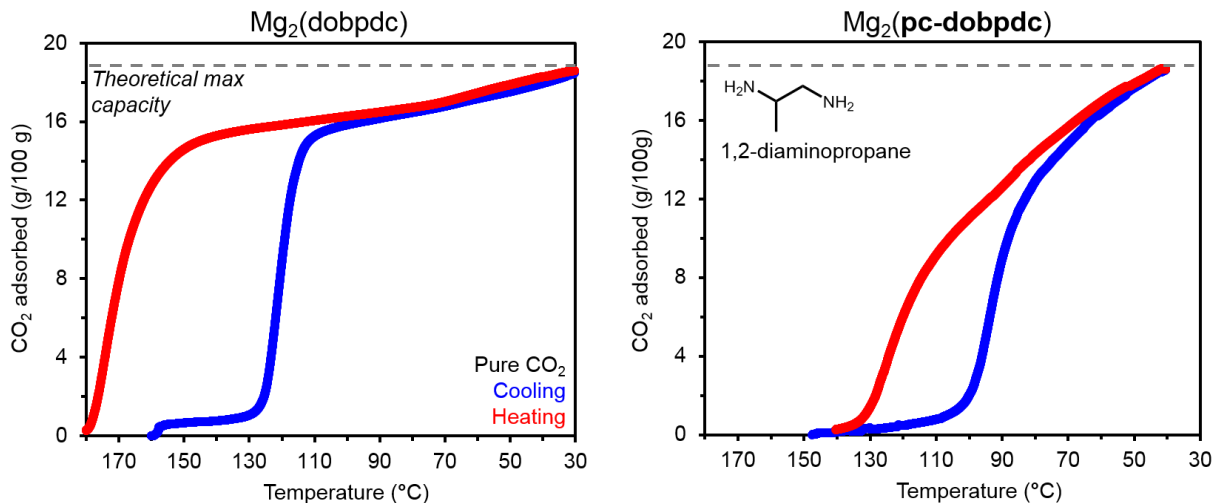


**Figure S18.** Thermogravimetric adsorption (cooling, blue) and desorption (heating, red) isobars under pure CO<sub>2</sub> for Mg<sub>2</sub>(dobpdc) (left) and Mg<sub>2</sub>(pc-dobpdc) (right) grafted with (±)-1,2-diaminopropane. Temperature ramp rates of 2 °C/min were used. The dashed gray lines indicate the CO<sub>2</sub> adsorption capacity expected for 1 CO<sub>2</sub> per Mg<sup>2+</sup>-diamine site. For the Mg<sub>2</sub>(pc-dobpdc) sample, diamine loading was determined to be 100% (1 diamine per Mg<sup>2+</sup>), and the sample was similar in crystallinity to other diamine-appended variants of Mg<sub>2</sub>(pc-dobpdc),<sup>3</sup> as determined by powder X-ray diffraction. Therefore, the short and broad CO<sub>2</sub> adsorption step for (±)-1,2-diaminopropane-Mg<sub>2</sub>(pc-dobpdc) was not caused by poor diamine loading or degradation of the framework structure.

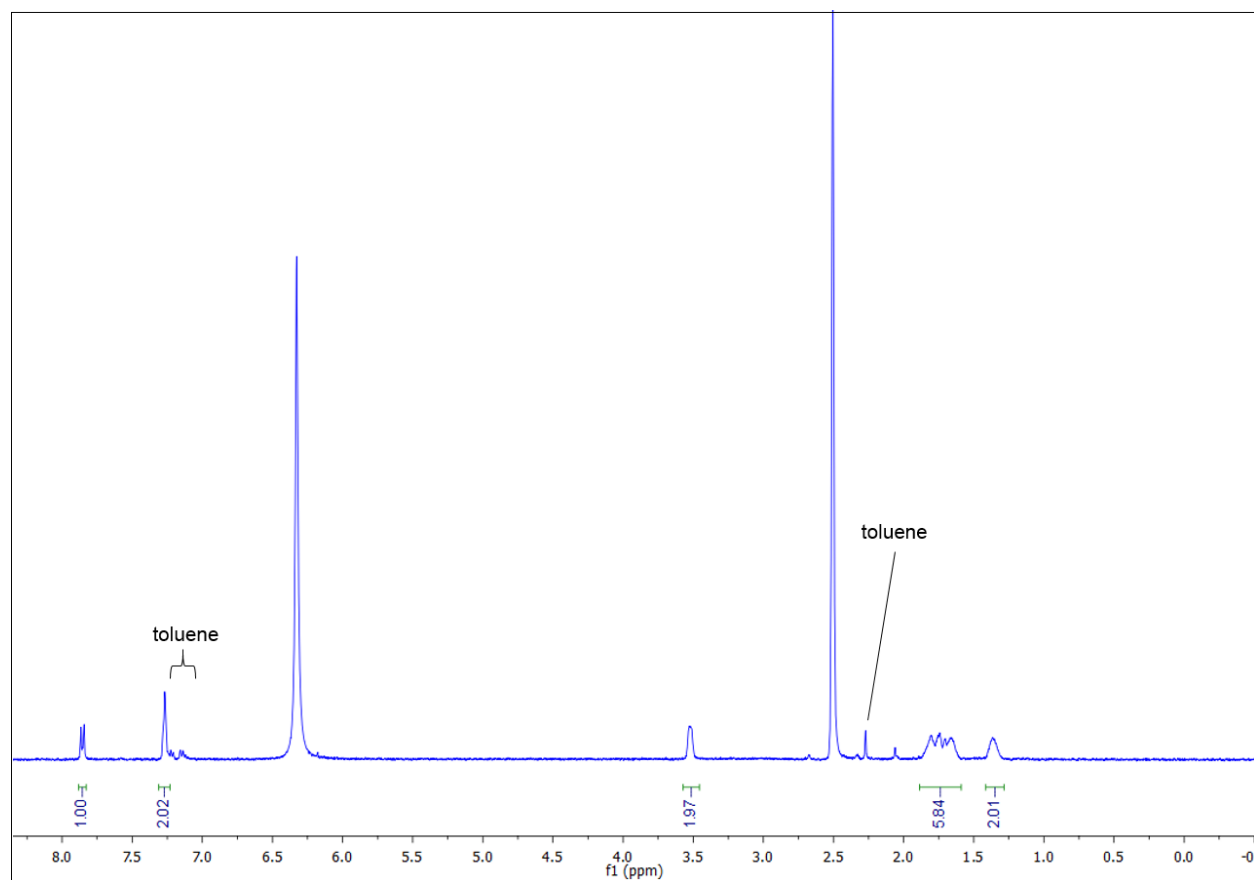


**Figure S19.** <sup>1</sup>H NMR spectrum of acid-digested as-synthesized *cis*-1,2-diaminocyclohexane-Mg<sub>2</sub>(pc-dobpdc) (DMSO-*d*<sub>6</sub>). Toluene was the grafting solvent. The peaks between ~7.3–8.0 ppm correspond to H<sub>4</sub>pc-dobpdc. The peak at 2.5 ppm corresponds to DMSO, and the peak at 6.3 ppm corresponds to H<sub>3</sub>O<sup>+</sup>. The molar ratio of *cis*-1,2-diaminocyclohexane:H<sub>4</sub>pc-dobpdc in this sample is 2:1, indicating a diamine loading of 1 per metal site in Mg<sub>2</sub>(pc-dobpdc), or 100%. This spectrum was obtained using a Bruker AVB-400 instrument.

### 3. Testing diamine mixtures in Mg<sub>2</sub>(dobpdc)

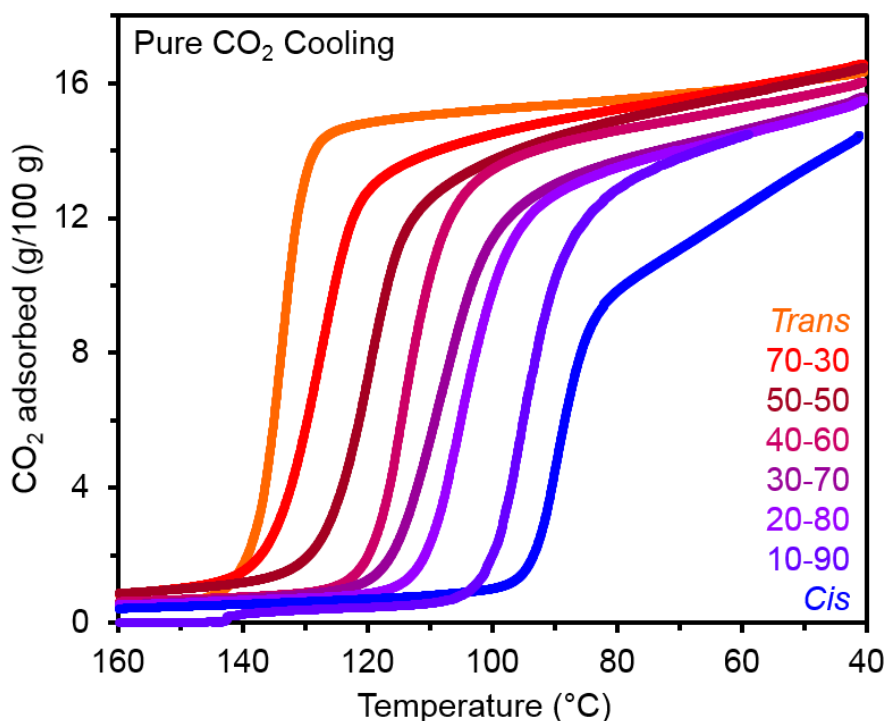


**Figure S20.** Thermogravimetric adsorption (cooling) isobars under pure CO<sub>2</sub> for Mg<sub>2</sub>(dobpdc) grafted with varying ratios of ( $\pm$ )-dach (*trans*-1,2-diaminocyclohexane) and *cis*-1,2-diaminocyclohexane. The purpose of this experiment was to investigate whether adding varying ratios of two 1°,1° diamines with distinct step temperatures could produce an adsorbent exhibiting a single step with intermediate temperature. For all ratios used, a single step, with intermediate temperature between the steps of pure *trans* and pure *cis*, was observed. A temperature ramp rate of 2 °C/min was used. Pure *trans* (orange) and pure *cis* (blue) samples are shown. For the remaining traces, the labels indicate the molar ratios of *trans*:*cis* in the grafting solution, but not necessarily the ratio of isomers grafted to the framework.

**Table S2.** Molar ratio of *trans*:*cis*-1,2-diaminocyclohexane present in the grafting solution and actual ratio grafted to Mg<sub>2</sub>(dobpdc).

<i>trans/cis</i> ratio added	Actual <i>trans/cis</i> ratio grafted to Mg <sub>2</sub> (dobpdc) determined by <sup>1</sup> H NMR after digest
70:30	73:27
50:50	53:47
10:90	21:79

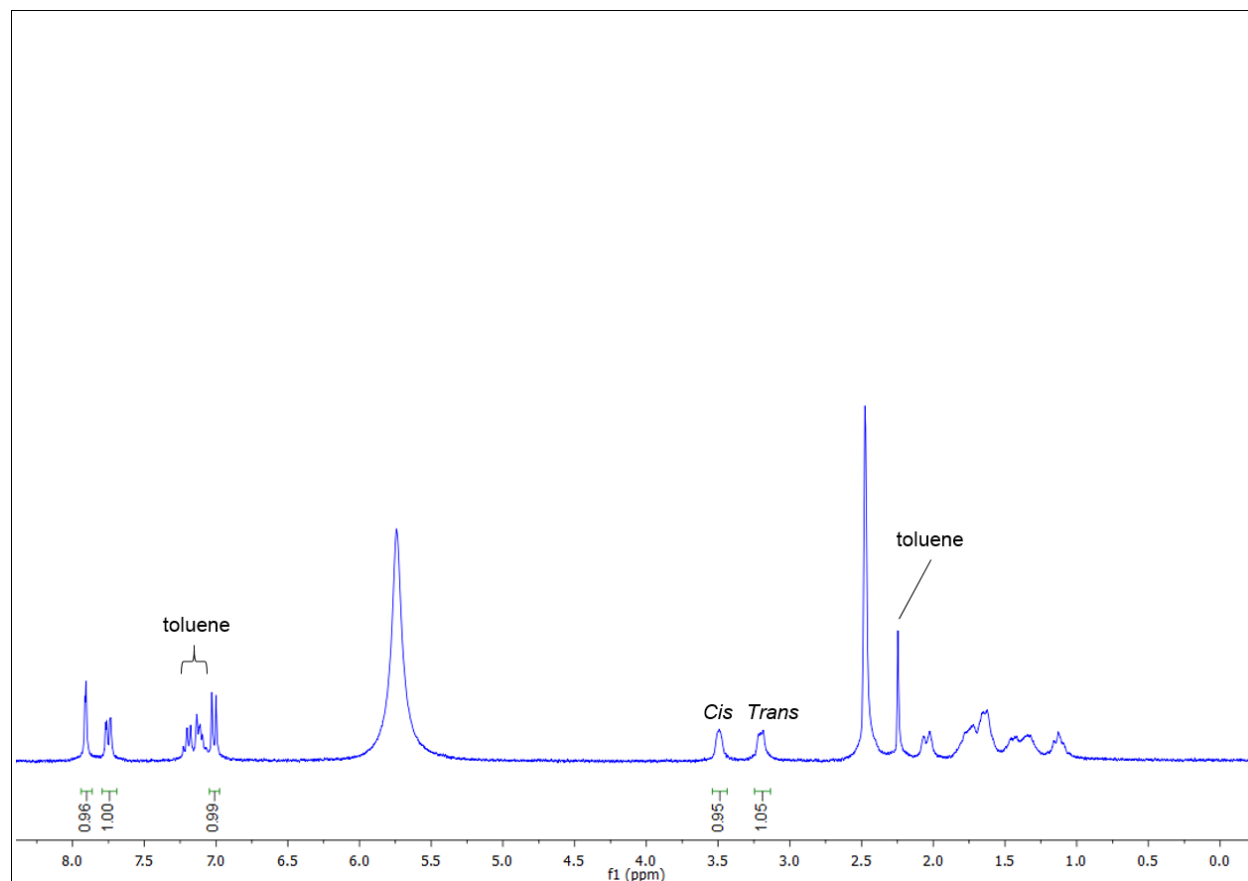


**Figure S21.**  $^1\text{H}$  NMR spectrum of acid-digested as-synthesized  $\text{Mg}_2(\text{dobpdc})$  grafted with a 50:50 molar ratio of ( $\pm$ )-dach (*trans*-1,2-diaminocyclohexane):*cis*-1,2-diaminocyclohexane ( $\text{DMSO-}d_6$ ). Toluene was the grafting solvent. The peak at 2.5 ppm corresponds to DMSO, and the peak at 6.3 ppm corresponds to  $\text{H}_3\text{O}^+$ . The molar ratio of ( $\pm$ )-dach (*trans*-1,2-diaminocyclohexane):*cis*-1,2-diaminocyclohexane grafted to  $\text{Mg}_2(\text{dobpdc})$  was 53:47, judging from integration of the peaks at  $\sim 3.2$  ppm and  $\sim 3.5$  ppm, respectively. Overall diamine loading was 1 per metal site in  $\text{Mg}_2(\text{dobpdc})$ , or 100%. This spectrum was obtained using a Bruker AV-300 MHz NMR instrument.

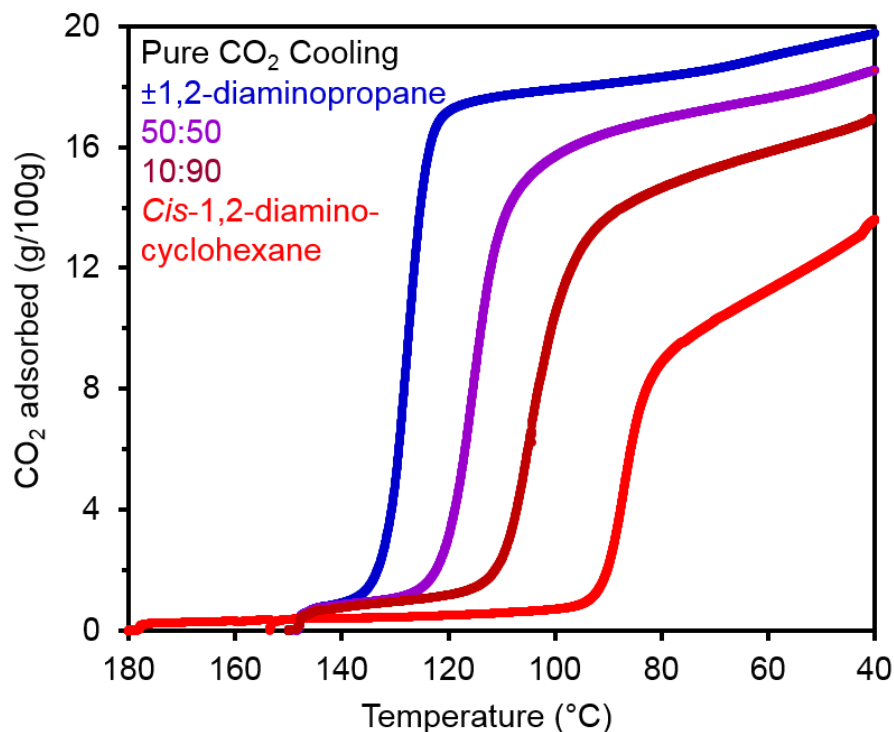


**Figure S22.** Thermogravimetric adsorption (cooling) isobars under pure CO<sub>2</sub> for Mg<sub>2</sub>(dobpdc) grafted with varying ratios of (±)-1,2-diaminopropane and *cis*-1,2-diaminocyclohexane. The purpose of this experiment was to investigate whether adding varying ratios of two 1°,1° diamines with distinct step temperatures could produce an adsorbent exhibiting a single step with intermediate temperature. For all ratios used, a single step with intermediate temperature was observed. A temperature ramp rate of 2 °C/min was used. Pure (±)-1,2-diaminopropane (blue) and pure *cis*-1,2-diaminocyclohexane (red) samples are shown. For the remaining traces, the labels indicate the molar ratios of (±)-1,2-diaminopropane:*cis*-1,2-diaminocyclohexane in the initial grafting solution, but not necessarily the ratio of isomers grafted to the framework.

#### 4. Dach-Zn<sub>2</sub>(dobpdc) single-crystal structure and CO<sub>2</sub> adsorption properties

**Procedure for single-crystal X-ray diffraction.** For the CO<sub>2</sub>-inserted (±)-dach-Zn<sub>2</sub>(dobpdc) structure, diamine-appended single crystals were transferred to a glass measurement tube, sealed with a Micromeritics *Transeal*, and heated *in vacuo* at 100 °C for 1 h on an ASAP 2420 gas adsorption instrument. The sample was then transferred air-free to the analysis port of the instrument and dosed with 1100 mbar CO<sub>2</sub>. The tube was sealed under CO<sub>2</sub>, removed from the manifold, and stored over dry ice for 3 h. Immediately after opening the tube, the crystals were coated with Paratone oil, and a single crystal was rapidly mounted and flash-cooled to 100 K using an Oxford Cryosystems cryostream prior to data collection. Single crystals of Zn<sub>2</sub>(dobpdc)(DMA)<sub>2</sub> synthesized in the presence of D-panthenol were coated with Paratone oil and mounted onto MiTeGen loops.

All single-crystal X-ray diffraction data were collected at Beamline 11.3.1 at the Advanced Light Source, Lawrence Berkeley National Laboratory using synchrotron radiation ( $\lambda = 0.8856 \text{ \AA}$  and  $0.7749 \text{ \AA}$ ) using a Bruker AXS D8 diffractometer equipped with a Bruker PHOTON 100 CMOS detector. Structures were collected at 100 K using an Oxford Cryosystems Cryostream 700 Plus. The structure of CO<sub>2</sub>-inserted ( $\pm$ )-dach-Zn<sub>2</sub>(dobpdc) was refined as an inversion twin in space group  $P3_221$  based on Flack parameter values near 0.5. All structures for Zn<sub>2</sub>(dobpdc)(DMA)<sub>2</sub> single crystals synthesized in the presence of D-panthenol were refined as inversion twins in the space group  $P3_121$  as these gave Flack parameter values that ranged from 0.40(2)–0.50(5) in this space group. Raw data were corrected for Lorentz and polarization effects using Bruker AXS SAINT software<sup>5</sup> and were corrected for absorption using SADABS.<sup>6</sup> The structures were solved using SHELXT<sup>7</sup> and refined using SHELXL<sup>8</sup> operated in the OLEX2<sup>9</sup> interface. Thermal parameters were refined anisotropically for all non-hydrogen atoms. All hydrogen atoms were placed geometrically and refined using a riding model.

For the structure of ( $\pm$ )-dach-Zn<sub>2</sub>(dobpdc) without CO<sub>2</sub>, the appended diamines were too disordered to be modeled. Nonetheless, the framework structure and bound amine could be clearly identified. The same sample of diamine-appended crystals was used to obtain the CO<sub>2</sub>-inserted structure, thus confirming the presence of diamine in the structure prior to insertion. Although the free diamine structure could not be fully refined, the unit cell parameters are provided in the main text for comparison to those of the contracted, CO<sub>2</sub>-inserted phase.

For the structure of Zn<sub>2</sub>(dobpdc)(( $\pm$ )-dach-CO<sub>2</sub>)<sub>2</sub>, the ammonium carbamate chains fully occupy the Zn sites within the pores, and both enantiomers of the diamine were resolved in the asymmetric unit. The occupancies of each enantiomer were freely refined and indicate 53(2)% occupancy of (1*S*,2*S*)-(+)-1,2-diaminocyclohexane (part 1, atoms with suffix A indicated in the .cif file) and 47(2)% occupancy of (1*R*,2*R*)-(-)-1,2-diaminocyclohexane (part 2, atoms with suffix B indicated in the .cif file). The occupancies were fixed in the final refinement. The crystal was refined as an inversion twin in space group  $P3_221$  with a twin fraction of 0.41(3). The carbamate unit (O4, C8, O5, and N1), ammonium (N2), and two carbon atoms of the cyclohexane ring (C11 and C14) are shared in both conformations of the ammonium carbamate chains. Distance (SADI for C–C and C–N bonds) and displacement parameter (RIGU) restraints were required in the refinement of the disordered ammonium carbamate chains.

**Procedure for diamine grafting to Zn<sub>2</sub>(dobpdc) polycrystalline powder.** Thermogravimetric analysis of diamine-appended Zn<sub>2</sub>(dobpdc) (Figure S23) was performed using samples prepared from polycrystalline Zn<sub>2</sub>(dobpdc) powder synthesized in bulk following a previously published procedure.<sup>1</sup>

For grafting of ( $\pm$ )-dach, the methanol supernatant of washed and methanol-solvated Zn<sub>2</sub>(dobpdc) powder was carefully decanted and immediately replaced with 10 mL toluene, and the sample was allowed to incubate for 5 min at room temp. The supernatant was replaced with fresh toluene twice following the same procedure. The supernatant was finally replaced with a 20% (v/v) solution of ( $\pm$ )-dach in toluene and allowed to incubate for 18 h at room temperature. No effort was made to remove trace water from the ( $\pm$ )-dach solution. After the 18 h period, the supernatant was decanted, replaced with 10 mL toluene, and allowed to incubate for 5 min at room temperature. The toluene was exchanged two times with fresh toluene, followed by three replacements of the supernatant with hexanes, using the same decanting procedure at room temperature. At no point was the sample allowed to become dry, since allowing the sample to dry can result in loss of crystallinity and porosity. The washed ( $\pm$ )-dach-grafted sample was immediately analyzed by TGA. Digestion of the powder and analysis by <sup>1</sup>H NMR spectroscopy revealed 100% loading of ( $\pm$ )-dach for the hexanes-washed sample (1 dach per metal site).

For (*R,R*)-dach, a rigorously air-free procedure was used to determine if higher CO<sub>2</sub> capacities could be obtained for the diamine-appended zinc framework in the absence of oxygen and moisture. In this procedure, a smaller concentration and number of equivalents of diamine was also used to minimize risk of diamine-induced degradation of the material. The enantiopure diamine was first dried over sodium metal under an Ar atmosphere. The dry diamine was then distilled with gentle heating using a heat gun. The dry diamine was subsequently stored in a N<sub>2</sub>-filled glovebox. A 30 mg portion of Zn<sub>2</sub>(dobpdc) was transferred to the glovebox following complete desolvation under dynamic vacuum at 250 °C for 12 h. In an atmosphere free of coordinating solvents, the activated Zn<sub>2</sub>(dobpdc) powder was submerged in 16.2 mL of 0.25% (v/v) solution of (*R,R*)-dach in toluene (2.25 equiv dach per metal site). The solution was prepared by first melting the solid (*R,R*)-dach on a heat plate at 120 °C for 10 s prior to mixing with toluene. The sample was allowed to incubate 4 h at room temperature. Following grafting, the supernatant was removed by pipette and replaced with fresh toluene. The sample was heated at 80 °C for 30 min, after which the supernatant was again removed and replaced with fresh toluene. A total of three toluene washes were performed at 80 °C, with the second and third washes performed for 10 min each. Next, the supernatant was removed and replaced three times with hexanes (room temperature; 5 min per wash). All washes were performed with dry solvent in a N<sub>2</sub>-filled glovebox in an atmosphere free of coordinating solvents. The powder was stored in the glovebox under dry hexanes until use.

The (*R,R*)-dach–Zn<sub>2</sub>(dobpdc) powder synthesized under air-free conditions was analyzed by thermogravimetric analysis using an air-free procedure. A pre-tared aluminum analysis pan and carrier were cycled into the glovebox. Approximately 5 mg of (*R,R*)-dach–Zn<sub>2</sub>(dobpdc) was loaded into the carrier as a slurry and was covered with dry hexanes. The pan and carrier were then quickly removed from the glovebox in a vial sealed under N<sub>2</sub>. The sample was rapidly loaded into the N<sub>2</sub>-filled furnace of the thermogravimetric analyzer prior to evaporation of the hexanes. The sample was then analyzed for isobaric CO<sub>2</sub> adsorption following the same procedure specified for other diamine-appended samples. Digestion of the powder and analysis by <sup>1</sup>H NMR revealed a loading of 1 dach per metal site. The CO<sub>2</sub> capacity measured under pure CO<sub>2</sub> matched that of the (±)-dach-appended sample prepared in air, suggesting that the low capacities observed for dach-appended zinc frameworks result from kinetic barriers or from diamine-induced degradation of the powder.

#### **Procedure for Pawley and Rietveld refinement of samples of (±)-dach grafted to Mg<sub>2</sub>(dobpdc).**

The analysis of the diffraction data, including pattern indexing, profile fitting, crystal structure analysis and Rietveld refinement, was performed with TOPAS 4.1.<sup>10</sup> Pawley fitting<sup>11</sup> using the *P3<sub>2</sub>21* space group (Figure S57) resulted in accurate unit cell parameters for activated (±)-dach–*R*-Mg<sub>2</sub>(dobpdc), which are listed in Table S5. During the fitting of the lattice parameters, profile parameters (strain, stress, instrumental parameters, zero-error shift) and background (Chebyshev polynomial of 10th order) were also refined.

For the (±)-dach–*R*-Mg<sub>2</sub>(dobpdc) analogues, only the crystal structure of the CO<sub>2</sub>-inserted phase could be determined. This structure was solved by methods similar to those described for (*R,R*)-dach–*R*-Mg<sub>2</sub>(dobpdc) and (*S,S*)-dach–*R*-Mg<sub>2</sub>(dobpdc) in Section 9 below, in that the model determined by single-crystal X-ray diffraction for the CO<sub>2</sub>-inserted (±)-dach–*R*-Zn derivative was applied in the Rietveld refinement of the Mg derivative. Due to pronounced thermal motion of the amines, together with the conformational disorder and the lower resolution compared to the single-crystal measurements, unconstrained refinement was not possible. Instead, the fractional coordinates were kept fixed during the Rietveld refinement, with all of the remaining parameters set free. The final Rietveld plot is given in Figure S24. The refined unit cell parameters, as well as the resulting figures-of-merit, are given in Table S5. The



Rietveld refinement of CO<sub>2</sub>-inserted ( $\pm$ )-dach-*R*-Mg<sub>2</sub>(dobpdc) confirms that it is isostructural to CO<sub>2</sub>-inserted ( $\pm$ )-dach-*R*-Zn<sub>2</sub>(dobpdc).

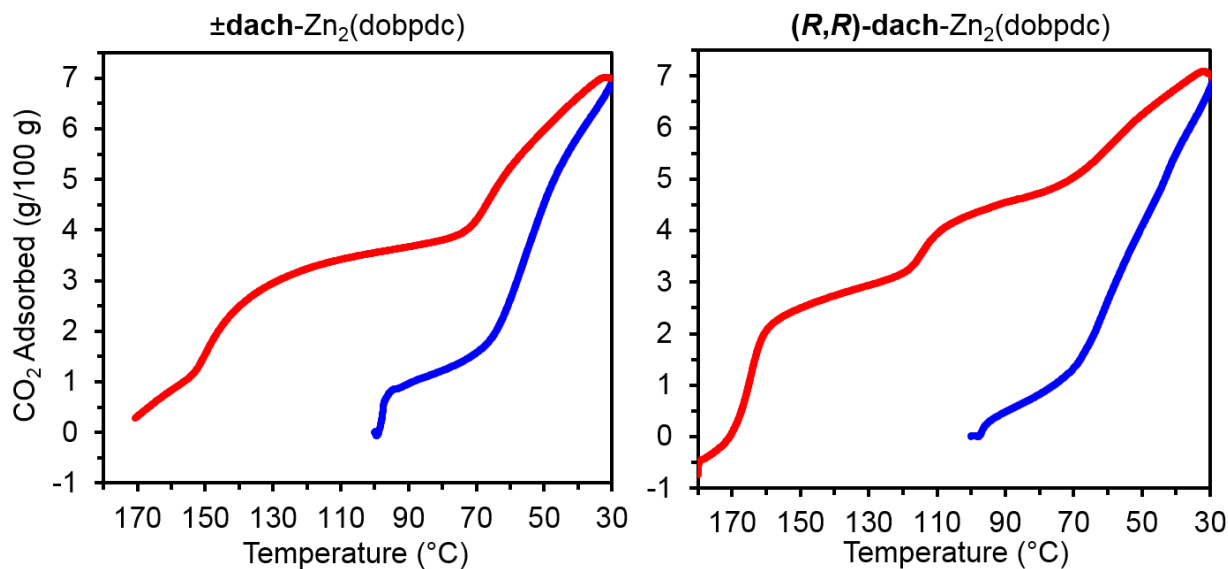


**Figure S23.** Thermogravimetric adsorption (cooling) and heating (red) pure CO<sub>2</sub> isobars for Zn<sub>2</sub>(dobpdc) polycrystalline powder grafted with ( $\pm$ )-dach (left) or (*R,R*)-dach (right). A temperature ramp rate of 2 °C/min was used. The samples were activated at 100 °C under flowing N<sub>2</sub>, then the gas stream was switched to pure CO<sub>2</sub>. Samples were cooled to 30 °C, then heated under pure CO<sub>2</sub>. The CO<sub>2</sub> adsorption capacities exhibited by these samples are much lower than the theoretical maximum (14.0 g/100 g). However, digestion of the samples followed by <sup>1</sup>H NMR spectroscopy revealed a diamine loading of 1 diamine per metal site. The suboptimal capacity could be due to slow adsorption kinetics or loss of porosity in the framework upon diamine grafting.

**Table S3. Crystallographic Data**

Parameter	Zn <sub>2</sub> (dobpdc)((±)-dach-CO <sub>2</sub> ) <sub>2</sub>
Formula	C <sub>28</sub> H <sub>34</sub> N <sub>4</sub> O <sub>10</sub> Zn <sub>2</sub>
Temperature (K)	100(2)
Crystal System	Trigonal
Space Group	<i>P</i> 3 <sub>2</sub> 21
a, b, c (Å)	20.6012(7), 20.6012(7), 6.8939(3)
α, β, γ (°)	90, 90, 120
V (Å <sup>3</sup> )	2533.8(2)
Z	3
Radiation, λ (Å)	Synchrotron, 0.8856
2θ Range for Data Collection (°)	4.928 to 68.152
Completeness to 2θ	99.9% (2θ = 64.194°)
Data / Restraints / Parameters	3597 / 169 / 236
Goodness of Fit on F <sup>2</sup>	1.182
R1 <sup>a</sup> , wR2 <sup>b</sup> (I>2σ(I))	0.0566, 0.1377
R1 <sup>a</sup> , wR2 <sup>b</sup> (all data)	0.0617, 0.1401
Largest Diff. Peak and Hole (e Å <sup>-3</sup> )	0.804 and -0.996

$${}^a R_1 = \sum |F_o| - |F_c| / \sum |F_o|. \quad {}^b wR_2 = \{ \sum [w(F_o^2 - F_c^2)^2] / \sum [w(F_o^2)^2] \}^{1/2}.$$

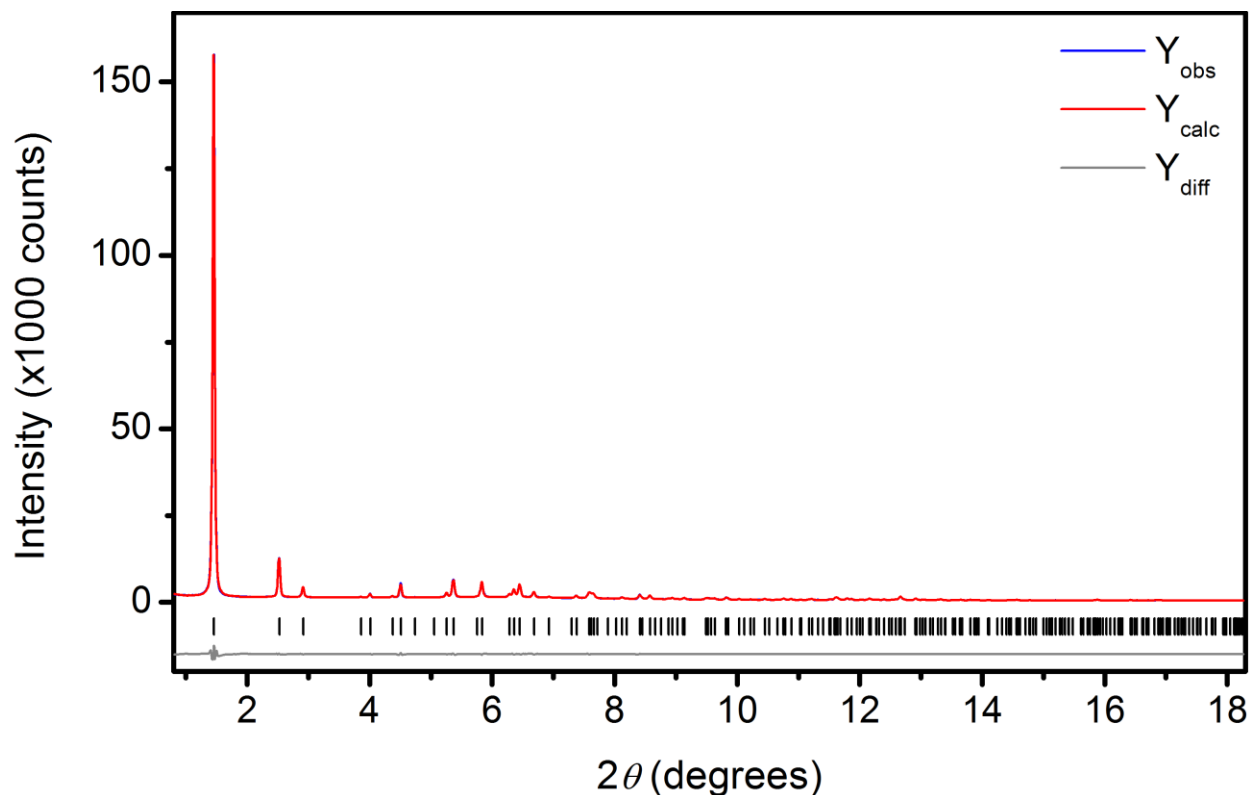


**Figure S24.** Rietveld refinement of CO<sub>2</sub>-inserted (±)-dach-*R*-Mg<sub>2</sub>(dobpdc) at 333 K from 0.8° to 18.3°. Blue and red lines represent the observed and calculated diffraction patterns, respectively. The gray line represents the difference between observed and calculated patterns, and the black tick marks indicate calculated Bragg peak positions. Figures-of-merit (as defined by TOPAS)  $R_{wp} = 4.55\%$ ,  $R_p = 3.08\%$ ,  $R_{bragg} = 1.64\%$ ,  $GoF = 1.83$ . The wavelength was 0.45241 Å.

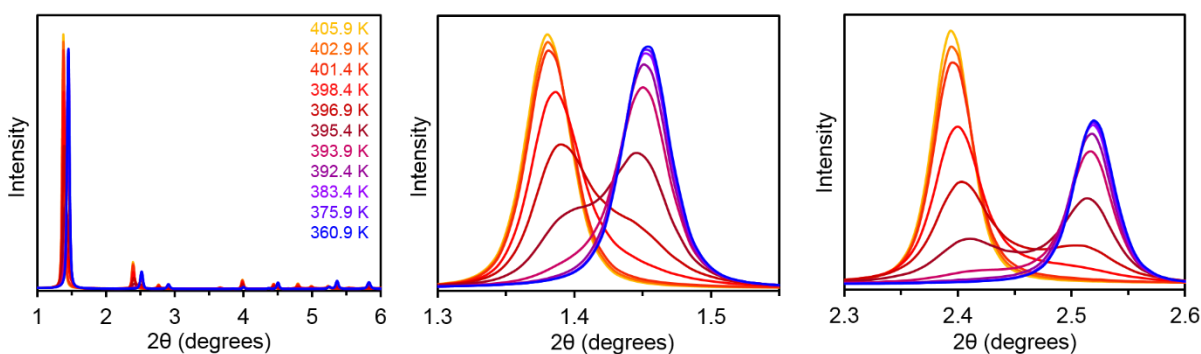


**Figure S25.** Variable temperature synchrotron powder XRD for CO<sub>2</sub>-dosed (±)-dach-(±)-Mg<sub>2</sub>(dobpdc). The sample was activated under vacuum at temperatures up to 453 K (180 °C) for approximately half an hour. Pure CO<sub>2</sub> was dosed on the sample to 0.94 bar, and the sample was cooled at a rate of 1.5 °C/min. Powder patterns were recorded at numerous temperatures. The plots at left, center, and right depict the same data, but with different  $x$ -axis scales. In this experiment, data were collected continuously from 453 K–361 K, and a selection of powder patterns between 405.9 K and 360.9 K are shown. Between 453 K–405.9 K, the diffraction pattern did not change. The data also did not change below 360.9 K.

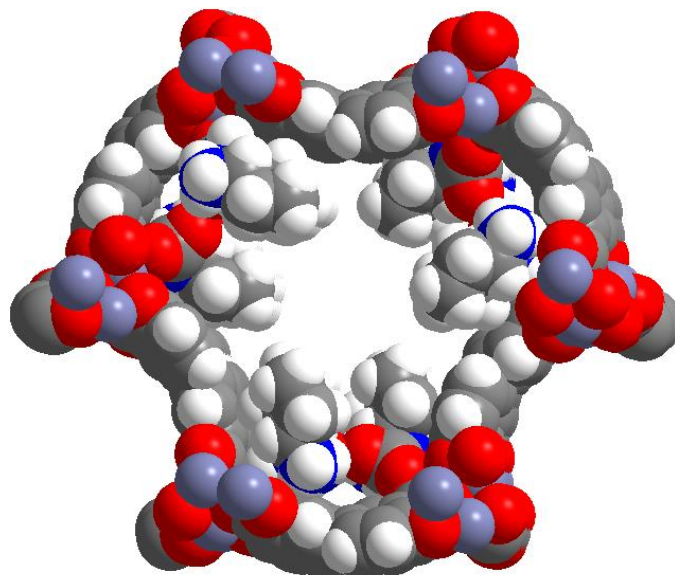


**Figure S26.** Space-filling model of CO<sub>2</sub>-inserted (*S,S*)-dach-Zn<sub>2</sub>(dobpdc); pale purple, red, blue, gray, and white spheres represent Zn, O, N, C, and H atoms, respectively. The left-handed framework is depicted (corresponding to the space group  $P3_221$ ), although the single crystal was an inversion twin containing both left-handed and right-handed subdomains (corresponding to the space groups  $P3_221$  and  $P3_121$ , respectively). Purple, blue, gray, red, and white spheres represent Zn, N, C, O, and H atoms, respectively. The polar ammonium carbamates appeared completely shielded from the pore interior by the cyclohexane rings and the contracted pore walls, suggesting a hydrophobic pore interior. Consistent with this observation, dach-appended variants of Mg<sub>2</sub>(dobpdc) co-adsorbed minimal water in humid CO<sub>2</sub> isobars (Figure S27).

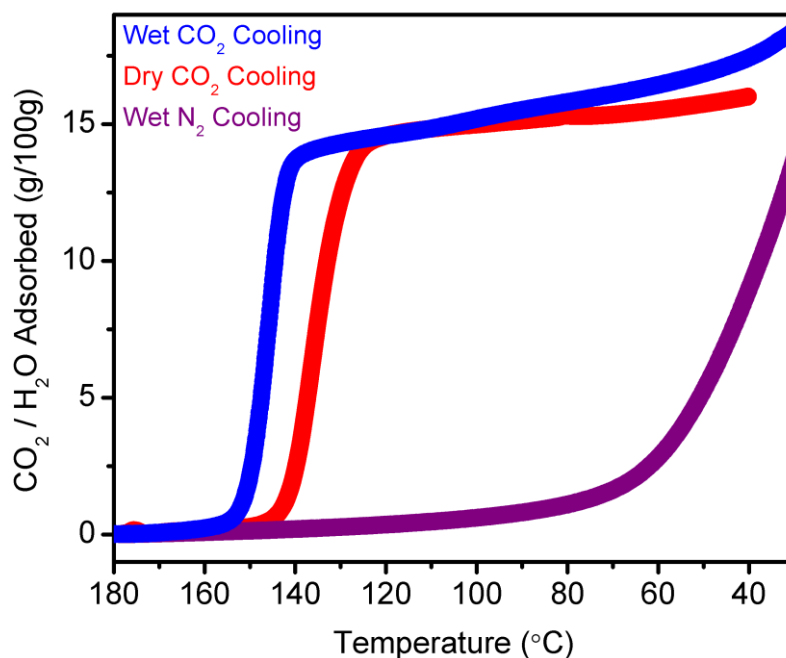


**Figure S27.** Thermogravimetric adsorption (cooling) isobars for ( $\pm$ )-dach-Mg<sub>2</sub>(dobpdc) under humid CO<sub>2</sub> (blue), dry CO<sub>2</sub> (red), or wet N<sub>2</sub> (purple). Temperature ramp rates of 2 °C/min were used. The humid CO<sub>2</sub> stream was obtained by flowing CO<sub>2</sub> through two water bubblers before the gas stream reached the sample in the furnace. The mass discrepancy between the humid and dry CO<sub>2</sub> isobars at 40 °C is only ~1.5 g/100 g, indicating an unusually small amount of water co-adsorption compared to other diamine-appended variants of this material.<sup>3</sup>

## 5. Testing additives for chiral induction of Mg<sub>2</sub>(dobpdc)

**Procedure for small-scale synthesis of Mg<sub>2</sub>(dobpdc) in the presence of chiral additives.** A 20 mL scintillation vial was charged with the ligand H<sub>4</sub>dobpdc (27.4 mg, 0.10 mmol, 1.00 equiv.), Mg(NO<sub>3</sub>)<sub>2</sub>·6H<sub>2</sub>O (64.0 mg, 0.25 mmol, 2.50 equiv.), and the chiral additive of interest (0.30 mmol, a 3:1 molar ratio of chiral additive:H<sub>4</sub>dobpdc). Methanol (5.5 mL) and *N,N*-dimethylformamide (DMF) (4.5 mL) were added, and the solution was sonicated until all of the solids dissolved. The threads of the glass vial were wrapped in Teflon tape, the vial was tightly sealed with a Teflon-lined cap, and the solution was heated at 120 °C in a heating block for 20 h (these reaction solutions were not stirred), during which time a white solid precipitated from solution. The vial was cooled to room temperature and filtered, and the resulting solid was washed thoroughly with fresh DMF (15 mL). The solid was transferred to a vial filled with fresh DMF (10 mL) and allowed to soak at 120 °C for 24 h. The supernatant was decanted and replaced with fresh DMF (10 mL). This process was repeated a total of three times. The DMF was replaced with methanol (10 mL), and the off-white solid was soaked in methanol at 60 °C for 3 h. The supernatant was decanted and replaced with fresh methanol (10 mL). This process was repeated a total of three times.

**Procedure for gram-scale synthesis of *R*-Mg<sub>2</sub>(dobpdc) and *S*-Mg<sub>2</sub>(dobpdc) using D-panthenol as chiral additive.** For synthesis of *R*-Mg<sub>2</sub>(dobpdc), a 350 mL glass pressure vessel was charged with the ligand H<sub>4</sub>dobpdc (0.879 g, 3.2 mmol, 1.00 equiv.) and Mg(NO<sub>3</sub>)<sub>2</sub>·6H<sub>2</sub>O (1.11 g, 4.31 mmol, 1.34 equiv.). Separately, DMF (26.4 mL) and D-panthenol (25.61 g, 125 mmol, 39:1 D-panthenol:H<sub>4</sub>dobpdc molar ratio) were mixed in a glass jar, and the mixture was heated with a heat gun and gently agitated until all of the D-panthenol had dissolved. Methanol (36.9 mL) was added to the DMF/D-panthenol mixture and gently agitated to make the solution homogeneous. Finally, the DMF/methanol/D-panthenol solvent system was added, along with a 3 cm, Teflon-coated magnetic stirring bar, to the 350 mL glass pressure vessel containing H<sub>4</sub>dobpdc and Mg(NO<sub>3</sub>)<sub>2</sub>·6H<sub>2</sub>O. The reactor was sealed with a Teflon cap equipped with an O-ring and heated in a silicone oil bath at 120 °C for 20 h with vigorous stirring (at least 750 min<sup>-1</sup> stirring rate). The white powder was isolated by filtration and soaked three times in 200 mL of DMF for a minimum of 3 h at 60 °C followed by solvent exchange by soaking three times in 200 mL of methanol for a minimum of 3 h at 60 °C. For synthesis of *S*-Mg<sub>2</sub>(dobpdc), the procedure was identical to that described above for *R*-Mg<sub>2</sub>(dobpdc), except that 3.97 g of H<sub>4</sub>dobpdc (14.5 mmol, 1.00 equiv.), 4.86 g Mg(NO<sub>3</sub>)<sub>2</sub>·6H<sub>2</sub>O (19.0 mmol, 1.32 equiv.), 31.86 g D-panthenol, 28 mL methanol, and 20 mL DMF were used.

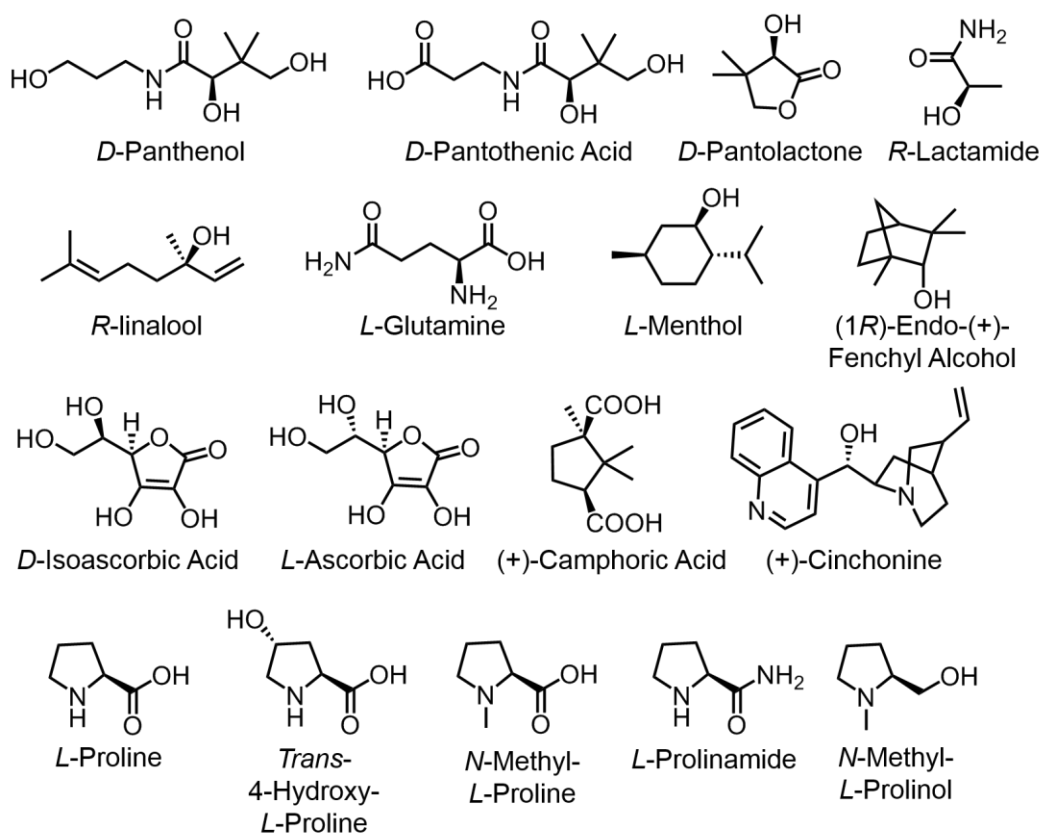


**Figure S28.** Structures of chiral additives tested in the synthesis of enantiopure Mg<sub>2</sub>(dobpdc).

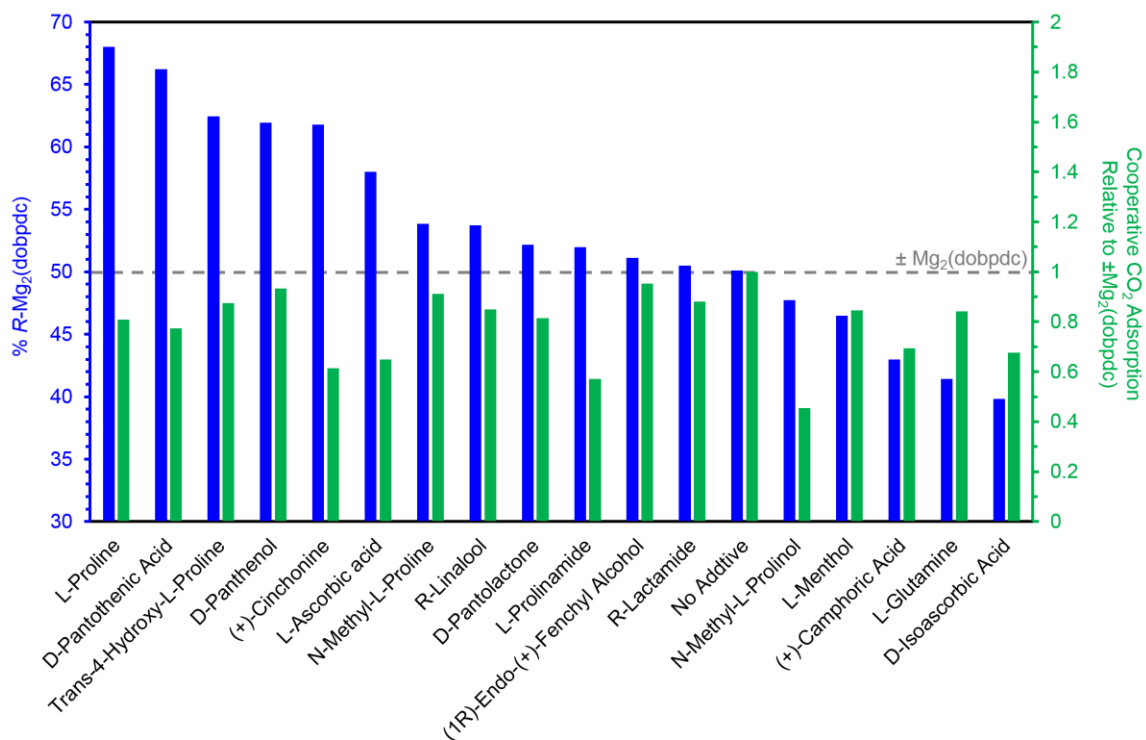


**Figure S29.** Quantitation of chiral induction of Mg<sub>2</sub>(dobpdc) by the various additives. The enantiopurity of Mg<sub>2</sub>(dobpdc) was determined by grafting (*R,R*)-dach, characterizing CO<sub>2</sub> adsorption by TGA, and quantifying the ratio CO<sub>2</sub> captured during the high-temperature step over CO<sub>2</sub> captured during the low-temperature step. In addition, the total amount of CO<sub>2</sub> captured within the steps, or cooperative CO<sub>2</sub> adsorption, was quantified to probe sample quality (right-hand axis). In contrast, some additives yielded broad CO<sub>2</sub> adsorption steps and caused substantial reductions in CO<sub>2</sub> capacity (Figure S36). In some cases, low CO<sub>2</sub> capacities clearly correlated with poor crystallinity by PXRD. It is possible that higher-quality samples could be obtained with further optimization for these additives, but in this study, only L-proline and D-panthenol were explored further.

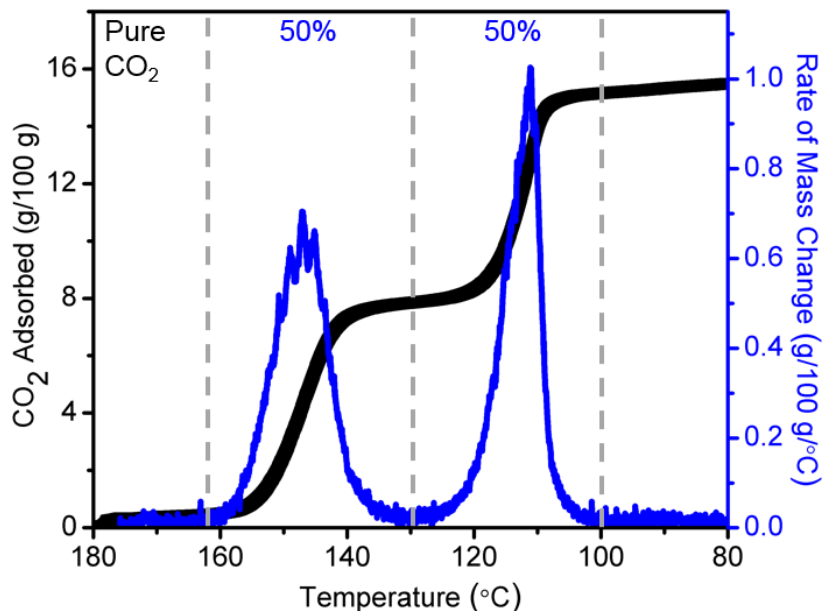


**Figure S30.** Thermogravimetric adsorption (cooling) isobar (black) and derivative trace (blue) for (*R,R*)-dach-Mg<sub>2</sub>(dobpdc). A temperature ramp rate of 2 °C/min was used. The step heights were quantified by measuring the CO<sub>2</sub> uptake occurring between the gray vertical lines, which represent the boundaries chosen for defining the high- and low-temperature steps. This racemic sample of Mg<sub>2</sub>(dobpdc) exhibits a 50:50 ratio between the two step heights.

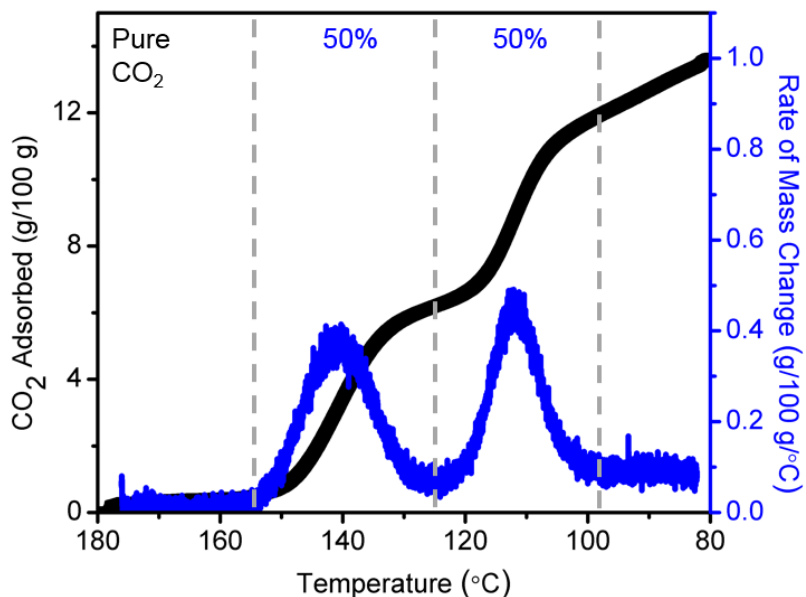


**Figure S31.** Thermogravimetric adsorption (cooling) isobar (black) and derivative trace (blue) for (*R,R*)-dach-Mg<sub>2</sub>(dobpdc), synthesized in the absence of chiral additives with dilute reagent concentrations and without stirring, matched to the reaction conditions of the chiral additive screen. A temperature ramp rate



of 2 °C/min was used. The step heights were quantified by measuring the CO<sub>2</sub> uptake occurring between the gray vertical lines, which represent the boundaries chosen for defining the high- and low-temperature steps. This racemic sample of Mg<sub>2</sub>(dobpdc) exhibits a perfect 50:50 ratio between the two step heights. The two steps are slightly less sharp than those shown in the preceding figure, which we attribute to the lower reactant concentrations that were used for the chiral additive testing.

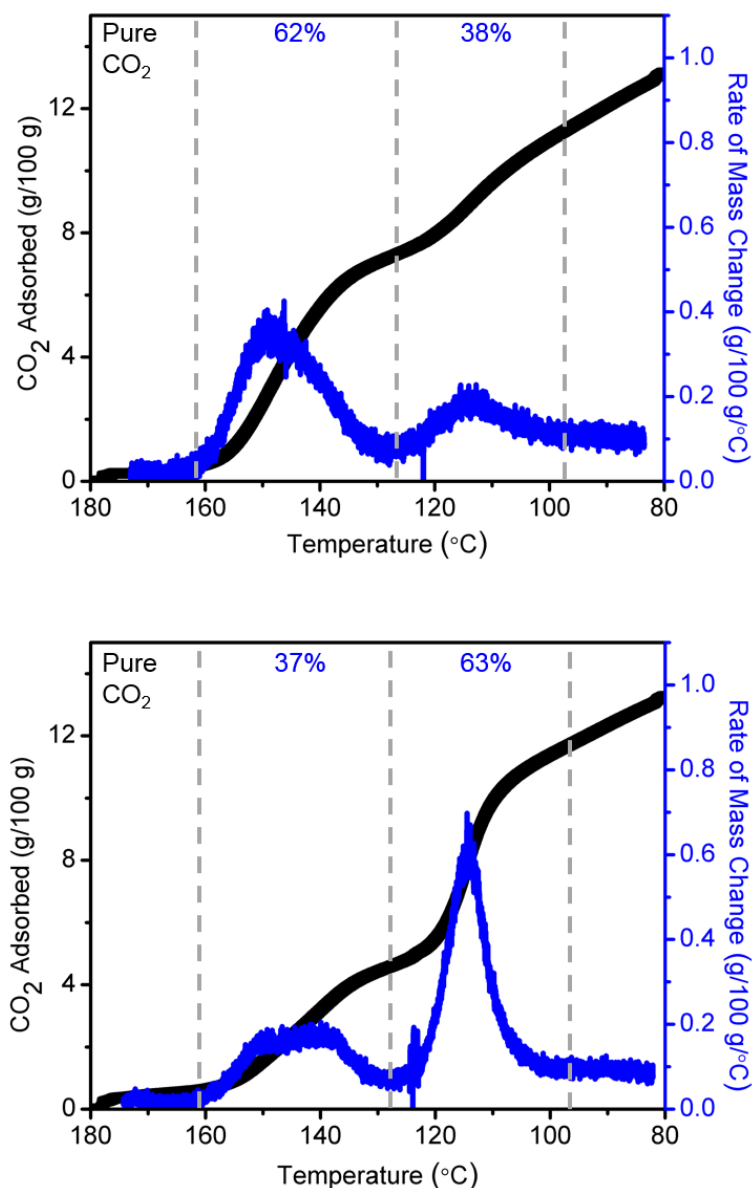


**Figure S32.** Thermogravimetric adsorption (cooling) pure CO<sub>2</sub> isobars (black) and derivative traces (blue) for Mg<sub>2</sub>(dobpdc), synthesized in the presence of three equivalents of D-panthenol in the chiral additive screen, grafted with either (*R,R*)-dach (top plot) or (*S,S*)-dach (bottom plot). A temperature ramp rate of 2 °C/min was used. The step heights were quantified by measuring the CO<sub>2</sub> uptake occurring between the gray vertical lines, which represent the boundaries chosen for defining the high- and low-temperature steps. These plots indicate that this sample of Mg<sub>2</sub>(dobpdc) contains ~62% *R*-Mg<sub>2</sub>(dobpdc) and ~38% *S*-Mg<sub>2</sub>(dobpdc).

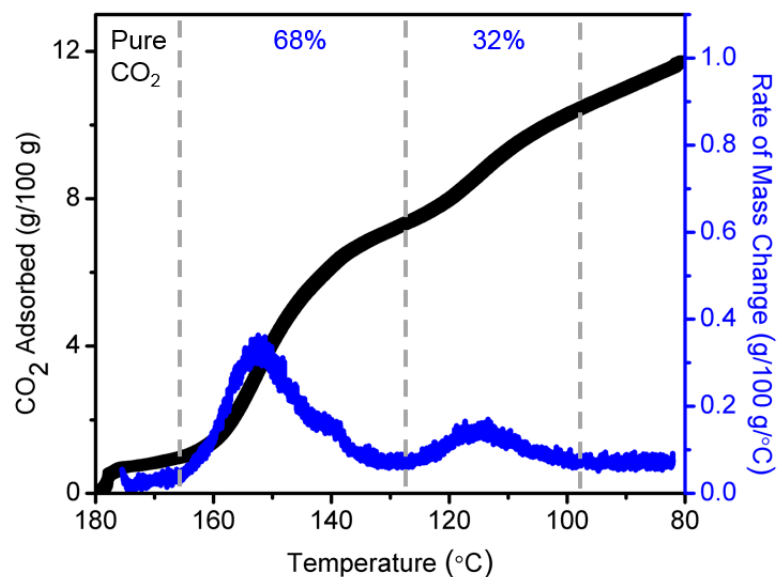


**Figure S33.** Thermogravimetric adsorption (cooling) pure CO<sub>2</sub> isobar (black) and derivative trace (blue) for Mg<sub>2</sub>(dobpdc), synthesized in the presence of three equivalents of L-proline in the chiral additive screen, grafted with (*R,R*)-dach. A temperature ramp rate of 2 °C/min was used. The step heights were quantified by measuring the CO<sub>2</sub> uptake occurring between the gray vertical lines, which represent the boundaries chosen for defining the high- and low-temperature steps. These plots indicate that this sample of Mg<sub>2</sub>(dobpdc) contains ~68% *R*-Mg<sub>2</sub>(dobpdc) and ~32% *S*-Mg<sub>2</sub>(dobpdc).

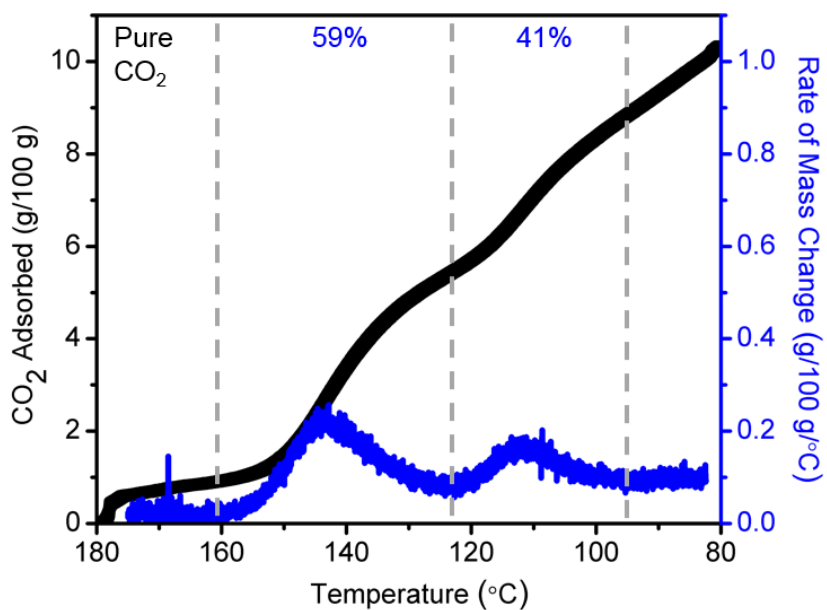


**Figure S34.** Thermogravimetric adsorption (cooling) pure CO<sub>2</sub> isobar (black) and derivative trace (blue) for Mg<sub>2</sub>(dobpdc), synthesized in the presence of three equivalents of L-ascorbic acid in the chiral additive screen, grafted with (*R,R*)-dach. A temperature ramp rate of 2 °C/min was used. The step heights were

quantified by measuring the CO<sub>2</sub> uptake occurring between the gray vertical lines, which represent the boundaries chosen for defining the high- and low-temperature steps. These plots indicate that this sample of Mg<sub>2</sub>(dobpdc) contains ~59% *R*-Mg<sub>2</sub>(dobpdc) and ~41% *S*-Mg<sub>2</sub>(dobpdc).

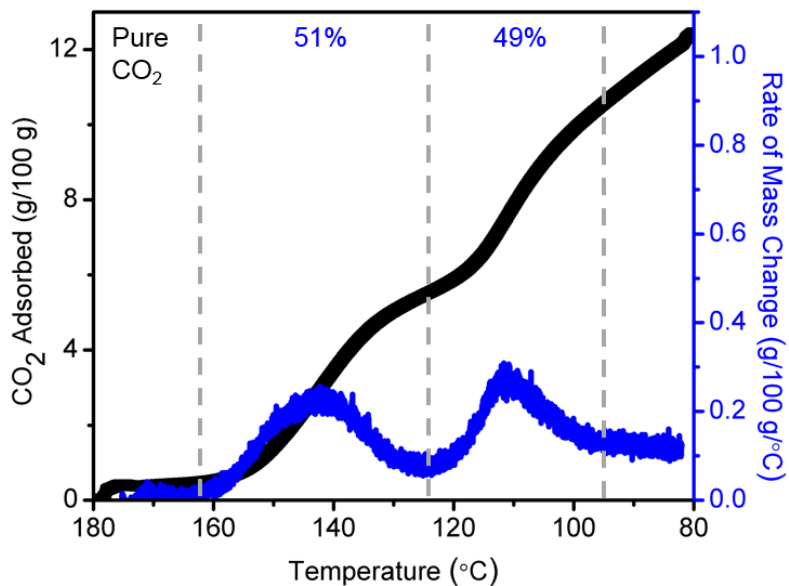


**Figure S35.** Thermogravimetric adsorption (cooling) pure CO<sub>2</sub> isobar (black) and derivative trace (blue) for Mg<sub>2</sub>(dobpdc), synthesized in the presence of three equivalents of *R*-lactamide in the chiral additive screen, grafted with (*R,R*)-dach. A temperature ramp rate of 2 °C/min was used. The step heights were quantified by measuring the CO<sub>2</sub> uptake occurring between the gray vertical lines, which represent the boundaries chosen for defining the high- and low-temperature steps. These plots indicate that this sample of Mg<sub>2</sub>(dobpdc) contains ~51% *R*-Mg<sub>2</sub>(dobpdc) and ~49% *S*-Mg<sub>2</sub>(dobpdc).

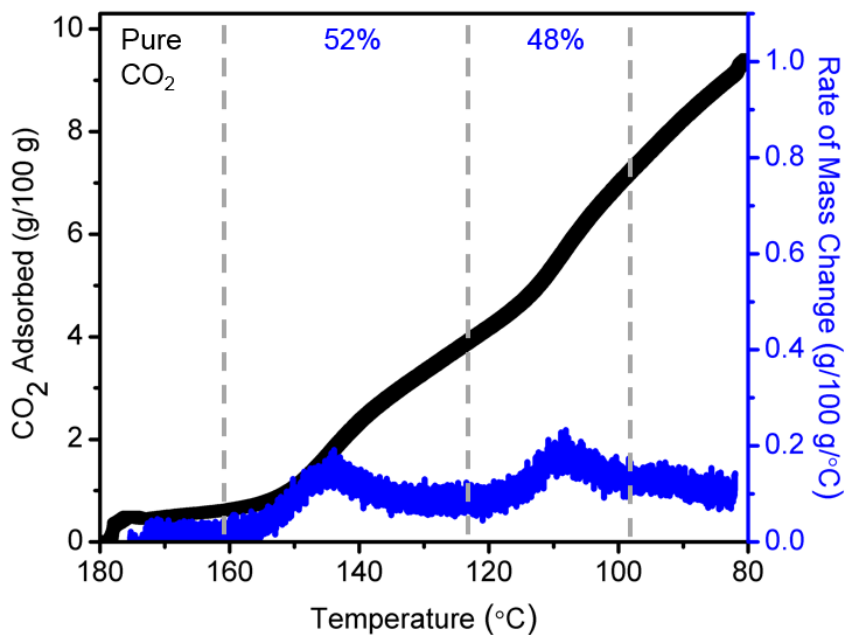


**Figure S36.** Thermogravimetric adsorption (cooling) pure CO<sub>2</sub> isobar (black) and derivative trace (blue) for Mg<sub>2</sub>(dobpdc), synthesized in the presence of three equivalents of L-prolinamide in the chiral additive screen, grafted with (*R,R*)-dach. A temperature ramp rate of 2 °C/min was used. The step heights were quantified by measuring the CO<sub>2</sub> uptake occurring between the gray vertical lines, which represent the boundaries chosen for defining the high- and low-temperature steps. These plots indicate that this sample of Mg<sub>2</sub>(dobpdc) contains ~52% *R*-Mg<sub>2</sub>(dobpdc) and ~48% *S*-Mg<sub>2</sub>(dobpdc). The broad adsorption steps and the low CO<sub>2</sub> capacity are indicative of suboptimal crystallinity and/or porosity.

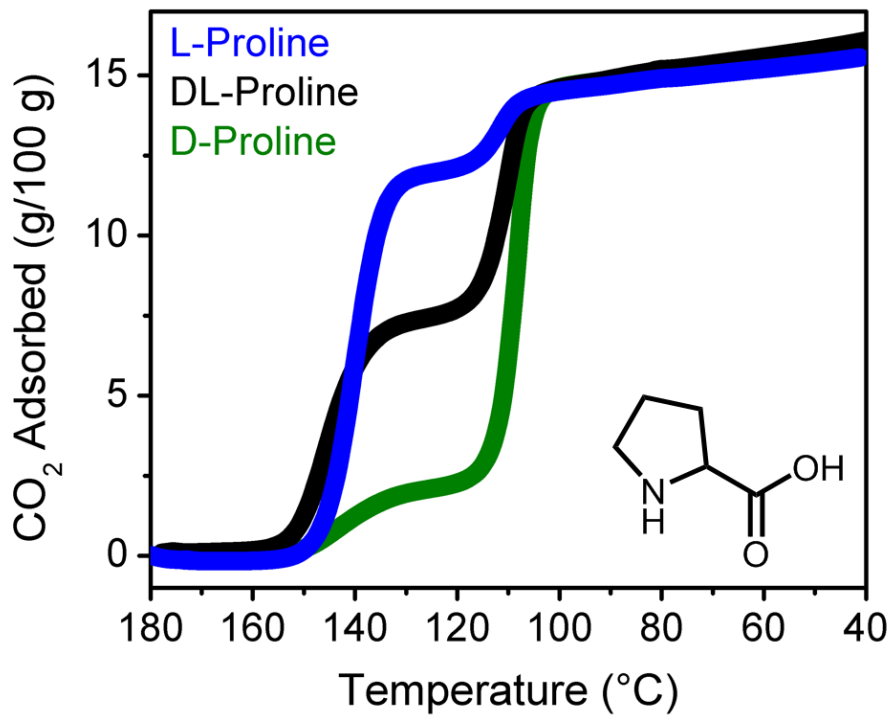


**Figure S37.** Thermogravimetric adsorption (cooling) pure CO<sub>2</sub> isobars for Mg<sub>2</sub>(dobpdc), synthesized in the presence of L-proline (blue), DL-proline (black), or D-proline (green), grafted with (R,R)-dach. In each reaction, 5 molar equivalents of proline were added relative to H<sub>4</sub>dobpdc. The samples synthesized in the presence of L- and D-proline are enantiomers of each other and are each approximately 90% enantiopure. The chemical structure of proline is shown at bottom right.

## 6. Characterization of *R*- and *S*-Mg<sub>2</sub>(dobpdc)

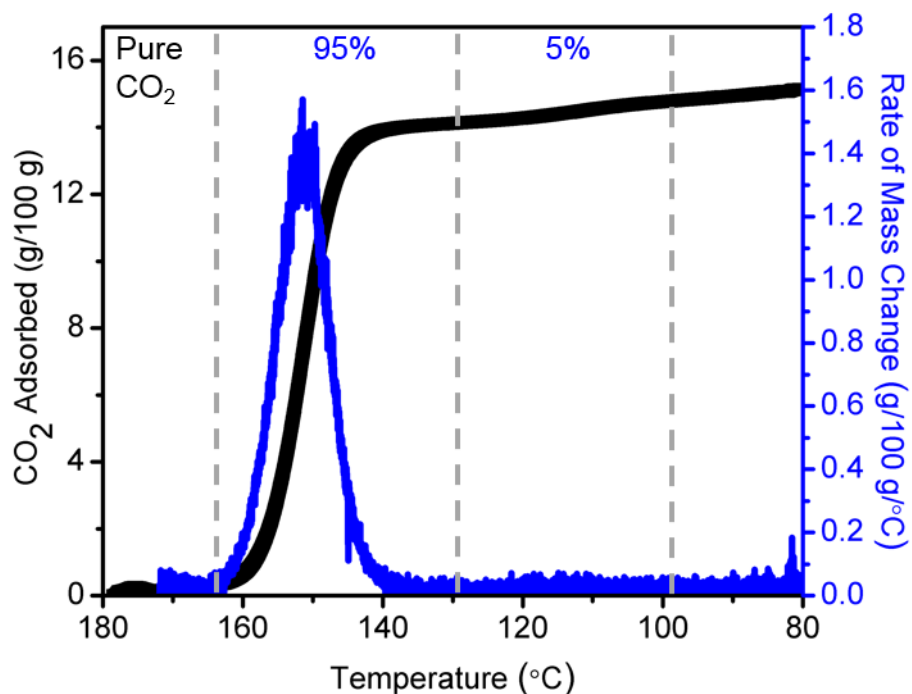


**Figure S38.** Thermogravimetric adsorption (cooling) pure CO<sub>2</sub> isobars (black) and derivative traces (blue) for (*R,R*)-dach-*R*-Mg<sub>2</sub>(dobpdc). The CO<sub>2</sub> adsorption isobar is the same as that presented in Figure 5b, corresponding to an H<sub>4</sub>dobpdc concentration of 37 mM. A temperature ramp rate of 2 °C/min was used. The step heights were quantified by measuring the CO<sub>2</sub> uptake occurring between the gray vertical lines, which represent the boundaries chosen for defining the high- and low-temperature steps. The plots indicate that this sample of Mg<sub>2</sub>(dobpdc) contains 95% *R*-Mg<sub>2</sub>(dobpdc) and ~5% *S*-Mg<sub>2</sub>(dobpdc). A short and broad peak is visible in the derivative plot ~115 °C, indicating the presence of *S*-Mg<sub>2</sub>(dobpdc).

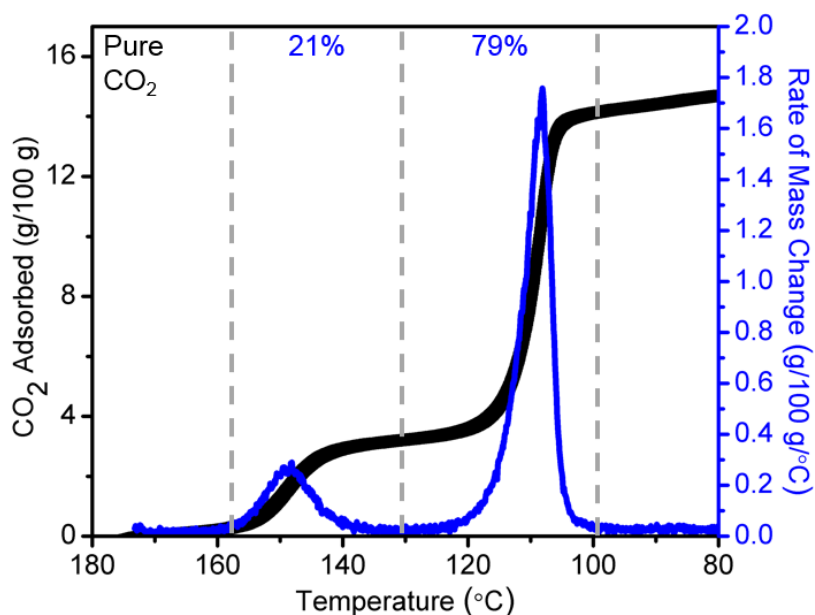


**Figure S39.** Thermogravimetric adsorption (cooling) pure CO<sub>2</sub> isobars (black) and derivative traces (blue) for Mg<sub>2</sub>(dobpdc), synthesized in a solvent system containing 40% D-panthenol, grafted with (*S,S*)-dach. This isobar corresponds to the result presented in Figure 7 corresponding to an H<sub>4</sub>dobpdc concentration of 91 mM. A temperature ramp rate of 2 °C/min was used. The step heights were quantified by measuring the CO<sub>2</sub> uptake occurring between the gray vertical lines, which represent the boundaries chosen for defining the high- and low-temperature steps. These plots indicate that this sample of Mg<sub>2</sub>(dobpdc) contains ~79% *R*-Mg<sub>2</sub>(dobpdc) and ~21% *S*-Mg<sub>2</sub>(dobpdc).

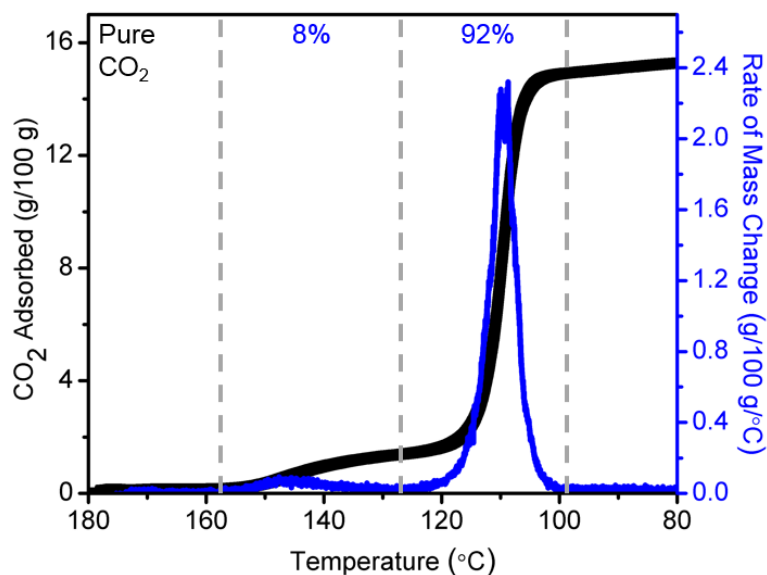


**Figure S40.** Thermogravimetric adsorption (cooling) pure CO<sub>2</sub> isobars (black) and derivative traces (blue) for (*R,R*)-dach-*S*-Mg<sub>2</sub>(dobpdc). The CO<sub>2</sub> adsorption isobar is the same as that presented in Figure 5c, corresponding to a H<sub>4</sub>dobpdc concentration of 181 mM. A temperature ramp rate of 2 °C/min was used. The step heights were quantified by measuring the CO<sub>2</sub> uptake occurring between the gray vertical lines, which represent the boundaries chosen for defining the high- and low-temperature steps. These plots indicate that this sample of Mg<sub>2</sub>(dobpdc) contains ~8% *R*-Mg<sub>2</sub>(dobpdc) and ~92% *S*-Mg<sub>2</sub>(dobpdc).

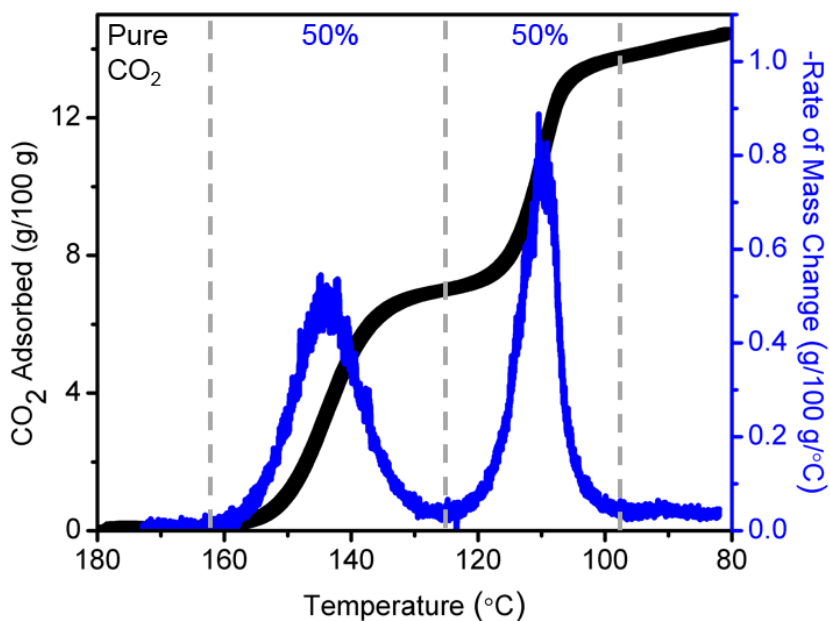


**Figure S41.** Thermogravimetric adsorption (cooling) pure CO<sub>2</sub> isobar (black) and derivative trace (blue) for Mg<sub>2</sub>(dobpdc), synthesized in the presence of DL-panthenol, grafted with (*R,R*)-dach. This sample of



$\text{Mg}_2(\text{dobpdc})$  was synthesized using the exact same reaction conditions as the sample depicted in Figure S38, except that DL-panthenol was used in place of D-panthenol. A temperature ramp rate of  $2\text{ }^\circ\text{C}/\text{min}$  was used. The step heights were quantified by measuring the  $\text{CO}_2$  uptake occurring between the gray vertical lines, which represent the boundaries chosen for defining the high- and low-temperature steps. These plots indicate that this sample of  $\text{Mg}_2(\text{dobpdc})$  contains  $\sim 50\%$   $R\text{-Mg}_2(\text{dobpdc})$  and  $\sim 50\%$   $S\text{-Mg}_2(\text{dobpdc})$ .

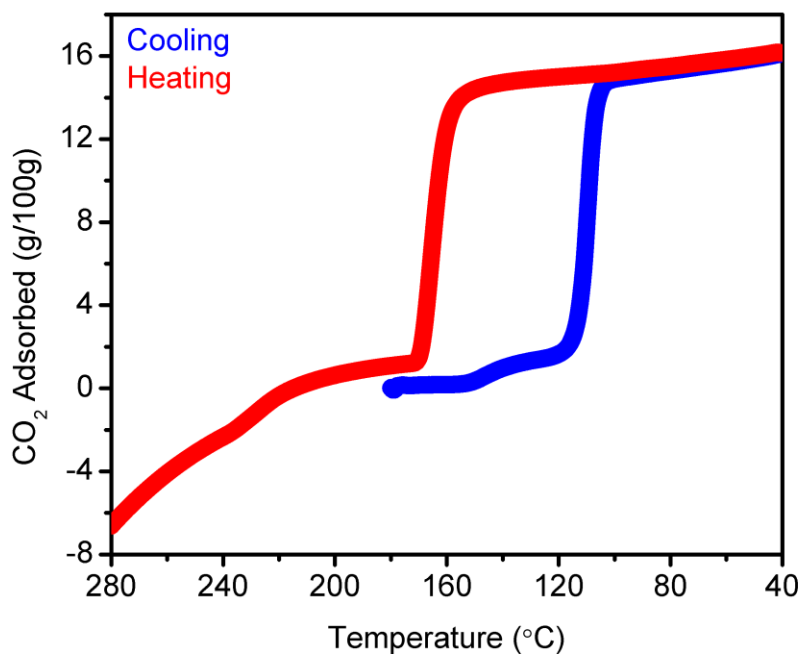


**Figure S42.** Thermogravimetric adsorption (cooling) and heating (red) pure  $\text{CO}_2$  isobars for  $(R,R)\text{-dach-S-Mg}_2(\text{dobpdc})$ . The  $\text{CO}_2$  adsorption isobar is the same as that presented in Figure 6c, corresponding to an  $\text{H}_4\text{dobpdc}$  concentration of 181 mM. A temperature ramp rate of  $2\text{ }^\circ\text{C}/\text{min}$  was used. The mass loss upon heating above  $240\text{ }^\circ\text{C}$  can be attributed to diamine volatilization.

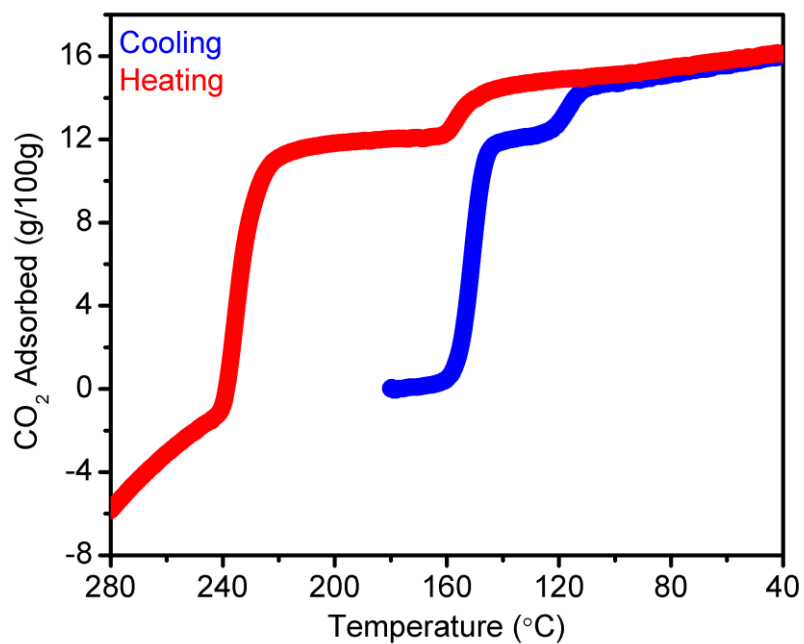


**Figure S43.** Thermogravimetric adsorption (cooling) and heating (red) pure CO<sub>2</sub> isobars for Mg<sub>2</sub>(dobpdc), synthesized in the presence of 40% D-panthenol, grafted with (*R,R*)-dach. The CO<sub>2</sub> adsorption isobar is the same as that presented in Figure 7, corresponding to an H<sub>4</sub>dobpdc concentration of 91 mM. A temperature ramp rate of 2 °C/min was used. The mass loss upon heating above 240 °C can be attributed to diamine volatilization.

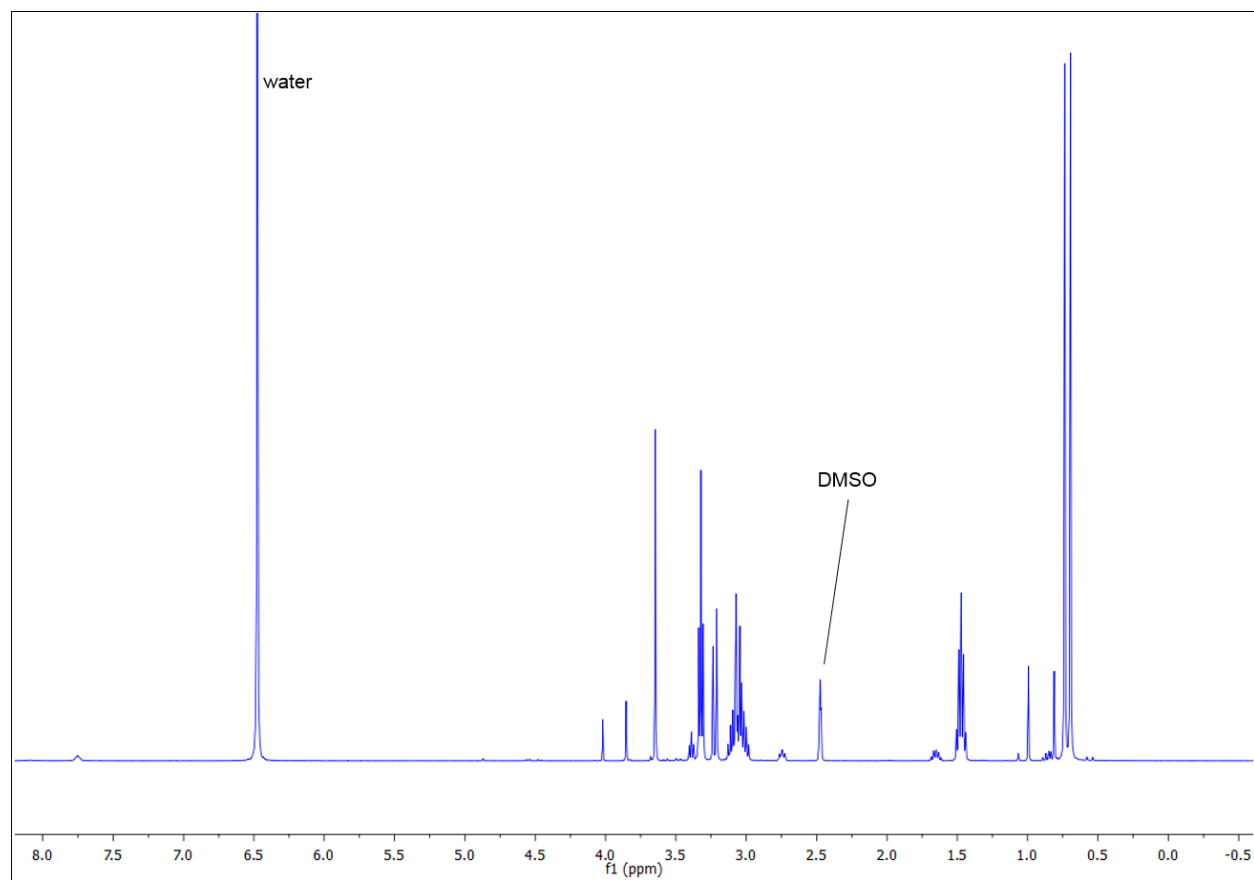


**Figure S44.** <sup>1</sup>H NMR spectrum of D-panthenol (DMSO-*d*<sub>6</sub>). D-panthenol was dissolved in DMSO-*d*<sub>6</sub> with DCl and heated at 60 °C, to match the conditions of acid digest for Mg<sub>2</sub>(dobpdc). This spectrum was recorded on a Bruker AVQ-400 instrument.

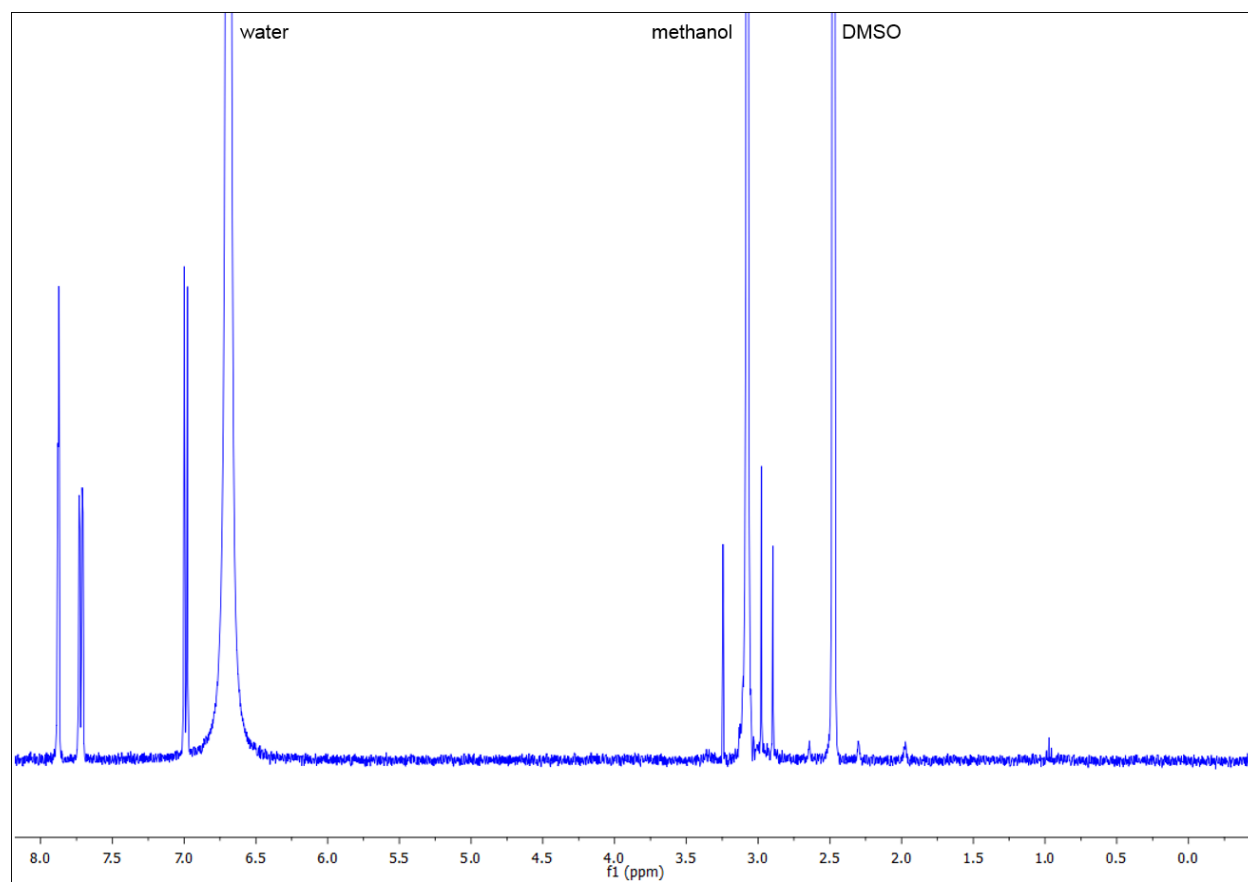


**Figure S45.** <sup>1</sup>H NMR spectrum of acid-digested methanol-solvated *R*-Mg<sub>2</sub>(dobpdc) (DMSO-*d*<sub>6</sub>). This material was synthesized in the presence of D-panthenol, then washed extensively with DMF followed by methanol. No D-panthenol is detectable in the spectrum. This spectrum was recorded on a Bruker AVQ-400 instrument.

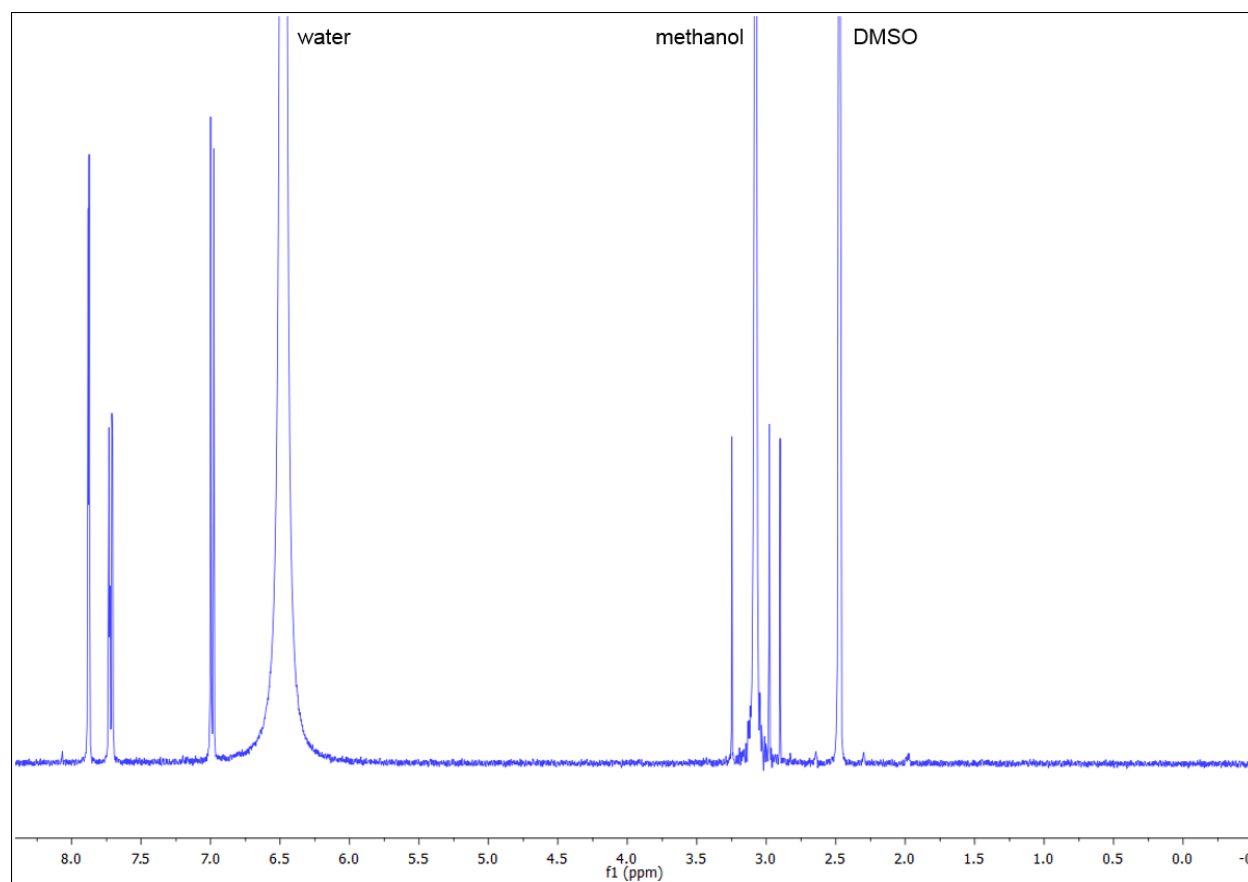


**Figure S46.**  $^1\text{H}$  NMR spectrum of acid-digested methanol-solvated  $S\text{-Mg}_2(\text{dobpdc})$  ( $\text{DMSO-}d_6$ ). This material was synthesized in the presence of D-panthenol, then washed extensively with DMF followed by methanol. No D-panthenol is detectable in the spectrum. This spectrum was recorded on a Bruker AVQ-400 instrument.

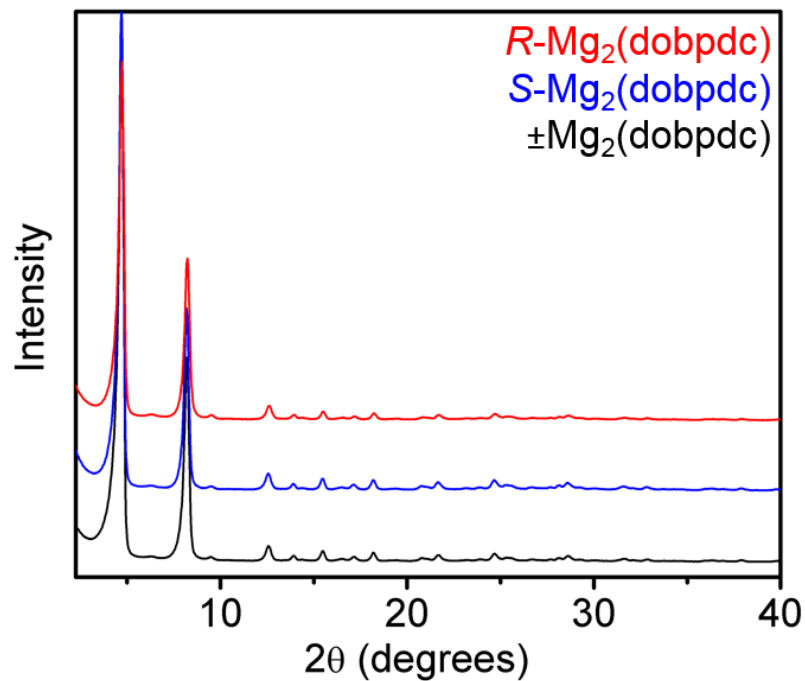


**Figure S47.** Powder X-ray diffraction patterns for *R*-, *S*-, and ( $\pm$ )- $\text{Mg}_2(\text{dobpdc})$ .

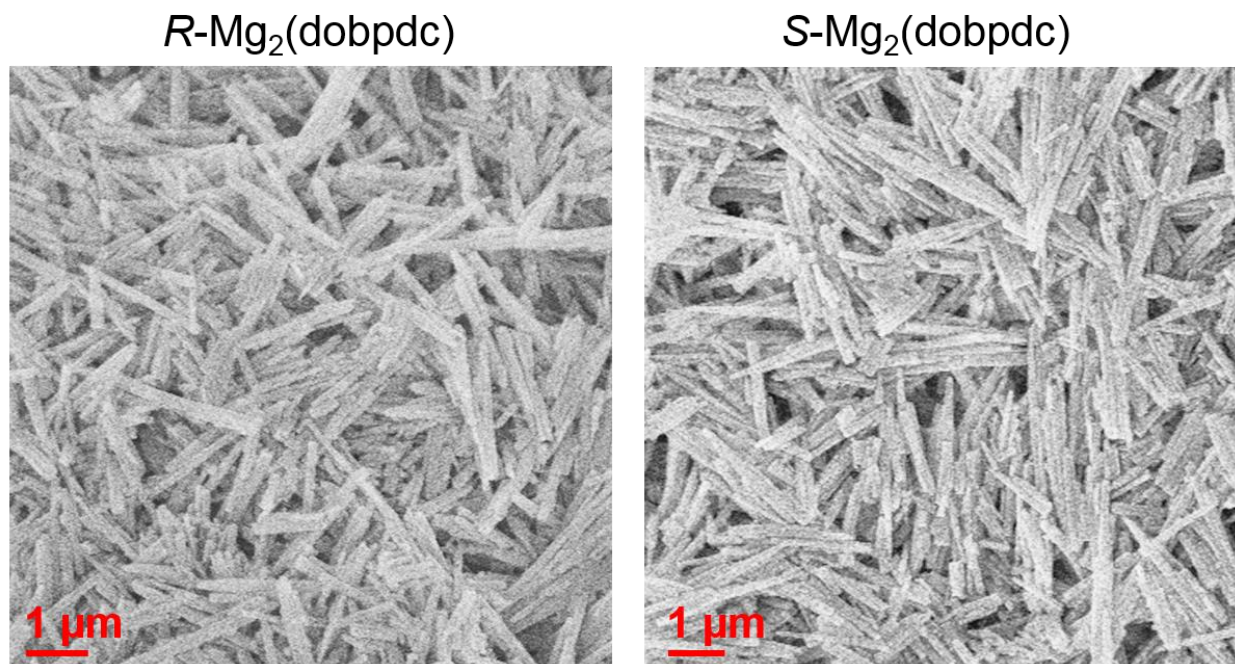


**Figure S48.** Scanning electron microscopy images of *R*- and *S*- $\text{Mg}_2(\text{dobpdc})$  crystallites.

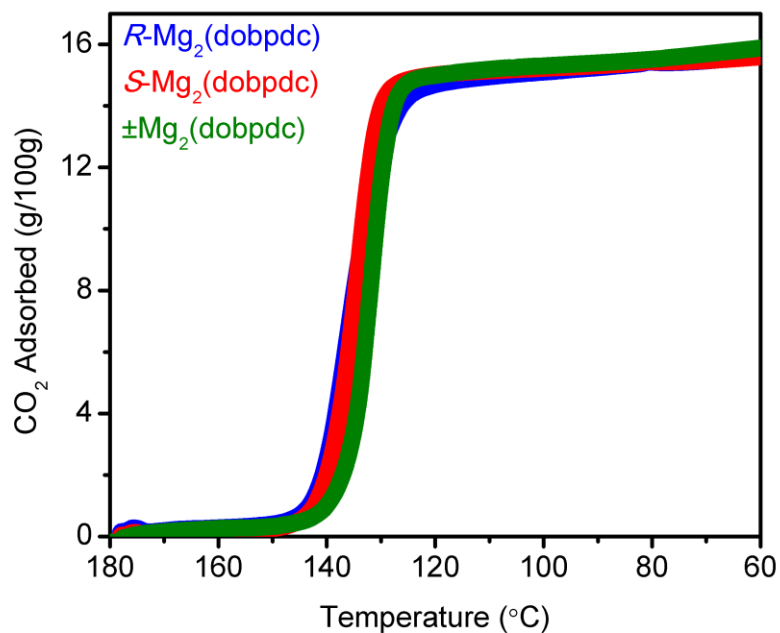


**Figure S49.** Thermogravimetric adsorption (cooling) isobars under pure CO<sub>2</sub> for (±)-dach appended to *R*-Mg<sub>2</sub>(dobpdc) (blue), *S*-Mg<sub>2</sub>(dobpdc) (red), (±)-Mg<sub>2</sub>(dobpdc) (green). A temperature ramp rate of 2 °C/min was used.

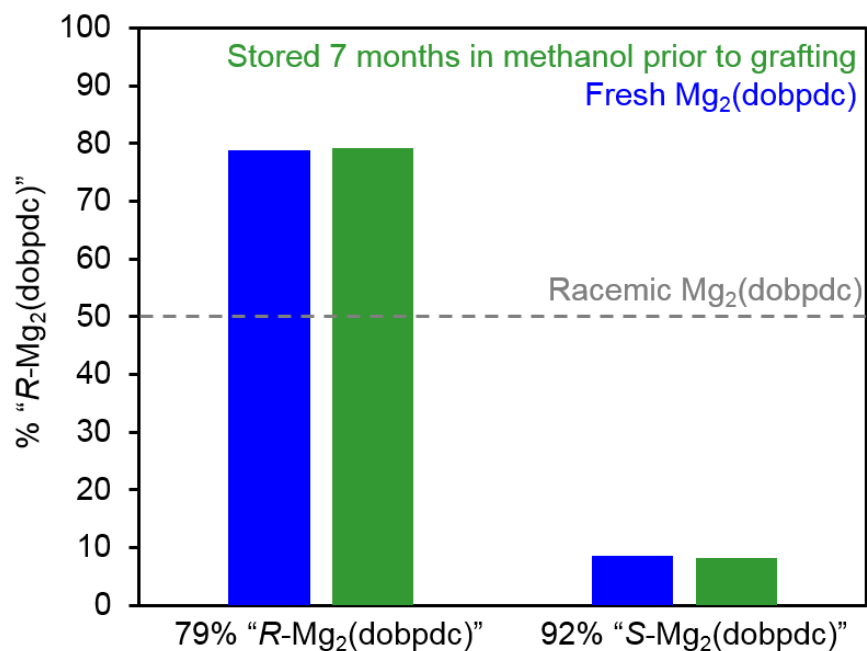


**Figure S50.** Enantiopurity of Mg<sub>2</sub>(dobpdc) samples as-synthesized (blue, “Fresh”) and after 7 months of storage in methanol (green), as determined by grafting of enantiopure dach, characterization of CO<sub>2</sub> adsorption, and quantification of relative step heights. The horizontal gray dotted line indicates the enantiopurity expected for (±)-Mg<sub>2</sub>(dobpdc).

## 7. Solid-state circular dichroism and calculated CD spectra

**Procedure for experimental solid-state circular dichroism (CD).** All solid-state CD measurements were performed on a J-1500 CD spectrometer (JASCO Corporation) at 298 K. Approximately 50 mg of methanol-solvated *R*-Mg<sub>2</sub>(dobpdc), *S*-Mg<sub>2</sub>(dobpdc), or (±)-Mg<sub>2</sub>(dobpdc) were rinsed with 10 mL deionized water, then stored in a sealed vial for under air 10 d. Immediately prior to CD measurements, the samples were placed on weighing paper and allowed to dry under air.

For the KBr transmission measurements, approximately 0.5 mg of dry sample was mixed with 100 mg of KBr in a mortar. The resulting powder was formed into a tablet with 5 mm diameter prior to measurement. A photomultiplier tube (PMT) detector was used. A scan speed of 200 nm/min was used, with a data interval of 0.1 nm and a bandwidth of 2 nm. Transmission linear dichroism and high tension voltage measurements were performed on the same pellets on the same CD spectrometer. The sample tablet was rotated after each measurement and totally measured at four different angles (0, 45, 90, and 135 degrees) to confirm that linear dichroism (LD) did not cause any interference for the CD spectra.

For the diffuse reflectance measurements, approximately 10 mg of sample was dried in a mortar, followed by grinding into a fine powder, which was directly introduced into a diffuse reflectance circular dichroism sample holder. A PMT detector was used. The scan speed was 200 nm/min with a data interval of 0.1 nm and a bandwidth of 16 nm. Diffuse reflectance linear dichroism and high tension voltage measurements were performed on the same samples on the same sample holder and CD spectrometer.

**Procedure for calculated CD spectra.** To support the experimental assignment of the absolute configuration of the M<sub>2</sub>(dobpdc) materials, calculations with Kohn-Sham (KS) density functional theory (KST, or DFT) and its time-dependent variant (TDKS, or TDDFT)<sup>12</sup> were performed for various structural motifs that were extracted from the left-handed (*S*) crystal structure of DMA-solvated Zn<sub>2</sub>(dobpdc). The molecular cluster models studied here are shown in Figure S54 and are representative of the diversity of local structural motifs in the materials. The models are (i) a set of one, two, or three stacked twisted dobpc<sup>4-</sup> molecules coordinated to two, four, or six Zn<sup>2+</sup> cations, respectively, [Zn<sub>2</sub>(dobpdc)], [Zn<sub>2</sub>(dobpdc)]<sub>2</sub>, and [Zn<sub>2</sub>(dobpdc)]<sub>3</sub>, that correspond to the organic linkers dobpc<sup>4-</sup> from which the M<sub>2</sub>(dobpdc) frameworks are assembled, (ii) a segment of the metal-oxo helix consisting of seven truncated dobpc<sup>4-</sup> molecules (with one phenyl ring included), [Zn(opc)]<sub>7</sub>, that is present in the corners of the M<sub>2</sub>(dobpdc) channels, and (iii) a more extended fragment of M<sub>2</sub>(dobpdc) channels including a segment of the metal-oxo helix consisting of seven full dobpc<sup>4-</sup> molecules, [Zn<sub>2</sub>(dobpdc)]<sub>7</sub>. The dangling bonds in [Zn(opc)]<sub>7</sub> were saturated with hydrogen atoms whose positions were optimized with the BP<sup>13,14,15</sup> exchange-correlation functional and a split-valence basis set with one set of polarization functions for non-hydrogen atoms, SV(P),<sup>16,17,18</sup> using the Turbomole package (TM6.6).<sup>19,20,21</sup> The TDDFT linear response CD calculations utilized the global hybrid functional B3LYP<sup>22-24</sup> and two functionals with range-separated exchange in their default parametrization, CAM-B3LYP and LC-PBE0,<sup>25</sup> with the SV(P) basis set. These calculations were carried out with the Gaussian 09 program (G09).<sup>26</sup> The TDDFT calculations reported here cover up to 600 lowest singlet excited states (S<sub>1</sub>-S<sub>200</sub> for [Zn<sub>2</sub>(dobpdc)]), S<sub>1</sub>-S<sub>400</sub> for [Zn<sub>2</sub>(dobpdc)]<sub>2</sub> and [Zn(opc)]<sub>7</sub>, S<sub>1</sub>-S<sub>600</sub> for [Zn<sub>2</sub>(dobpdc)]<sub>3</sub> and [Zn<sub>2</sub>(dobpdc)]<sub>7</sub>). The simulated CD spectra shown are the sums of Gaussian functions centered at the vertical excitation energies and scaled using the calculated rotatory strengths, with a parameter of  $\sigma = 0.15$  eV applied for the root mean square width.<sup>27</sup>



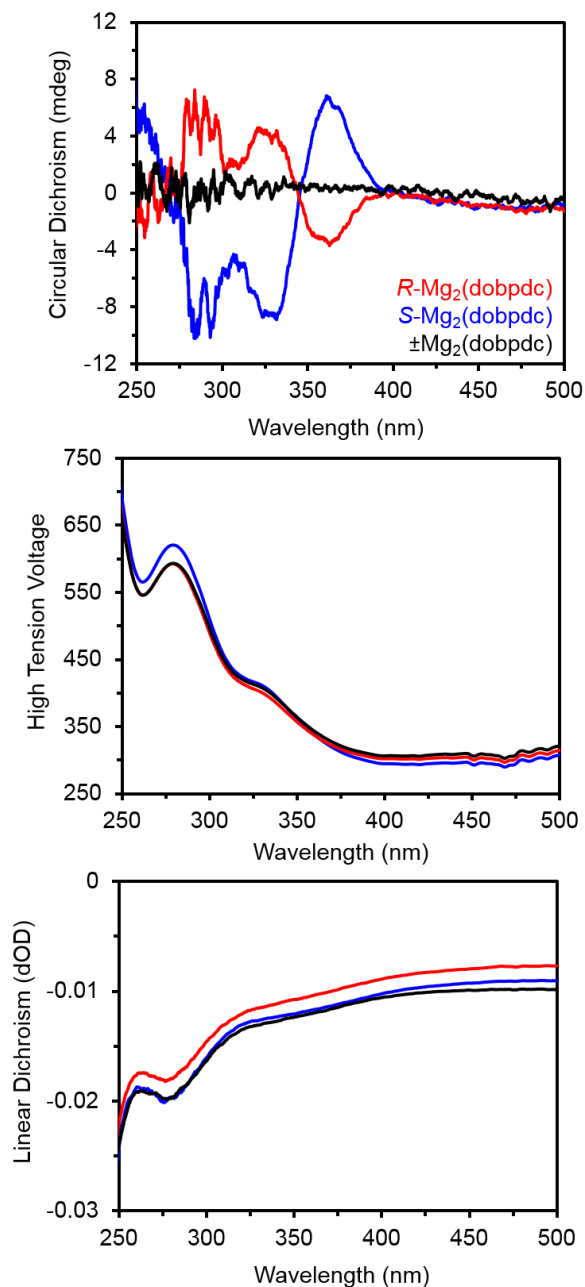


**Figure S51.** Solid-state circular dichroism and associated control spectra measured by transmission for *R*-Mg<sub>2</sub>(dobpdc) (red), *S*-Mg<sub>2</sub>(dobpdc) (blue), and  $\pm$ Mg<sub>2</sub>(dobpdc) (black) in pellets mixed with KBr. (Top) Circular dichroism plot. The noise level is high at wavelengths shorter than 300 nm, a result of the high absorbance exhibited at those wavelengths. Therefore, the data are more trustworthy at wavelengths longer than 300 nm. (Middle) High-tension voltage, which indicates the absorbance of the sample, measured across the same wavelength range. (Bottom) Linear dichroism (LD) measured across the same range of wavelengths. When the LD spectrum was recorded with the sample tablet oriented at four different angles, very little difference was observed, indicating that the CD spectrum at top was reliable (data not shown).

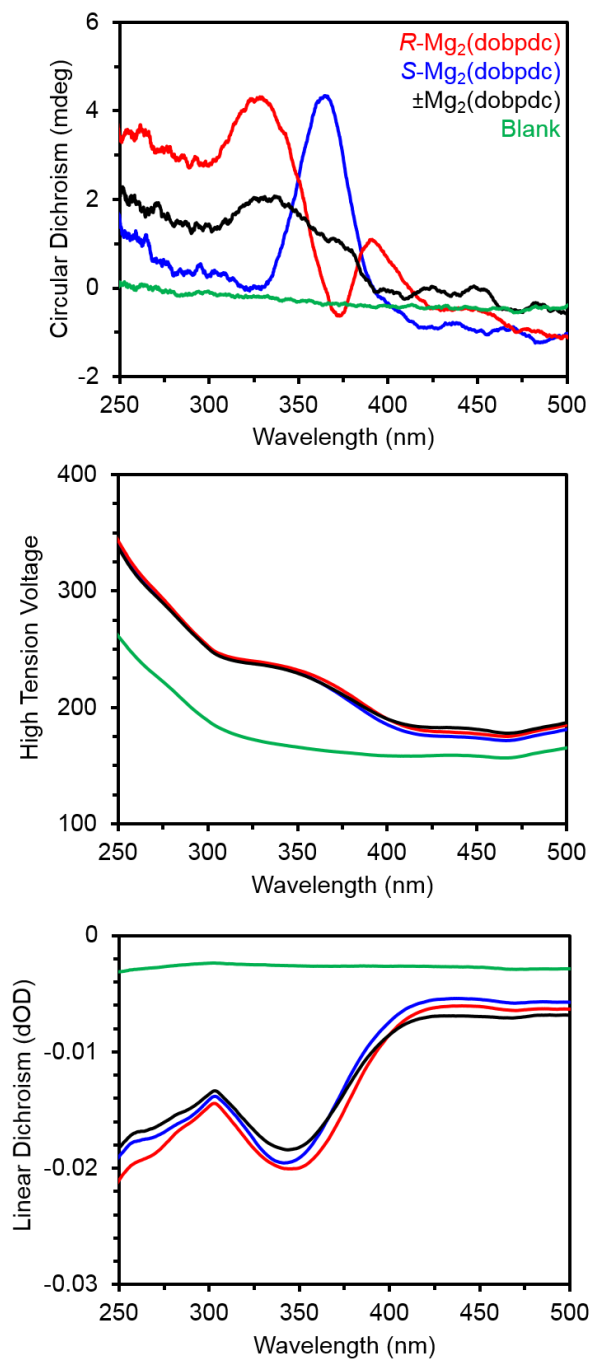


**Figure S52.** Raw spectra for solid-state circular dichroism (CD) measured by diffuse reflectance for *R*-Mg<sub>2</sub>(dobpdc) (red), *S*-Mg<sub>2</sub>(dobpdc) (blue), (±)-Mg<sub>2</sub>(dobpdc) (black), and a blank measurement containing no sample (green). (Top) Raw CD spectra. Baseline drift is apparent in all of the Mg<sub>2</sub>(dobpdc) samples, making subtraction of the Mg<sub>2</sub>(dobpdc) spectrum necessary (see preceding figure). (Middle) High tension voltage of the same samples. (Bottom) Linear dichroism of the same samples.

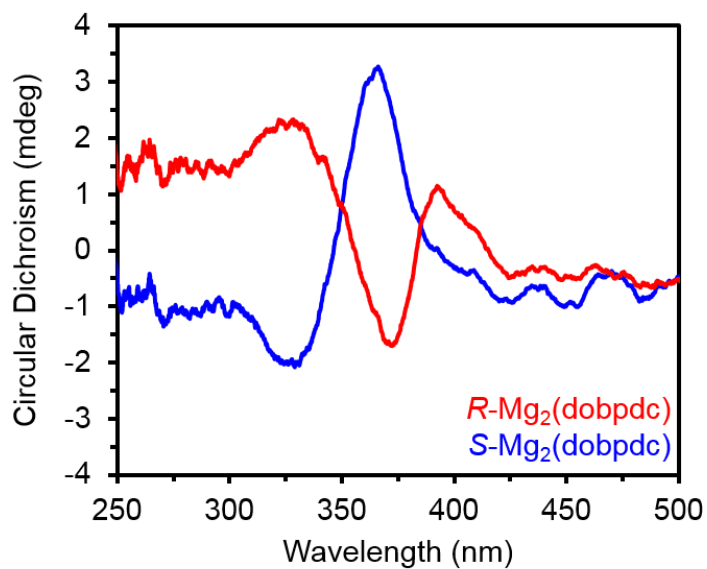


**Figure S53.** Solid-state circular dichroism (CD) measured by diffuse reflectance for *R*-Mg<sub>2</sub>(dobpdc) (red) and *S*-Mg<sub>2</sub>(dobpdc) (blue). To generate these traces, the spectrum of (±)-Mg<sub>2</sub>(dobpdc) was subtracted from the raw spectra of *R*- and *S*-Mg<sub>2</sub>(dobpdc), respectively. This subtraction procedure was implemented because all three samples exhibited baseline shift, possibly caused by interference from light diffusion.

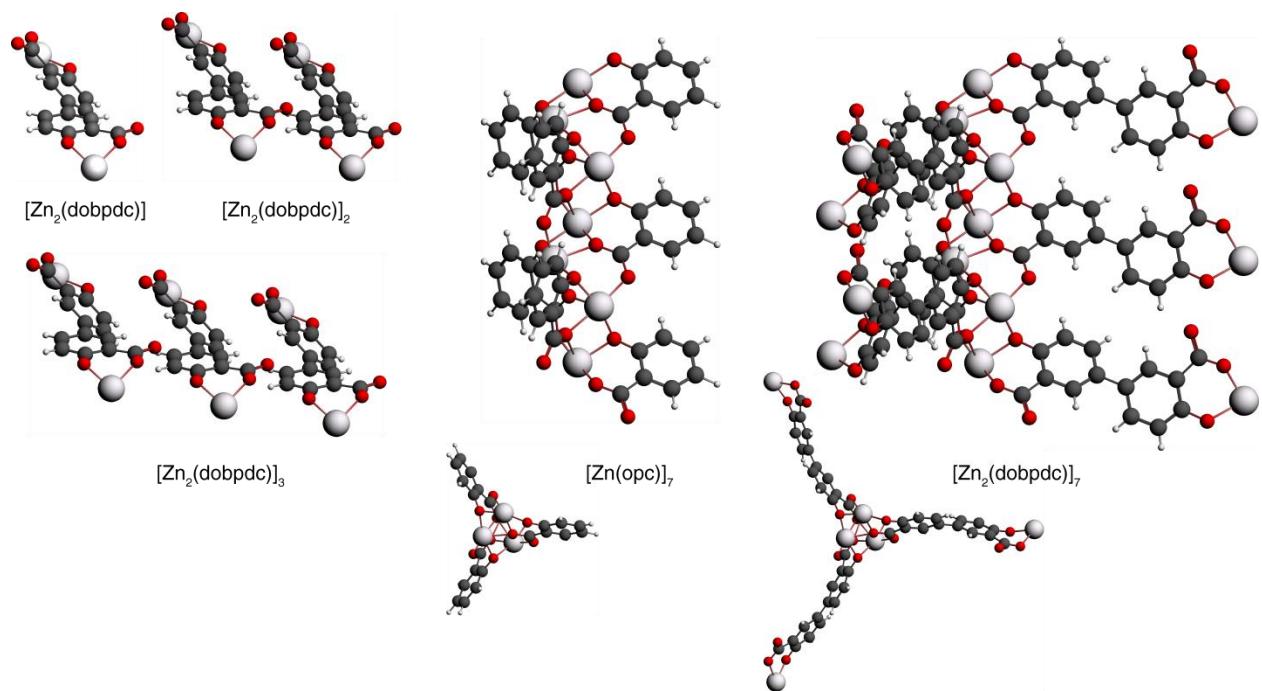


**Figure S54.** Structural motifs extracted from the left-handed (*S*) crystal structure of DMA-solvated  $\text{Zn}_2(\text{dobpdc})$  used for the CD spectra calculations.

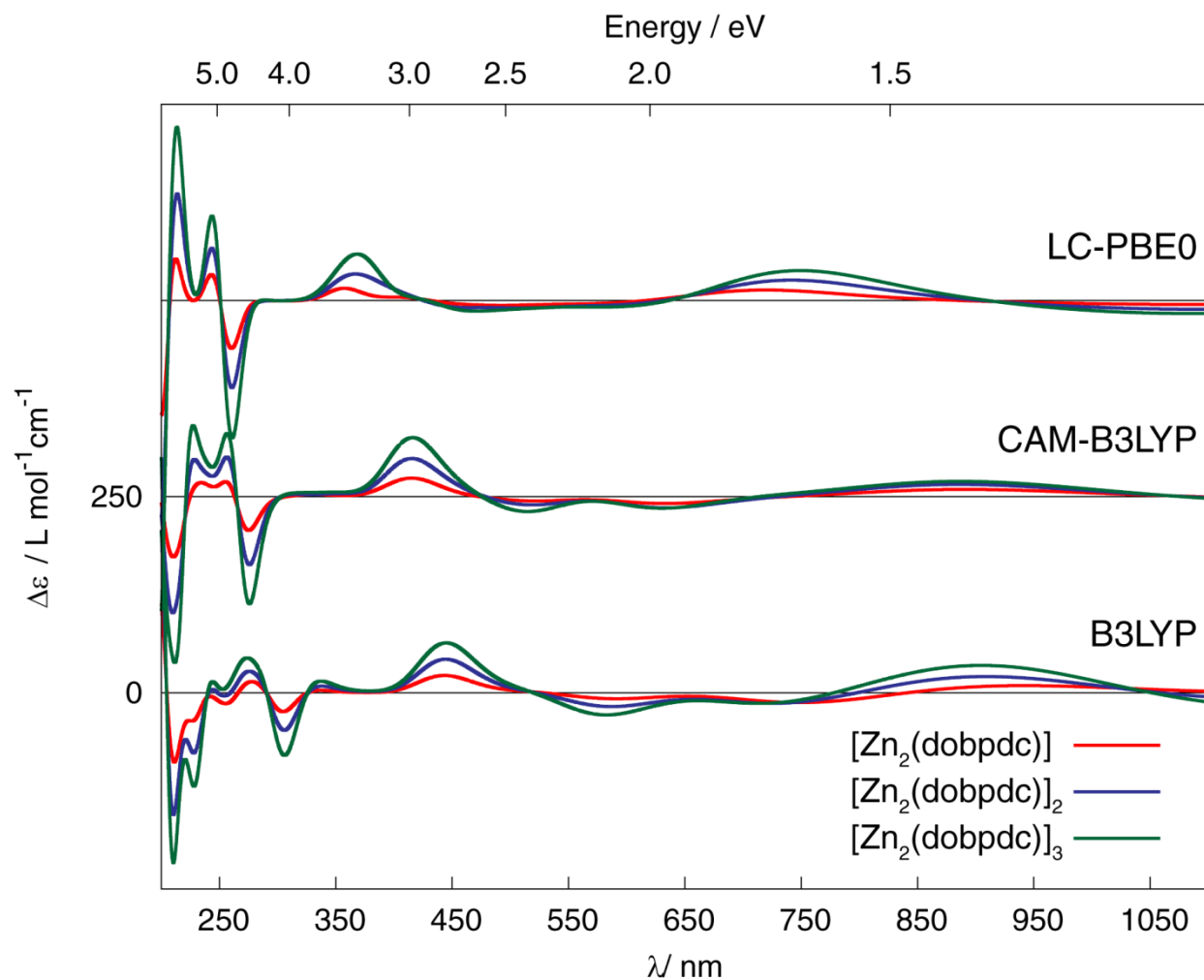


**Figure S55.** Comparison of simulated CD spectra (between 200–1100 nm) for monomer, dimer, and trimer model of the twist  $Zn_2(dobpdc)$  molecules shown in Figure S53. No spectral shift has been applied.

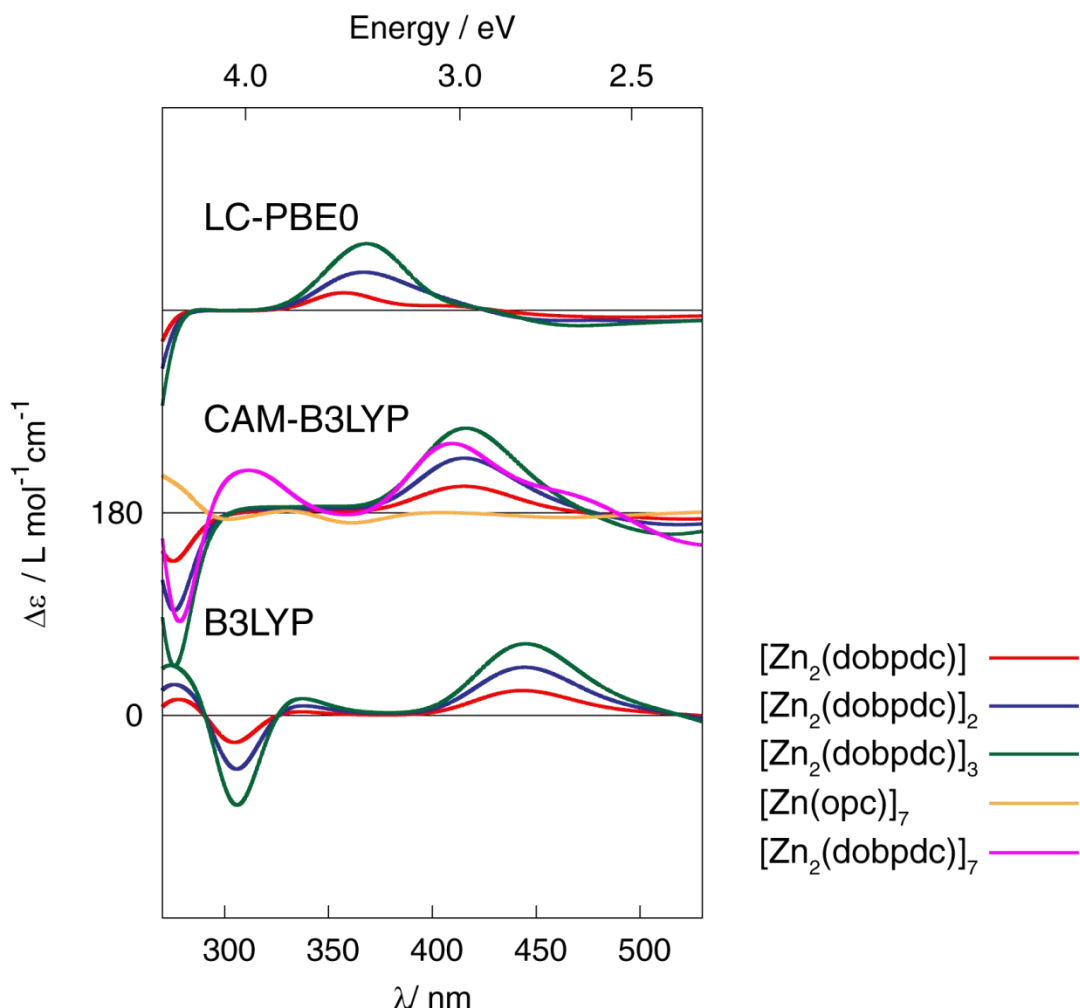


**Figure S56.** Comparison of simulated CD spectra between 270–530 nm for all structural motifs extracted from the left-handed (*S*) crystal structure of DMA-solvated  $\text{Zn}_2(\text{dobpdc})$  including monomer, dimer, and trimer model of the twist  $\text{Zn}_2(\text{dobpdc})$  molecules, model of the  $\text{Zn}_2(\text{dobpdc})$  motif in the channel corners, and the more extended fragment of  $\text{Zn}_2(\text{dobpdc})$  channels (the structures are shown in Figure S54). No spectral shift has been applied.

## 8. Attempts to synthesize large enantiopure $\text{Zn}_2(\text{dobpdc})$ single crystals

**Procedure for synthesizing  $\text{Zn}_2(\text{dobpdc})$  single crystals in the presence of D-panthenol.** Attempts to synthesize large single crystals of  $\text{Zn}_2(\text{dobpdc})$  in the presence of D-panthenol were prepared following our previously-reported procedure for synthesizing racemic twinned single crystals of  $\text{Zn}_2(\text{dobpdc})$ ,<sup>1</sup> with slight modifications.

For synthesis of  $\text{Zn}_2(\text{dobpdc})$  in the presence of 3 or 10 equiv. D-panthenol (relative to  $\text{H}_4\text{dobpdc}$ ),  $\text{H}_4\text{dobpdc}$  (82 mg, 0.30 mmol) was dissolved in 10.0 mL of dimethylacetamide (DMA) in a 20 mL vial. In a second 20 mL vial,  $\text{Zn}(\text{NO}_3)_2 \cdot 6\text{H}_2\text{O}$  (223 mg, 0.750 mmol) was dissolved in a mixture of 10.0 mL ethanol

and 10.0 mL H<sub>2</sub>O. After all reagents had been dissolved, the two stocks were mixed to generate a single 30.0 mL reactant stock solution. Next, a D-panthenol stock solution was prepared by dissolving D-panthenol (262 mg, 1.28 mmol) in DMA (1.06 mL) to generate a 1.2 M D-panthenol stock solution. Several thick-walled borosilicate tubes were each charged with 1.2 mL of reactant stock solution, followed by 32  $\mu$ L or 105  $\mu$ L of D-panthenol stock solution, respectively, for the 3 equiv. and 10 equiv. D-panthenol reactions. The resulting reaction solutions with 3 equiv. D-panthenol (9.74 mM H<sub>4</sub>dobpdc, 2.5 equiv. Zn(NO<sub>3</sub>)<sub>2</sub>·6H<sub>2</sub>O, 3.15 equiv. D-panthenol, 1.232 mL of 350:325:325 DMA:ethanol:water, v:v:v) or 10 equiv. D-panthenol (9.20 mM H<sub>4</sub>dobpdc, 2.5 equiv. Zn(NO<sub>3</sub>)<sub>2</sub>·6H<sub>2</sub>O, 10.5 equiv. D-panthenol, 1.305 mL of 387:306.5:306.5 DMA:ethanol:water, v:v:v) were degassed by four freeze–pump–thaw cycles, after which the tubes were flame sealed and placed in an oven pre-heated to 100 °C. After 20 h, colorless, needle-shaped crystals suitable for single-crystal X-ray diffraction had formed.

For synthesis of Zn<sub>2</sub>(dobpdc) in the presence of 20, 60, or 122 equiv. D-panthenol, individual reaction solutions were prepared. For the 20 equiv. D-panthenol reaction, a 1.2 mL solution containing H<sub>4</sub>dobpdc (3.3 mg, 0.012 mmol, 10 mM), Zn(NO<sub>3</sub>)<sub>2</sub>·6H<sub>2</sub>O (8.9 mg, 2.5 equiv.), and D-panthenol (49 mg, 20 equiv.) was prepared in 313:313:333 DMA:ethanol:water (v:v:v). For the 60 equiv. D-panthenol reaction, a 1.2 mL solution containing H<sub>4</sub>dobpdc (3.3 mg, 0.012 mmol, 10 mM), Zn(NO<sub>3</sub>)<sub>2</sub>·6H<sub>2</sub>O (8.9 mg, 2.5 equiv.), and D-panthenol (148 mg, 60 equiv.) was prepared in 272:272:333 DMA:ethanol:water (v:v:v). For the 122 equiv. D-panthenol reaction, a 1.2 mL solution containing H<sub>4</sub>dobpdc (3.3 mg, 0.012 mmol, 10 mM), Zn(NO<sub>3</sub>)<sub>2</sub>·6H<sub>2</sub>O (8.9 mg, 2.5 equiv.), and D-panthenol (300 mg, 122 equiv.) was prepared in 208:208:333 DMA:ethanol:water (v:v:v). Several thick-walled borosilicate tubes were each charged with 1.2 mL of reaction solution. The reaction solutions were degassed by four freeze–pump–thaw cycles, after which the tubes were flame sealed and placed in an oven pre-heated to 100 °C. After 20 h, colorless, needle-shaped crystals suitable for single-crystal X-ray diffraction had formed in the 20 equiv. D-panthenol reaction tube, and polycrystalline powder had formed in the 30 and 122 equiv. D-panthenol reaction tubes.

**Table S4.** Flack Parameters for Zn<sub>2</sub>(dobpdc) Single Crystals Synthesized in the Presence of D-Panthenol

Conditions	Flack Parameter <sup>a</sup>
3 equiv. D-panthenol	0.50(4), 0.48(4)
10 equiv. D-panthenol	0.42(2), 0.40(2), 0.50(5)
20 equiv. D-panthenol	0.46(5)

<sup>a</sup>All structures were refined in the space group *P*3<sub>1</sub>21.

## 9. Powder X-ray diffraction of dach-appended *R*- and *S*-Mg<sub>2</sub>(dobpdc)

### Procedure for Rietveld refinements of enantiopure dach grafted to enantiopure Mg<sub>2</sub>(dobpdc).

The analysis of the X-ray powder diffraction data, including pattern indexing, profile fitting, and Rietveld refinement were performed in TOPAS 4.1.<sup>10</sup> Pawley fitting<sup>11</sup> using the *P*3<sub>1</sub>21 space group resulted in accurate unit cell parameters (Figures S58 and S59), which are listed in Table 1 in the main text. During

the Pawley refinement, the lattice parameters, profile parameters, and background function (a Chebyshev polynomial of 10th order) were also refined.

Similar to the crystal structures of the Zn analogues (analyzed by single-crystal X-ray diffraction), the crystal structures of activated (*R,R*)-dach-*R*-Mg<sub>2</sub>(dobpdc) and (*S,S*)-dach-*R*-Mg<sub>2</sub>(dobpdc) were characterized by disordered amine molecules bound within the pores of the material. The pronounced disorder prevented resolution of the diamine molecules in the crystal structures of both the Zn and Mg analogues. However, dosing with CO<sub>2</sub> resulted in ordering of the amine molecules after the formation of characteristic ammonium carbamate chains, as evidenced by the crystal structure of the Zn analogue solved by single-crystal X-ray diffraction. In order to investigate whether CO<sub>2</sub>-inserted (*R,R*)-dach-*R*-Mg<sub>2</sub>(dobpdc) and (*S,S*)-dach-*R*-Mg<sub>2</sub>(dobpdc) have crystal structures similar to that of (±)-dach-*R*-Zn<sub>2</sub>(dobpdc) (Figure 4), careful Rietveld refinements were performed.<sup>28</sup>

The fractional coordinates for all atoms were taken from the Zn analogue in the space group *P*3<sub>1</sub>21. Due to pronounced thermal motion of the amines, together with the conformational disorder and the lower resolution compared to the single-crystal measurements, unconstrained refinement was not possible. Instead, the fractional coordinates were kept fixed during the Rietveld refinement, with all of the remaining parameters set free. The final Rietveld refinement plots are given in Figure S61 and Figure S62. The refined unit cell parameters, as well as the resulting figures-of-merit, are given in Table S6. The Rietveld refinements indicated that CO<sub>2</sub>-inserted (*R,R*)-dach-*R*-Mg<sub>2</sub>(dobpdc) and (*S,S*)-dach-*R*-Mg<sub>2</sub>(dobpdc) are isostructural to CO<sub>2</sub>-inserted (±)-dach-*R*-Zn<sub>2</sub>(dobpdc).

**Table S5.** Unit cell parameters of activated (±)-dach-*R*-Mg<sub>2</sub>(dobpdc), (*R,R*)-dach-*R*-Mg<sub>2</sub>(dobpdc), and (*S,S*)-dach-*R*-Mg<sub>2</sub>(dobpdc); determined via Pawley fitting of synchrotron powder X-ray diffraction data.

	(±)-dach- <i>R</i> - Mg <sub>2</sub> (dobpdc)	( <i>R,R</i> )-dach- <i>R</i> - Mg <sub>2</sub> (dobpdc)	( <i>S,S</i> )-dach- <i>R</i> - Mg <sub>2</sub> (dobpdc)
<b>Space group</b>	<i>P</i> 3 <sub>2</sub> 21	<i>P</i> 3 <sub>1</sub> 21	<i>P</i> 3 <sub>1</sub> 21
<b><i>a</i> / Å</b>	21.4306(11)	21.1813(11)	21.3988(11)
<b><i>c</i> / Å</b>	6.9107(5)	6.8612(5)	6.8697(5)
<b><i>V</i> / Å<sup>3</sup></b>	2748.7(4)	2665.9(3)	2724.2(3)
<b><i>R</i><sub>exp</sub></b>	2.203	2.473	2.298
<b><i>R</i><sub>wp</sub></b>	2.577	3.511	3.017
<b><i>R</i><sub>p</sub></b>	1.699	1.958	2.074
<b>Wavelength (Å)</b>	0.45241	0.45241	0.42541
<b>Temperature</b>	298 K	298 K	298 K



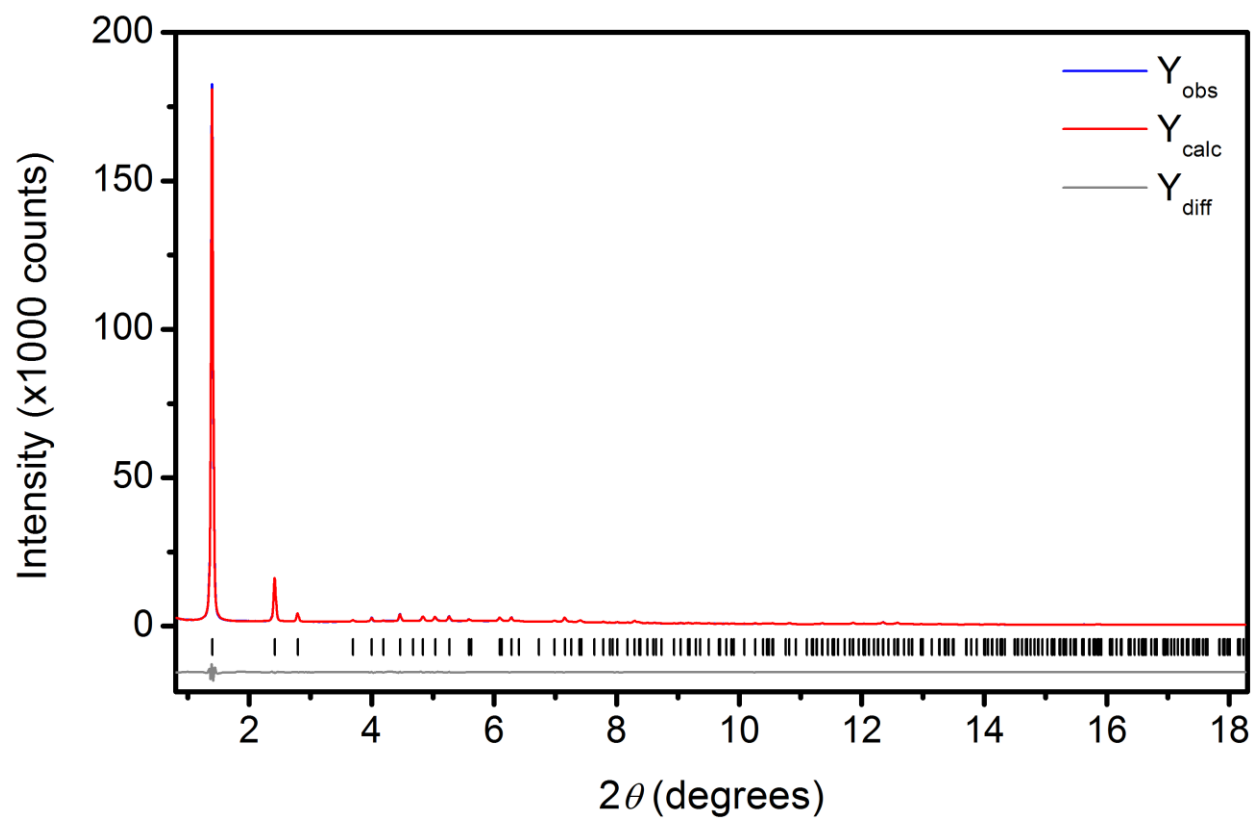


**Figure S57.** Pawley refinement of (+)-dach-*R*-Mg<sub>2</sub>(dobpdc) at 298 K from 0.8° to 18.3°. Blue and red lines represent the observed and calculated diffraction patterns, respectively. The gray line represents the difference between observed and calculated patterns, and the black tick marks indicate calculated Bragg peak positions. The wavelength was 0.45241 Å.

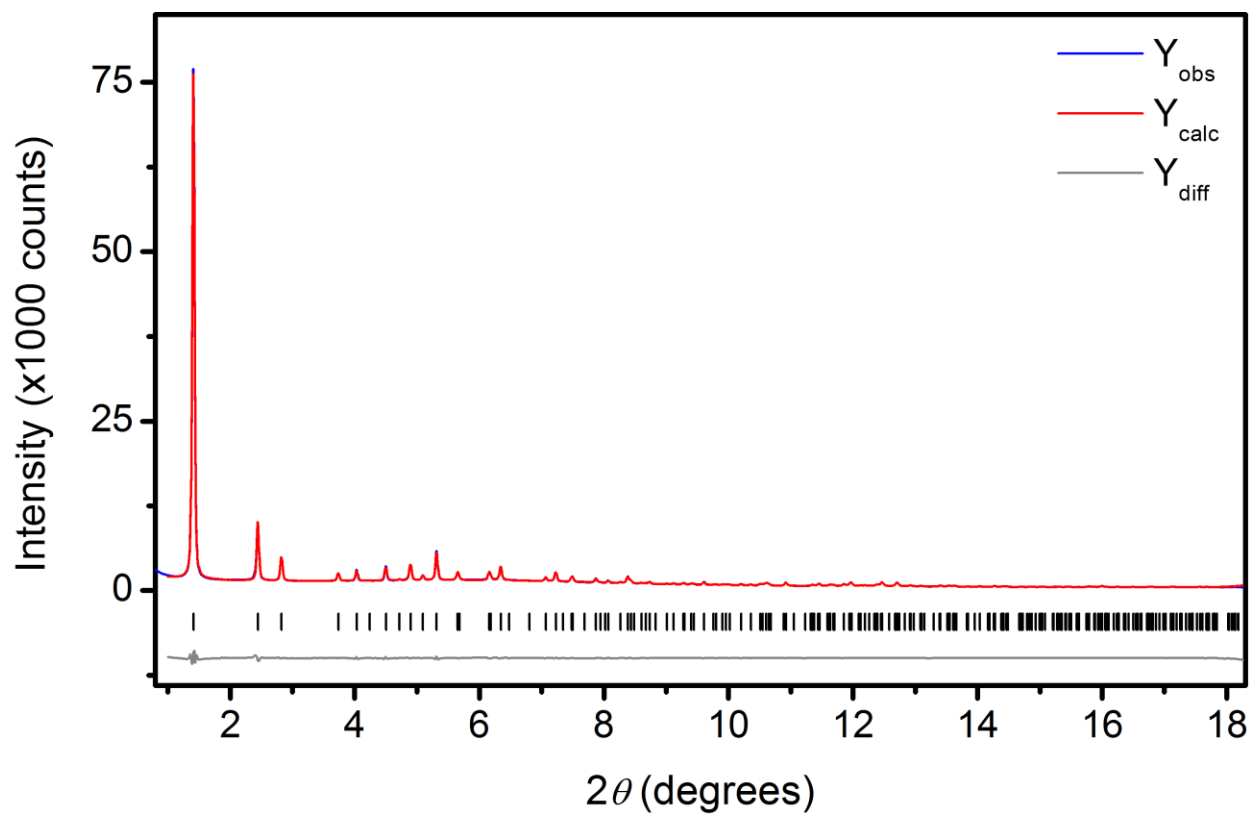


**Figure S58.** Pawley refinement of *(R,R)*-dach-*R*-Mg<sub>2</sub>(dobpdc) at 298 K from 0.8° to 18.3°. Blue and red lines represent the observed and calculated diffraction patterns, respectively. The gray line represents the difference between observed and calculated patterns, and the black tick marks indicate calculated Bragg peak positions. The wavelength was 0.45241 Å.

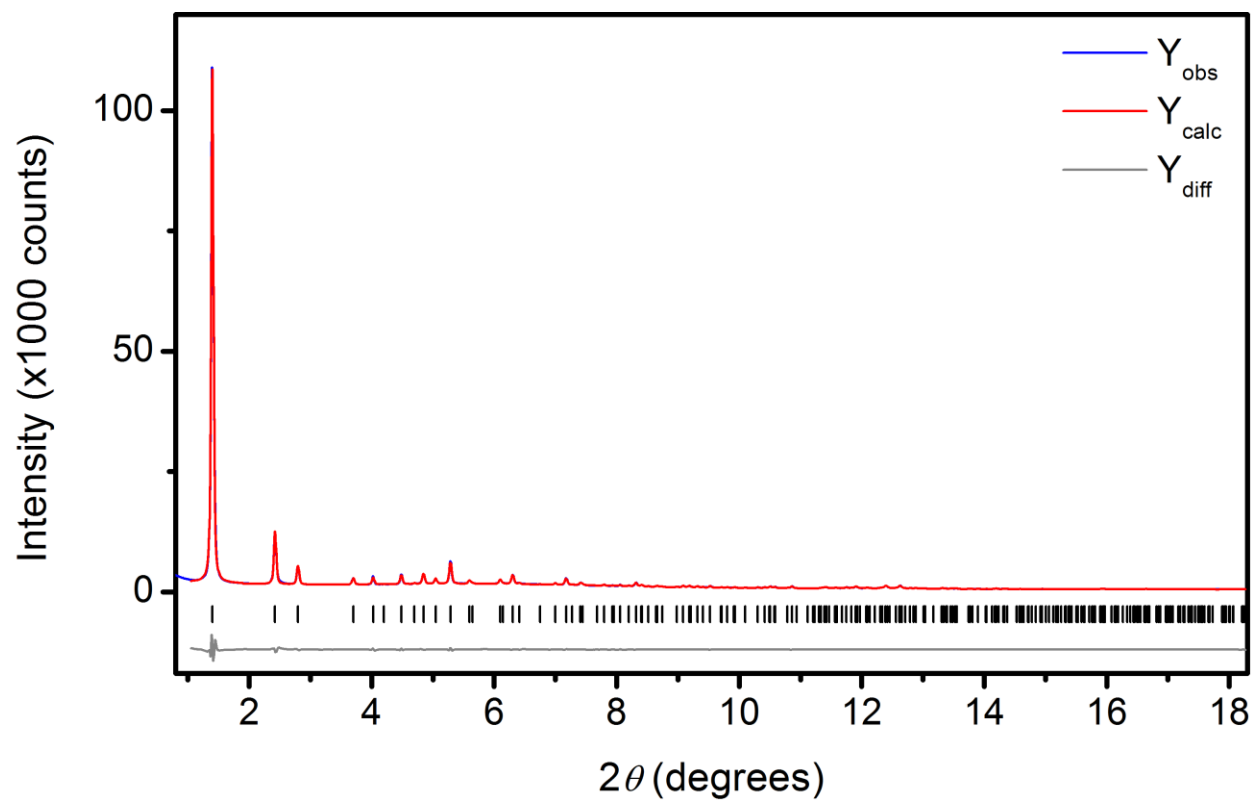


**Figure S59.** Pawley refinement of (*S,S*)-dach-*R*-Mg<sub>2</sub>(dobpdc) at 298 K from 0.8° to 18.3°. Blue and red lines represent the observed and calculated diffraction patterns, respectively. The gray line represents the difference between observed and calculated patterns, and the black tick marks indicate calculated Bragg peak positions. The wavelength was 0.45241 Å.

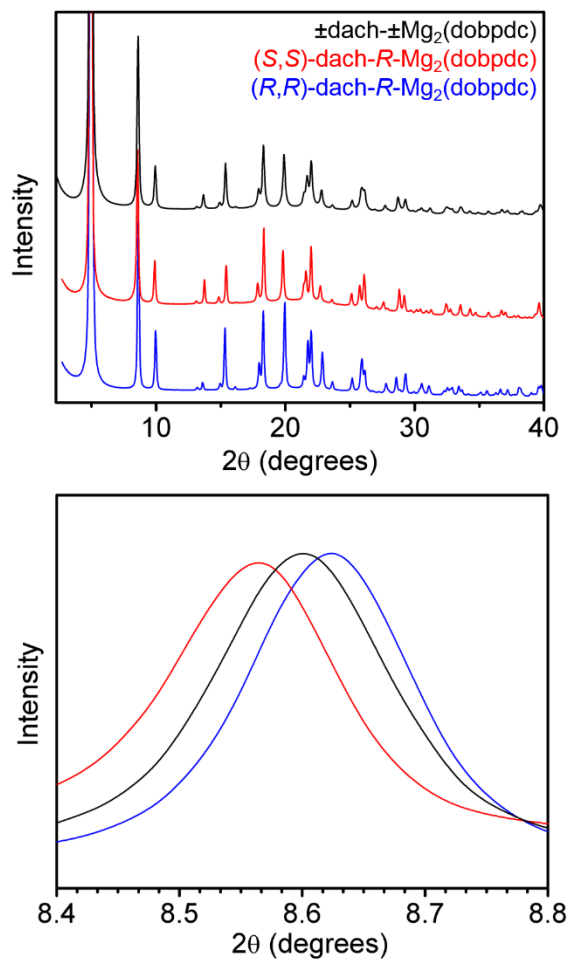


**Figure S60.** Synchrotron powder X-ray diffraction patterns for  $\text{CO}_2$ -inserted  $\text{Mg}_2(\text{dobpdc})$  grafted with  $(\pm)$ -dach (black),  $(S,S)$ -dach (red), or  $(R,R)$ -dach (blue). The top and bottom panels present the same powder patterns, but with different  $x$ -axis scales. The wavelength was  $0.45241 \text{ \AA}$ , but the data in the plot were converted to a wavelength of  $1.5418 \text{ \AA}$ .

**Table S6.** Unit cell parameters of CO<sub>2</sub>-inserted ( $\pm$ )-dach-*R*-Mg<sub>2</sub>(dobpdc), (*R,R*)-dach-*R*-Mg<sub>2</sub>(dobpdc), and (*S,S*)-dach-*R*-Mg<sub>2</sub>(dobpdc); determined via Rietveld refinement of synchrotron powder X-ray diffraction data.

	CO <sub>2</sub> -inserted ( $\pm$ )- dach- <i>R</i> - Mg <sub>2</sub> (dobpdc)	CO <sub>2</sub> -inserted ( <i>R,R</i> )- dach- <i>R</i> - Mg <sub>2</sub> (dobpdc)	CO <sub>2</sub> -inserted ( <i>S,S</i> )-dach- <i>R</i> - Mg <sub>2</sub> (dobpdc)
<b>Space group</b>	<i>P</i> 3 <sub>2</sub> 21	<i>P</i> 3 <sub>1</sub> 21	<i>P</i> 3 <sub>1</sub> 21
<i>a</i> / Å	20.5293(8)	20.4280(5)	20.5809(8)
<i>c</i> / Å	6.9401(4)	6.9667(3)	6.8861(4)
<i>V</i> / Å <sup>3</sup>	2533.1(3)	2517.72(16)	2526.0(2)
<i>R</i> <sub>exp</sub>	2.481	2.044	2.605
<i>R</i> <sub>wp</sub>	4.547	3.886	3.291
<i>R</i> <sub>p</sub>	3.079	2.860	2.455
<i>R</i> <sub>bragg</sub>	1.643	1.618	1.522
<i>GoF</i>	1.833	1.902	1.264
<b>Wavelength (Å)</b>	0.45241	0.45241	0.45241
<b>Temperature</b>	333 K	298 K	298 K

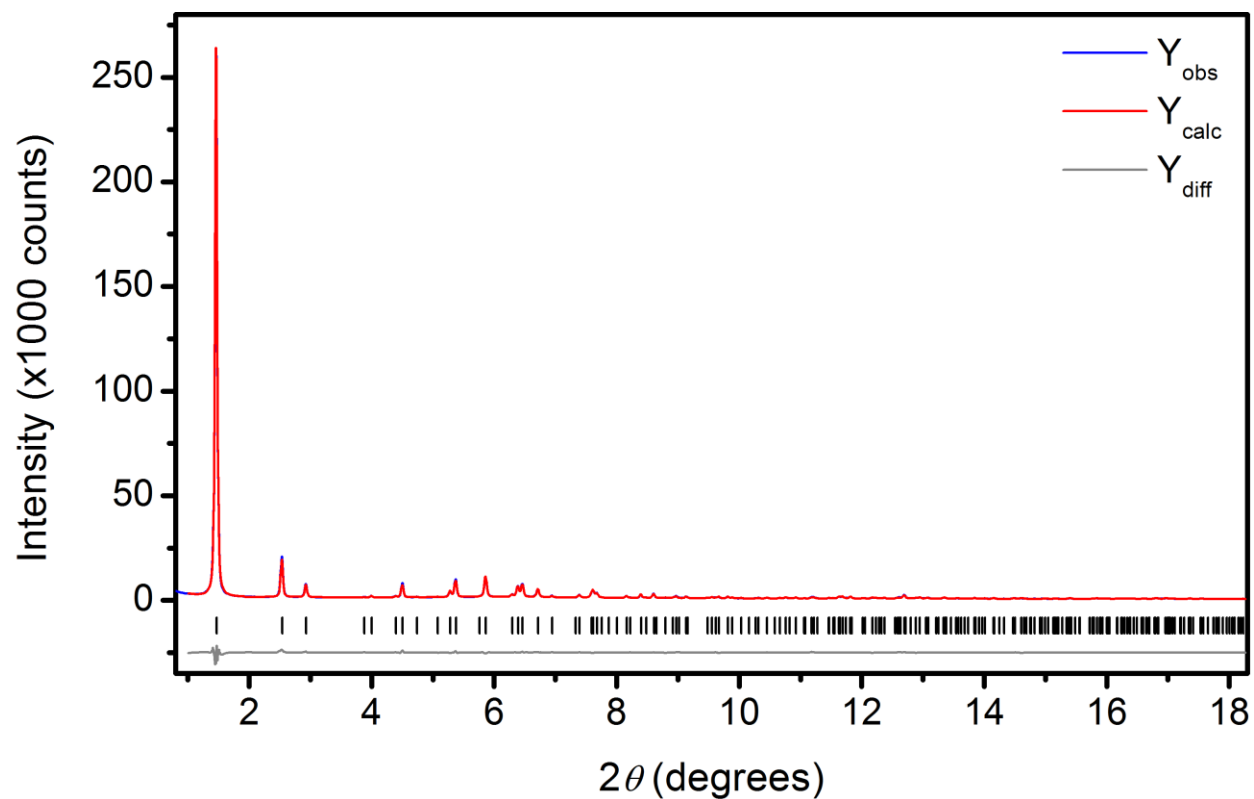


**Figure S61.** Rietveld refinement of CO<sub>2</sub>-inserted (*R,R*)-dach-*R*-Mg<sub>2</sub>(dobpdc) at 298 K from 0.8° to 18.3°. Blue and red lines represent the observed and calculated diffraction patterns, respectively. The gray line represents the difference between observed and calculated patterns, and the black tick marks indicate calculated Bragg peak positions. Figures-of-merit (as defined by TOPAS)  $R_{wp} = 3.89\%$ ,  $R_p = 2.86\%$ ,  $R_{bragg} = 1.62\%$ ,  $GoF = 1.90$ . The wavelength was 0.45241 Å.

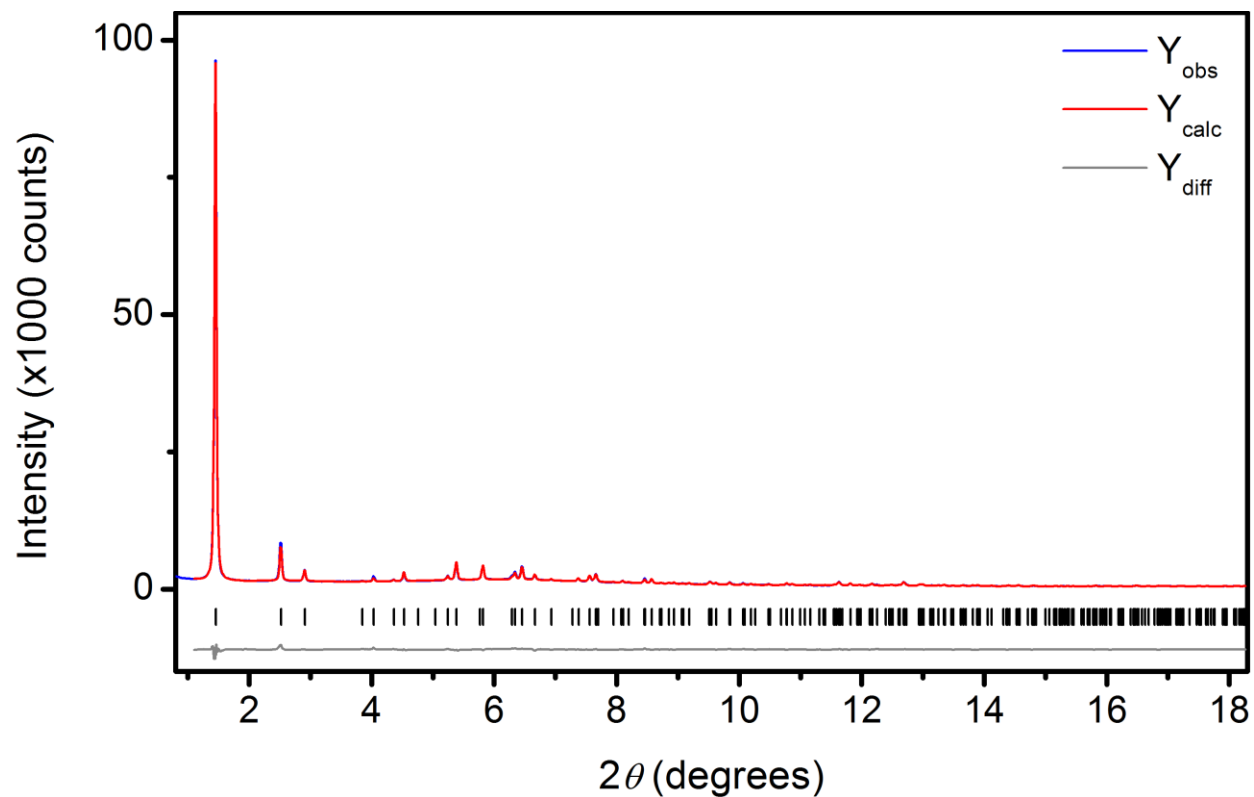


**Figure S62.** Rietveld refinement of CO<sub>2</sub>-inserted (*S,S*)-dach-*R*-Mg<sub>2</sub>(dobpdc) at 298 K from 0.8° to 18.3°. Blue and red lines represent the observed and calculated diffraction patterns, respectively. The gray line represents the difference between observed and calculated patterns, and the black tick marks indicate calculated Bragg peak positions. Figures-of-merit (as defined by TOPAS)  $R_{wp} = 3.29\%$ ,  $R_p = 2.46\%$ ,  $R_{bragg} = 1.52\%$ ,  $GoF = 1.26$ . The wavelength was 0.45241 Å.

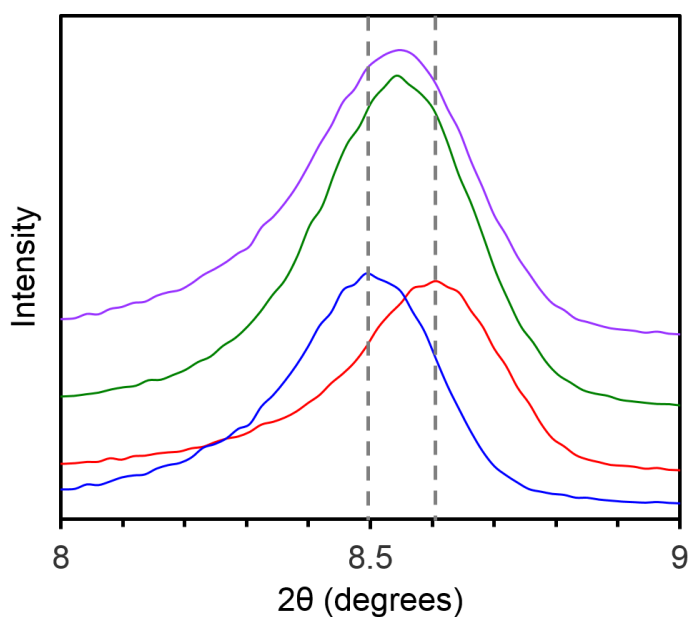
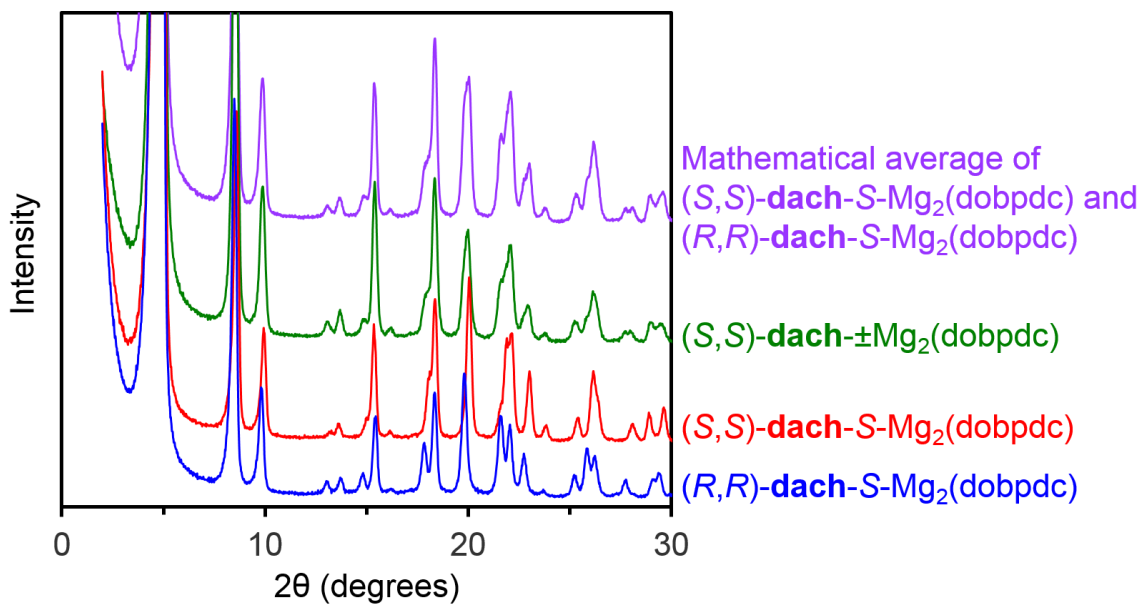


**Figure S63.** Powder X-ray diffraction patterns ( $\lambda = 1.5418 \text{ \AA}$ ) of CO<sub>2</sub>-dosed (*R,R*)-dach-*S*-Mg<sub>2</sub>(dobpdc) (blue), (*S,S*)-dach-*S*-Mg<sub>2</sub>(dobpdc) (red), and (*S,S*)-dach-(±)-Mg<sub>2</sub>(dobpdc) (green). The purple trace is a mathematical average of the blue and red traces. The top and bottom plots present the same data with different scaling of the axes. The vertical dotted gray lines in the bottom plot indicate the peak positions for the blue and red traces.



## 10. Density functional theory calculations

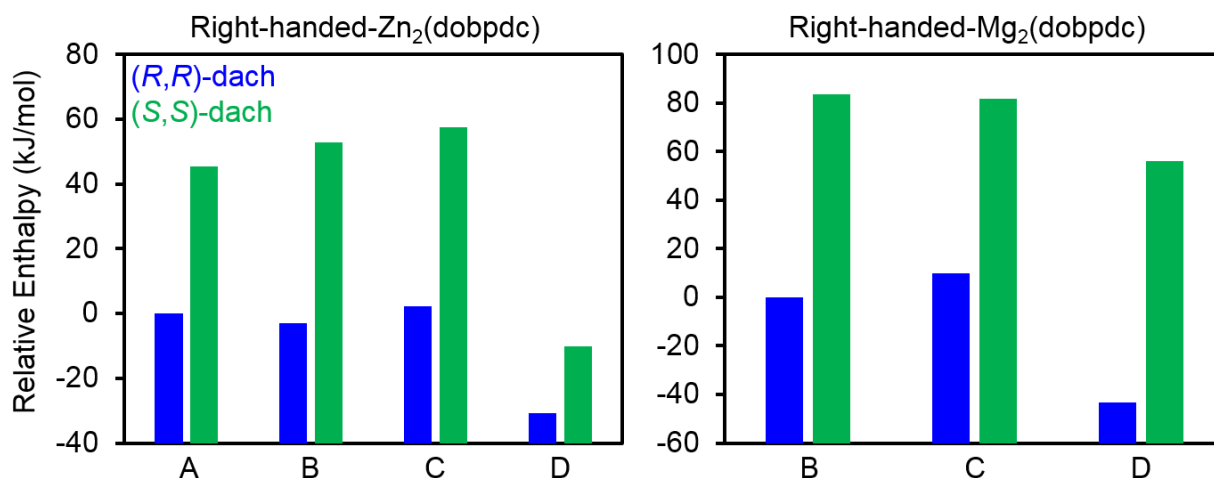


**Figure S64.** DFT-calculated enthalpies for CO<sub>2</sub>-inserted *R*-Zn<sub>2</sub>(dobpdc) (left) or *R*-Mg<sub>2</sub>(dobpdc) (right) grafted with (*R,R*)-dach (blue) or (*S,S*)-dach (green). Lower enthalpy numbers indicate more stable structures. The letters A through D indicate different unit cell constraints imposed during the DFT geometry optimizations: (A) the unit cell parameters were fixed to those of the (±)-dach-Zn<sub>2</sub>(dobpdc) single crystal structure; (B) the unit cell parameters were fixed to those determined by powder X-ray diffraction for (*R,R*)-dach-*R*-Mg<sub>2</sub>(dobpdc) and (*S,S*)-dach-*R*-Mg<sub>2</sub>(dobpdc), with the assumption that *R*-Mg<sub>2</sub>(dobpdc) is the right-handed structure; (C) same as condition (B), except with the incorrect assumption that *S*-Mg<sub>2</sub>(dobpdc) is the right-handed structure; (D) the unit cell parameters were allowed to vary freely during the geometry optimization. (*R,R*)-dach-*R*-Mg<sub>2</sub>(dobpdc) was the more stable structure with all of the different unit cell assumptions.

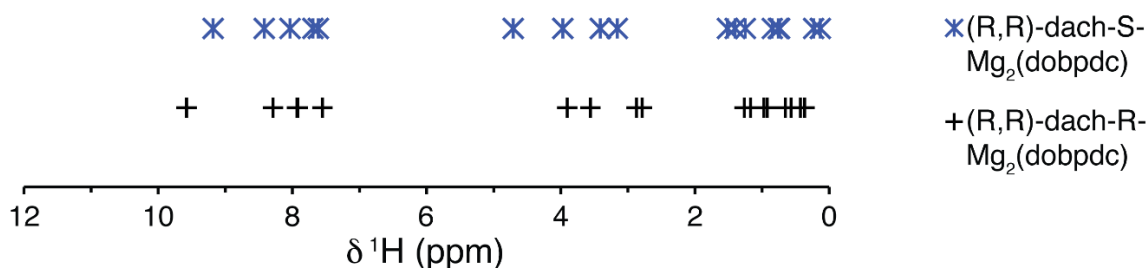


**Figure S65.** DFT calculated <sup>1</sup>H chemical shifts for (*R,R*)-dach-*S*-Mg<sub>2</sub>(dobpdc) and (*R,R*)-dach-*R*-Mg<sub>2</sub>(dobpdc).

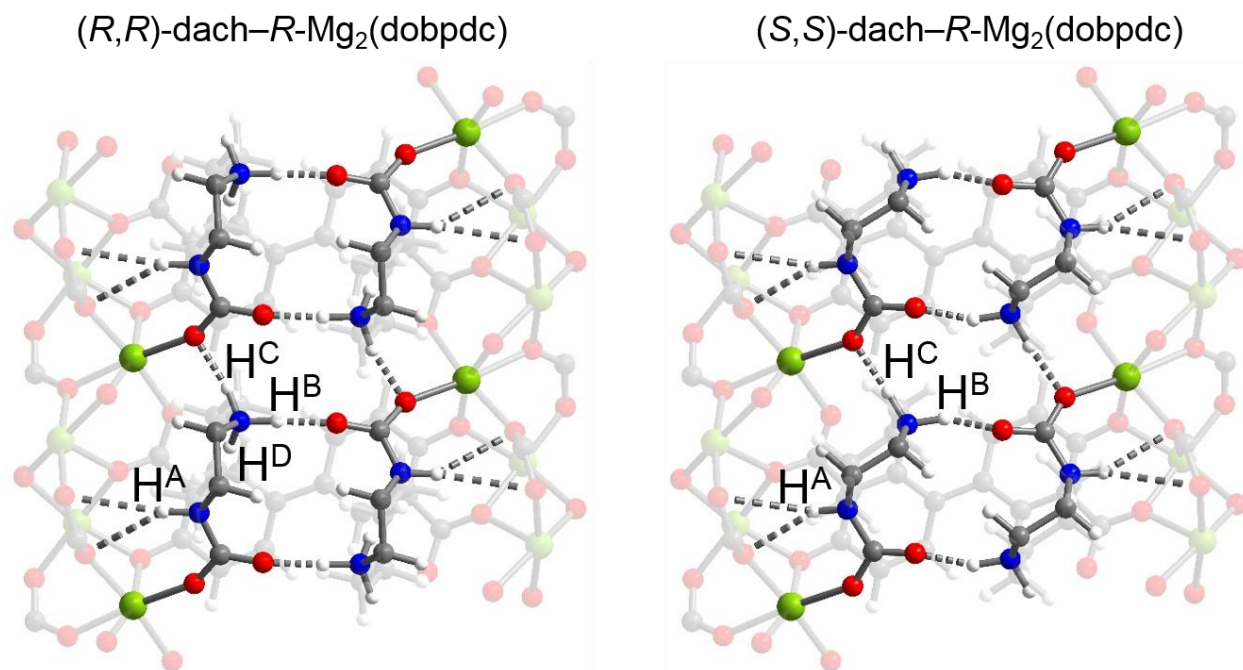


**Figure S66.** DFT calculated structures for CO<sub>2</sub>-inserted  $(R,R)$ -dach- $R$ -Mg<sub>2</sub>(dobpdc) and  $(S,S)$ -dach- $R$ -Mg<sub>2</sub>(dobpdc). These are the same structures shown in Figure 9 in the main text, except with specific ammonium and carbamate hydrogens labeled as H<sup>A</sup>, H<sup>B</sup>, H<sup>C</sup>, and H<sup>D</sup>. These specific hydrogens are referred to in Table S7 below.

**Table S7.** DFT-calculated <sup>1</sup>H NMR chemical shifts for specific hydrogens depicted in Figure S66 for CO<sub>2</sub>-inserted dach-Mg<sub>2</sub>(dobpdc) variants, with unit cell parameters fixed to the experimental values determined by PXRD, with the assumption that  $R$ -Mg<sub>2</sub>(dobpdc) is the right-handed structure.

Chemical Shift	$(R,R)$ -dach- $R$ -Mg <sub>2</sub> (dobpdc)	$(S,S)$ -dach- $R$ -Mg <sub>2</sub> (dobpdc)
H <sup>A</sup> (Carbamate N-H)	3.6 ppm	4.7 ppm
H <sup>B</sup> (Ammonium N-H, H-bonded in $a$ - $b$ plane)	7.9 ppm	7.7 ppm
H <sup>C</sup> (Ammonium N-H, H-bonded along $c$ axis)	9.6 ppm	9.2 ppm
H <sup>D</sup> (Not hydrogen-bonded)	3.9 ppm	4.0 ppm

**Table S8.** Experimental and DFT Calculated Unit Cell Parameters for CO<sub>2</sub>-Inserted Structures of the right-handed framework, *R*-M<sub>2</sub>(dobpdc).

	Experimental Powder X-ray Diffraction			Zn Variable Cell	Mg Variable Cell		
				DFT Calculations		DFT Calculations	
	<i>(R,R)</i> -dach- <i>R</i> -Mg <sub>2</sub> (dobpdc)	(±)-dach-Mg <sub>2</sub> (dobpdc)	<i>(S,S)</i> -dach- <i>R</i> -Mg <sub>2</sub> (dobpdc)	<i>(R,R)</i> -dach-Zn <sub>2</sub> (dobpdc)	<i>(S,S)</i> -dach-Zn <sub>2</sub> (dobpdc)	<i>(R,R)</i> -dach-Mg <sub>2</sub> (dobpdc)	<i>(S,S)</i> -dach-Mg <sub>2</sub> (dobpdc)
<i>a=b</i>	20.4292(9)	20.5293(8)	20.582(1)	20.81	21.31	20.80	20.82
<i>c</i>	6.9663(4)	6.9401(4)	6.8863(4)	7.09	6.80	7.07	6.99

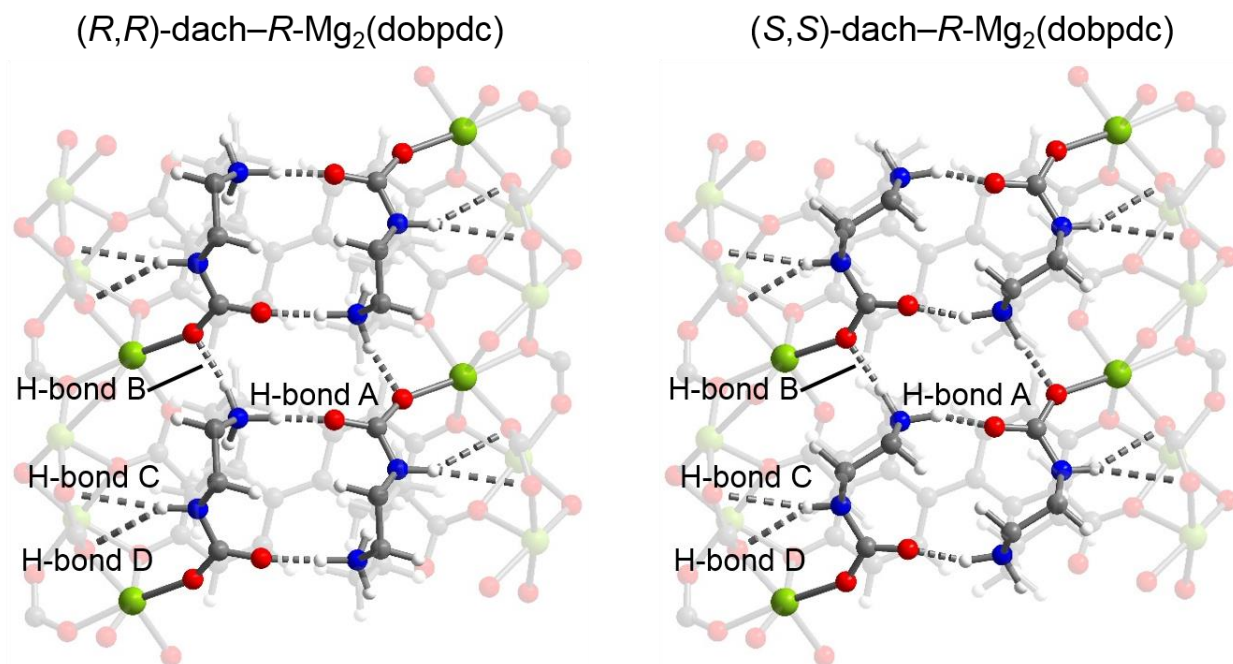


**Figure S67.** DFT calculated structures for CO<sub>2</sub>-inserted *(R,R)*-dach-*R*-Mg<sub>2</sub>(dobpdc) and *(S,S)*-dach-*R*-Mg<sub>2</sub>(dobpdc). These are the same structures shown in Figure 9 in the main text, except with specific hydrogen bonds labeled as A–D. These specific hydrogens are referred to in Tables S9–S12 below.

**Table S9.** DFT hydrogen bond lengths and angles depicted in Figure S67 for CO<sub>2</sub>-inserted dach-Mg<sub>2</sub>(dobpdc) variants, assuming the experimental unit cells from powder X-ray diffraction

Metric	CO <sub>2</sub> -inserted-	CO <sub>2</sub> -inserted-
	( <i>R,R</i> )-dach- <i>R</i> -Mg <sub>2</sub> (dobpdc)	( <i>S,S</i> )-dach- <i>R</i> -Mg <sub>2</sub> (dobpdc)
Hydrogen bond A, N–H···O length	1.700 Å	1.781 Å
Hydrogen bond A, N–H···O angle	175.42°	149.40°
Hydrogen bond A, N–H length	1.051 Å	1.049 Å
Hydrogen bond B, N–H···O length	1.773 Å	1.797 Å
Hydrogen bond B, N–H···O angle	164.44°	175.49°
Hydrogen bond B, N–H length	1.055 Å	1.060 Å
Hydrogen bond C, N–H···O length	2.894 Å	2.476 Å
Hydrogen bond C, N–H···O angle	142.84°	153.72°
Hydrogen bond D, N–H···O length	2.815 Å	2.783 Å
Hydrogen bond D, N–H···O angle	171.15°	144.22°
Carbamate N–H length	1.017 Å	1.016 Å

**Table S10.** DFT hydrogen bond lengths and angles in CO<sub>2</sub>-inserted dach-Zn<sub>2</sub>(dobpdc) variants, assuming the experimental unit cells from powder X-ray diffraction of Mg<sub>2</sub>(dobpdc), with bond labels corresponding to those shown in Figure S67

Metric	CO <sub>2</sub> -inserted-	CO <sub>2</sub> -inserted-
	( <i>R,R</i> )-dach- <i>R</i> -Zn <sub>2</sub> (dobpdc)	( <i>S,S</i> )-dach- <i>R</i> -Zn <sub>2</sub> (dobpdc)
Hydrogen bond A, N–H···O length	1.674Å	1.757Å
Hydrogen bond A, N–H···O angle	173.93°	134.76°
Hydrogen bond A, N–H length	1.052Å	1.051Å
Hydrogen bond B, N–H···O length	1.709Å	1.736Å
Hydrogen bond B, N–H···O angle	166.12°	174.99°
Hydrogen bond B, N–H length	1.060Å	1.062Å
Hydrogen bond C, N–H···O length	2.885Å	2.430Å
Hydrogen bond C, N–H···O angle	144.86°	155.48°
Hydrogen bond D, N–H···O length	2.819Å	2.814Å
Hydrogen bond D, N–H···O angle	168.91°	142.59°
Carbamate N–H length	1.018Å	1.016Å
Carbamate N–C bond length	1.391Å	1.388Å

**Table S11.** DFT hydrogen bond lengths and angles for CO<sub>2</sub>-inserted dach-Zn<sub>2</sub>(dobpdc) variants, assuming the opposite unit cells for the diastereomeric phases compared to experimental powder X-ray diffraction of Mg<sub>2</sub>(dobpdc), with bond labels corresponding to those shown in Figure S67

Metric	CO <sub>2</sub> -inserted-	CO <sub>2</sub> -inserted-
	( <i>R,R</i> )-dach- <i>R</i> -Zn <sub>2</sub> (dobpdc)	( <i>S,S</i> )-dach- <i>R</i> -Zn <sub>2</sub> (dobpdc)
Hydrogen bond A, N–H···O length	1.684Å	1.738Å
Hydrogen bond A, N–H···O angle	172.40°	149.65°
Hydrogen bond A, N–H length	1.050Å	1.051Å
Hydrogen bond B, N–H···O length	1.708Å	1.769Å
Hydrogen bond B, N–H···O angle	164.50°	175.73°
Hydrogen bond B, N–H length	1.060Å	1.059Å
Hydrogen bond C, N–H···O length	2.861Å	2.407Å
Hydrogen bond C, N–H···O angle	143.90°	155.32°
Hydrogen bond D, N–H···O length	2.925Å	2.791Å
Hydrogen bond D, N–H···O angle	170.69°	141.41°
Carbamate N–H length	1.017Å	1.015Å
Carbamate N–C bond length	1.390Å	1.389Å

**Table S12.** DFT hydrogen bond lengths and angles for CO<sub>2</sub>-inserted dach-Zn<sub>2</sub>(dobpdc) variants, with unit cells fixed to those determined by single-crystal X-ray diffraction of (±)-dach-Zn<sub>2</sub>(dobpdc), with bond labels corresponding to those shown in Figure S67

Metric	CO <sub>2</sub> -inserted-	CO <sub>2</sub> -inserted-
	( <i>R,R</i> )-dach- <i>R</i> -Zn <sub>2</sub> (dobpdc)	( <i>S,S</i> )-dach- <i>R</i> -Zn <sub>2</sub> (dobpdc)
Hydrogen bond A, N–H···O length	1.688Å	1.750Å
Hydrogen bond A, N–H···O angle	171.59°	149.31°
Hydrogen bond A, N–H length	1.051Å	1.051Å
Hydrogen bond B, N–H···O length	1.706Å	1.748Å
Hydrogen bond B, N–H···O angle	164.51°	175.84°
Hydrogen bond B, N–H length	1.061Å	1.061Å
Hydrogen bond C, N–H···O length	2.865Å	2.363Å
Hydrogen bond C, N–H···O angle	144.19°	155.99°
Hydrogen bond D, N–H···O length	2.947Å	2.846Å
Hydrogen bond D, N–H···O angle	170.43°	142.94°
Carbamate N–H length	1.018Å	1.016Å
Carbamate N–C bond length	1.390Å	1.388Å

## 11. Solid-state NMR spectroscopy

**Procedure for ssNMR spectroscopy and peak quantification.** NMR spectra were recorded at 16.4 T using a Bruker 3.2 mm magic angle spinning probe and a Bruker Avance spectrometer, with the exception of experiments on <sup>13</sup>CO<sub>2</sub>-inserted (±)-dach-(±)-Mg<sub>2</sub>(dobpdc) that were recorded at 7.1 T using a DOTY 4 mm magic angle spinning probe and a Tecmag Apollo spectrometer. ssNMR experiments were carried out under ambient conditions without temperature control. <sup>13</sup>C NMR spectra were acquired by cross-polarization from <sup>1</sup>H, and with continuous wave <sup>1</sup>H decoupling during the acquisition period. 2-D HETCOR experiments were acquired by cross polarization from <sup>1</sup>H to <sup>13</sup>C. Contact times for cross polarization are

specified in the figure captions.  $^{13}\text{C}$  and  $^1\text{H}$  NMR spectra were referenced using adamantane as a secondary reference at 38.5 ppm ( $^{13}\text{C}$ , tertiary carbon atom) and 1.8 ppm ( $^1\text{H}$ ).

For quantification of  $^{13}\text{C}$  NMR spectra, a series of  $^{13}\text{C}$  spectra were first acquired by cross polarization with a range of different contact times on  $\text{CO}_2$ -inserted (*R,R*)-dach-( $\pm$ )- $\text{Mg}_2(\text{dobpdc})$ . Spectra at different contact times were then fit using DMFIT software,<sup>29</sup> by using two Lorentzian peaks for the carbamate resonance in (*R,R*)-dach-R- $\text{Mg}_2(\text{dobpdc})$ , and a further two Lorentzian peaks for the carbamate resonance in (*R,R*)-dach-S- $\text{Mg}_2(\text{dobpdc})$ . A fifth Lorentzian peak was used to capture weak intensity at  $\sim 160.5$  ppm, the origin of which is currently unknown. The variation of signal intensity ( $I$ ) was then fit as function of contact time ( $t$ ), to quantify the amount ( $I_0$ ) of each diastereomer, as well as the time constant for cross polarization ( $T_{\text{CP}}$ ), using the following equation<sup>30</sup>:  $I(t) = I_0[1 - \exp(-t/T_{\text{CP}})]$ , with one fit performed for each diastereomer. For other samples, a single cross polarization spectrum was obtained with a given contact time. The spectra were then fit as described above, and then the above equation was used to quantify the amount,  $I_0$ , of each diastereomer.

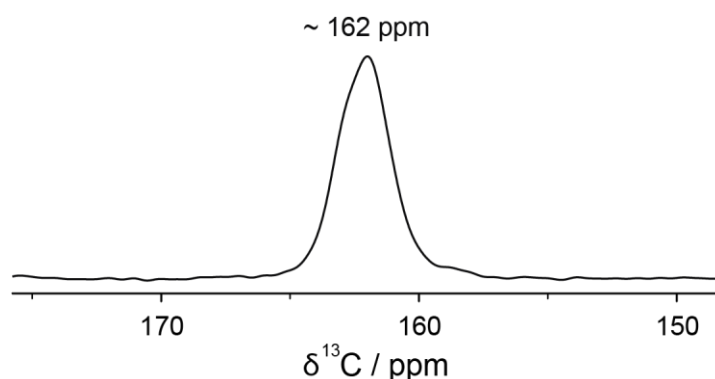


**Figure S68.** Solid-state MAS  $^{13}\text{C}$  NMR (7.1 T) spectrum of  $^{13}\text{CO}_2$ -inserted ( $\pm$ )-dach-( $\pm$ )- $\text{Mg}_2(\text{dobpdc})$ . The magic angle spinning rate was 8 kHz, and the contact time for cross polarization was 1 ms. A broad chemisorbed  $^{13}\text{CO}_2$  signal spanning  $\sim 160$ - $164$  ppm, centered  $\sim 162$  ppm, is observed. By comparison, the corresponding spectra for enantiopure dach- $\text{Mg}_2(\text{dobpdc})$  variants gave narrower peaks.



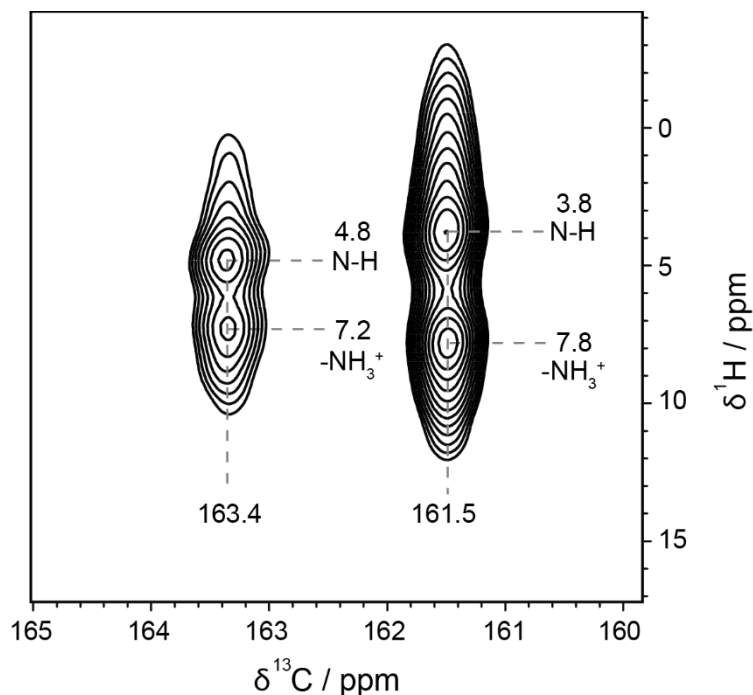


**Figure S69.** Experimental 2-D HETCOR NMR (16.4 T) spectrum for (*R,R*)-dach-(±)-Mg<sub>2</sub>(dobpdc). A longer contact time (relative to Figure 9C in the main text) of 1 ms was used in this experiment, so correlation signal is observed from both the carbamate N–H hydrogens and the ammonium NH<sub>3</sub><sup>+</sup> hydrogens. The magic angle spinning rate was 15 kHz. Distinct chemical shifts are observed for the carbamate N–H hydrogens of (*R,R*)-dach-*S*-Mg<sub>2</sub>(dobpdc) and (*R,R*)-dach-*R*-Mg<sub>2</sub>(dobpdc), in good agreement with DFT calculations (a). The NH<sub>3</sub><sup>+</sup> hydrogens of (*R,R*)-dach-*R*-Mg<sub>2</sub>(dobpdc) are more deshielded, indicating stronger hydrogen bonding, compared to the NH<sub>3</sub><sup>+</sup> hydrogens of (*R,R*)-dach-*S*-Mg<sub>2</sub>(dobpdc). The carbamate N–H hydrogens of (*R,R*)-dach-*S*-Mg<sub>2</sub>(dobpdc) are more deshielded than the carbamate N–H hydrogens of (*R,R*)-dach-*R*-Mg<sub>2</sub>(dobpdc).

## 12. Testing a different chiral diamine-appended $\text{Mg}_2(\text{dobpdc})$ variant

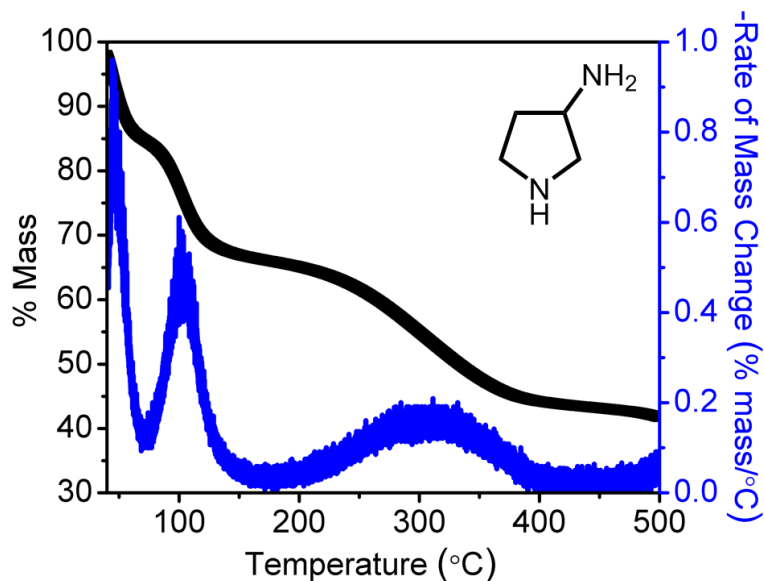


**Figure S70.** Thermogravimetric decomposition trace (black) and negative derivative decomposition trace (“Rate of Mass Change”, blue) for  $(\pm)$ -3-aminopyrrolidine- $(\pm)$ - $\text{Mg}_2(\text{dobpdc})$ . A ramp rate of 1.5 °C/min was used. The initial transition below 70 °C can be attributed to loss of loosely bound toluene solvent molecules. The transition with a peak from 280–330 °C can be attributed to diamine loss.

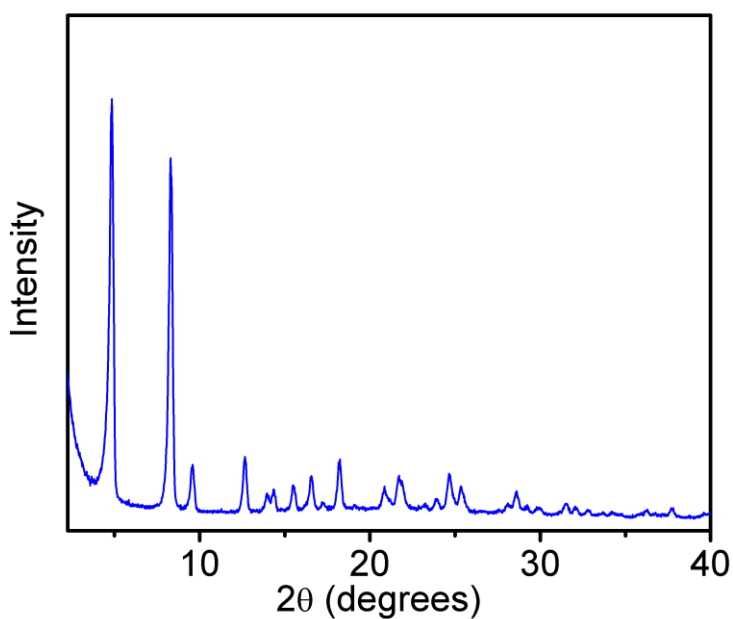


**Figure S71.** Powder X-ray diffraction pattern ( $\lambda = 1.5418 \text{ \AA}$ ) for as-synthesized  $(\pm)$ -3-aminopyrrolidine- $(\pm)$ - $\text{Mg}_2(\text{dobpdc})$ .

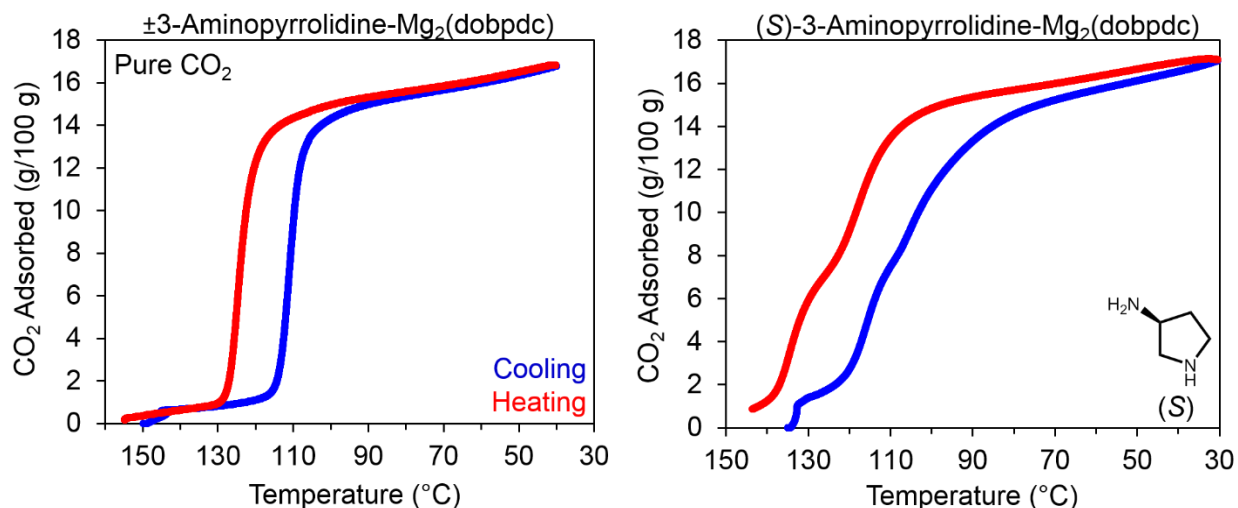


**Figure S72.** Thermogravimetric adsorption (cooling) and heating (red) pure CO<sub>2</sub> isobars for ( $\pm$ )-Mg<sub>2</sub>(dobpdc) grafted with ( $\pm$ )-3-aminopyrrolidine (left) or (S)-3-aminopyrrolidine (right). A temperature ramp rate of 2 °C/min was used. The ( $\pm$ )-3-aminopyrrolidine sample was activated under flowing N<sub>2</sub> at 150 °C for 20 min, although in separate experiments, activating at 170 °C yielded identical results. In the (S)-3-aminopyrrolidine experiment, the sample was activated under flowing N<sub>2</sub> at 150 °C for 20 min.

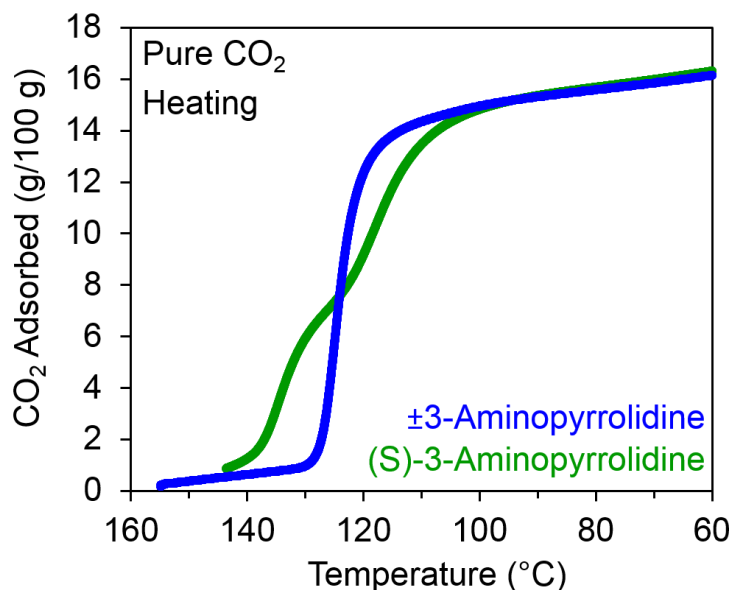


**Figure S73.** Thermogravimetric desorption pure CO<sub>2</sub> isobars for ( $\pm$ )-Mg<sub>2</sub>(dobpdc) grafted with ( $\pm$ )-3-aminopyrrolidine (blue) or (S)-3-aminopyrrolidine (green). A temperature ramp rate of 2 °C/min was used. The samples were first activated under N<sub>2</sub>, then cooled under pure CO<sub>2</sub> to 40 °C, following by heating under pure CO<sub>2</sub>. Only the heating portions of the experiments are shown. At the conclusion of the heating portions of the experiments, the samples were digested and <sup>1</sup>H NMR spectroscopy was performed to quantify diamine loading. The loading for ( $\pm$ )-3-aminopyrrolidine was 99%, and the loading for (S)-3-aminopyrrolidine was 106%.

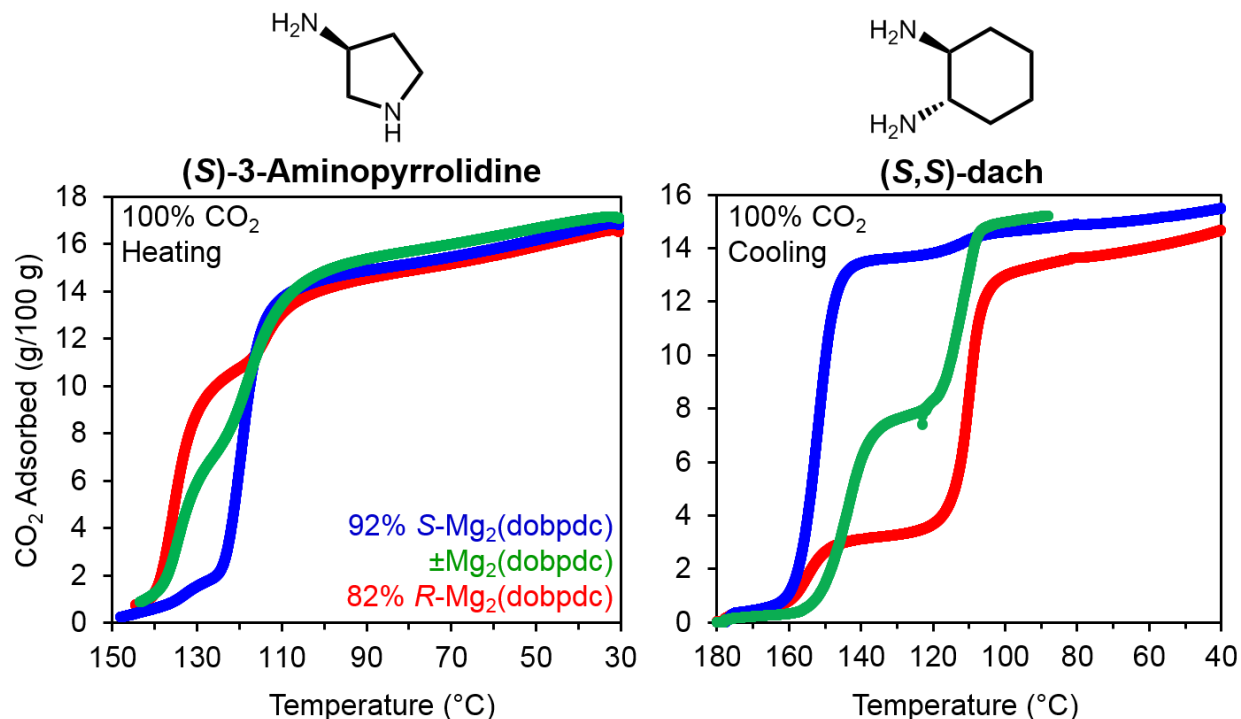


**Figure S74.** Thermogravimetric adsorption heating pure CO<sub>2</sub> isobars for (S)-3-aminopyrrolidine (left) or cooling pure CO<sub>2</sub> isobars for (S,S)-dach (right) grafted to 92% S-Mg<sub>2</sub>(dobpdc) (blue), (±)-Mg<sub>2</sub>(dobpdc) (green), or 82% R-Mg<sub>2</sub>(dobpdc) (red). A temperature ramp rate of 2 °C/min was used.

### 13. References

- (1) Siegelman, R. L.; McDonald, T. M.; Gonzalez, M. I.; Martell, J. D.; Milner, P. J.; Mason, J. A.; Berger, A. H.; Bhowan, A. S.; Long, J. R. *J. Am. Chem. Soc.* **2017**, *139* (30), 10526.
- (2) Milner, P. J.; Siegelman, R. L.; Forse, A. C.; Gonzalez, M. I.; Runčevski, T.; Martell, J. D.; Reimer, J. A.; Long, J. R. *J. Am. Chem. Soc.* **2017**, *139* (38), 13541.
- (3) Milner, P.J.; Martell, J.D.; Siegelman, R.L.; Gygi, D.; Weston, S.C.; Long, J.R. **2017**, *In Review*.
- (4) Deng, H.; Grunder, S.; Cordova, K. E.; Valente, C.; Furukawa, H.; Hmadeh, M.; Gándara, F.; Whalley, A. C.; Liu, Z.; Asahina, S.; Kazumori, H.; O’Keeffe, M.; Terasaki, O.; Stoddart, J. F.; Yaghi, O. M. *Science* **2012**, *336* (6084), 1018.
- (5) *SAINT, APEX2, and APEX3 Software for CCD Diffractometers*; Bruker Analytical X-ray Systems Inc.: Madison, WI, USA, 2014.
- (6) Sheldrick, G. M. *SADABS*; **1996**, University of Göttingen: Göttingen.
- (7) Sheldrick, G. M. *Acta Crystallogr., Sect. A: Found. Adv* **2015**, *71* (1), 3.
- (8) Sheldrick, G. M. *Acta Crystallogr., Sect. C: Struct. Chem.* **2015**, *71* (1), 3.

- (9) Dolomanov, O. V.; Bourhis, L. J.; Gildea, R. J.; Howard, J. A. K.; Puschmann, H. *J. Appl. Crystallogr.* **2009**, *42* (2), 339.
- (10) Bruker AXS, Topas, version 4.1. **2007**.
- (11) Pawley, G. S. *Journal of Applied Crystallography* **1981**, *14* (6), 357.
- (12) Srebro-Hooper, M.; Autschbach, J. *Annual Review of Physical Chemistry* **2017**, *68* (1), 399.
- (13) Becke, A. D. *Physical review A* **1988**, *38* (6), 3098.
- (14) Perdew, J. P. *Physical Review B* **1986**, *33* (12), 8822.
- (15) Perdew, J. P. *Physical Review B* **1986**, *34* (10), 7406.
- (16) Schäfer, A.; Horn, H.; Ahlrichs, R. *The Journal of Chemical Physics* **1992**, *97* (4), 2571.
- (17) Eichkorn, K.; Weigend, F.; Treutler, O.; Ahlrichs, R. *Theoretical Chemistry Accounts: Theory, Computation, and Modeling (Theoretica Chimica Acta)* **1997**, *97* (1), 119.
- (18) Weigend, F.; Ahlrichs, R. *Physical Chemistry Chemical Physics* **2005**, *7* (18), 3297.
- (19) TURBOMOLE V6.6 2014, a development of University of Karlsruhe and Forschungszentrum Karlsruhe GmbH, 1989-2007, TURBOMOLE GmbH, since 2007; available from <http://www.turbomole.com>.
- (20) Ahlrichs, R.; Bär, M.; Häser, M.; Horn, H.; Kölmel, C. *Chemical Physics Letters* **1989**, *162* (3), 165.
- (21) Furche, F.; Ahlrichs, R.; Hättig, C.; Klopper, W.; Sierka, M.; Weigend, F. *Wiley Interdisciplinary Reviews: Computational Molecular Science* **2014**, *4* (2), 91.
- (22) Lee, C.; Yang, W.; Parr, R. G. *Physical review B* **1988**, *37* (2), 785.
- (23) Becke, A. D. *J. Chem. Phys* **1993**, *98*, 5648.
- (24) Stephens, P. J.; Devlin, F. J.; Chabalowski, C.F.; Frisch, M. J. *J. Phys. Chem.* **1994**, *98* (45), 11623.
- (25) Yanai, T.; Tew, D. P.; Handy, N. C. *Chemical Physics Letters* **2004**, *393* (1), 51.
- (26) Frisch, M. J.; Trucks, G. W.; Schlegel, H. B.; Scuseria, G. E.; Robb, M. A.; Cheeseman, J. R.; Scalmani, G.; Barone, V.; Mennucci, B.; Petersson, G. A. *Inc., Wallingford, CT* **2009**.
- (27) Autschbach, J.; Ziegler, T.; van Gisbergen, S. J.; Baerends, E. J. *The Journal of Chemical Physics* **2002**, *116* (16), 6930.
- (28) Rietveld, H. *Journal of Applied Crystallography* **1969**, *2* (2), 65.
- (29) Massiot, D.; Fayon, F.; Capron, M.; King, I.; Le Calvé, S.; Alonso, B.; Durand, J.-O.; Bujoli, B.; Gan, Z.; Hoatson, G. *Magnetic Resonance in Chemistry* **2002**, *40* (1), 70.
- (30) Kolodziejski, W.; Klinowski, J. *Chem. Rev.* **2002**, *102* (3), 613.